UNIVERSITY OF OKLAHOMA

GRADUATE COLLEGE

POROVISCOELASTICITY AND ANALYTICAL SOLUTIONS OF SELECTED PROBLEMS IN ENGINEERING

A DISSERTATION

SUBMITTED TO THE GRADUATE FACULTY

in partial fulfillment of the requirements for the

Degree of

DOCTOR OF PHILOSOPHY

By

SON KY HOANG
Norman, Oklahoma
2011

POROVISCOELASTICITY AND ANALYTICAL SOLUTIONS
OF SELECTED PROBLEMS IN ENGINEERING

A DISSERTATION APPROVED FOR THE
SCHOOL OF CIVIL ENGINEERING AND ENVIRONMENTAL SCIENCE

BY

Dr. Younane N. Abousleiman, Chair

Dr. Amy B. Cerato

Dr. Feng C. Lai

Dr. Gerald A. Miller

Dr. K.K. Muraleetharan

Acknowledgements

First and foremost, I would like to thank my advisor, Dr. Younane N. Abousleiman, for his guidance throughout my graduate study. His visionary approach to scientific and engineering problems and his unrivaled demand for quality research have always fueled my drive for academic excellence.

I would also like to thank my committee, Dr. Amy B. Cerato, Dr. Feng C. Lai, Dr. Gerald A. Miller, and Dr. K.K. Muraleetharan, for their encouragement and advice. I also took their classes at one time or another; and their enthusiasm for teaching and dedication to students were my motivations to pursue higher academic goals.

My deepest appreciation goes to my colleagues and friends, Dr. Vinh Xuan Nguyen and Mr. Minh Ha Tran, for serving as sounding boards for my ideas and for their constructive criticisms of my works. I am also indebted to Dr. Shengli Chen, Mr. Amin Mehrabian, and Mr. John L. Brumley for many stimulating discussions.

My heartfelt thanks go to my IT colleagues: Subramanyam Kapaleswaran Vallur (Subbu), Joseph Prem Ebenezer, Kiran Reddy Nomula, Sameeri Pavan Kumar Marryboyina (Sam), Dung Tuan Phan, Syed Naveed Hussain Shah, and Thinh Thanh Doan, for implementing some of my theoretical works into user-friendly softwares. Their efforts helped put my research results into practical engineering use much sooner than I could ever imagine. My special thanks must also go to Ms. Carla L. Cates, the integrated PoroMechanics Institute's Manager of Administration and Operations, for always going above and beyond her call of duty to make sure our work go as smoothly as possible.

I must acknowledge my old Physics teachers, Professors Ham Nguyen and Don Trung Dam, for nurturing my curiosity for the underlying mechanism of physical phenomena and instilling in me an appreciation for the beauty of physical reasoning balanced with mathematical modeling. Their superior knowledge and utmost humility are still my aspiration today.

Last but not least, I am grateful to my parents, Dr. Ky Van Hoang and Mrs. Thi Thi Nguyen, and my brother, Mr. Lam Ky Hoang, for their unconditional love and support. I am indebted to my wife, Dr. Huong Thi Lan Pham, and my daughter, Uyen Tu Hoang, for the joy and happiness they bring me everyday.

Table of Contents

List of Tables

List of Figures

Abstract

This study provides newly-derived analytical poroviscoelastic solutions for a number of practical and important engineering problems with various levels of material anisotropy: laboratory and field testing of cylinders (isotropy, transverse isotropy, and weak orthotropy), laboratory testing of rectangular strips (isotropy, transverse isotropy, and orthotropy), and wellbore drilling and tunnel excavation (isotropy and transverse isotropy). The solutions for these problems are crucial in many disciplines such as civil engineering, petroleum engineering, and biomechanics. The newly-derived solutions can be considered extensions of some existing analytical solutions to a higher degree of anisotropy. However, the importance of material anisotropy is self-evident in engineering applications since many bio- and geo-materials are intrinsically anisotropic and their mechanical anisotropy can significantly influence the material behavior as illustrated throughout this dissertation. The frequently-used assumption of material isotropy in poroviscoelasticity to simplify modeling and analysis is therefore no longer justified without thorough calibration and validation.

More important, this study finally establishes the correspondence principle between poroviscoelasticity and poroelasticity with general anisotropy based on rigorous mathematical and physical considerations. The correspondence principle has been established not only in time domain but also in Laplace transform domain, for the general phenomenological formulation as well as for the micromechanical relations between material coefficients, and will be of fundamental importance in the study of poroviscoelasticity. In particular, using the correspondence principle, analytical

poroelastic solutions in the Laplace transform domain with any degree of anisotropy can now be readily transferred to poroviscoelasticity and vice versa.

Chapter 1: Introduction

1.1 Introduction to Poroviscoelasticity

Poroviscoelasticity, simply put, is the crossroad of poroelasticity and viscoelasticity. The former is the study of saturated linearly-elastic porous materials whose coupling between the pore fluid diffusion and the porous matrix deformation significantly influences the overall behavior of the composite material. This theory has been successfully applied in a range of disciplines such as biomechanics (bones, cartilage, etc.), geosciences and petroleum engineering (reservoir engineering, drilling, subsidence, etc.), geotechnical engineering (soil behaviors, consolidation, etc.), civil engineering (foundations, earth dams, seepage, etc.), physical chemistry (transport, fluid flow, etc.), and mechanical engineering (dynamics, wave propagation in porous media, etc.). On the other hand, linear viscoelasticity concerns non-aging materials whose stiffness coefficients are time-dependent. Various geo-materials and biomaterials exhibit viscoelastic behaviors, as will be shown in the next two sections. Following this introduction are brief literature surveys where relevant poroviscoelastic research in geomechanics and biomechanics is summarized. Next, existing analytical poroviscoelastic solutions and the objectives for the development of new ones are reviewed. Finally, some background information pertinent to the presentation of this dissertation is discussed.

1.2 Poroviscoelasticity in Geomechanics and Biomechanics

1.2.1 Poroviscoelasticity in Geomechanics

The study of time-dependent effects, usually spoken of under the general title of 'creep', is of the greatest importance in rock mechanics and geophysics.

Jaeger and Cook, 1979

Although the preceding quotation is a little outdated, as time-dependent effects encompass not only creep-type, i.e., viscoelastic behaviors, but also consolidation-type, i.e., poroelastic behaviors, it highlights the importance of poroviscoelasticity, which envelops both of the aforementioned time-dependent phenomena, in the study of geomechanics. Indeed, poroviscoelastic phenomena have been observed in the laboratory and in the field for a wide range of geo-materials as illustrated in **Table 1.1**. Moreover, mechanical anisotropy has long been observed on various classes of rocks and soils, probably most notably transverse isotropy on sediments and sedimentary rocks. Therefore, analytical anisotropic poroviscoelastic solutions of realistic engineering problems would be very useful in simulating laboratory experiments/field problems and validating numerical schemes in geomechanics.

Table 1.1 – Geo-materials investigated under viscoelasticity, poroelasticity, and poroviscoelasticity.

Geo-material	Modeling		
	Viscoelasticity	**Poroelasticity**	**Poroviscoelasticity**
Alabaster	Griggs, 1939		
Asphalt concrete	Kim et al., 2004		
	Shu and Huang, 2008		
Cement paste		Jones and Grasley, 2009	Grasley, 2007
Chalk	El Rabaa, 1989		
Clay/soil	Geuze and Tjong-Kie, 1954	Gibson et al., 1963	Lefeuve-Mesgouez and Mesgouez, 2008
		Hsu and Lu, 2006	Mesgouez and Lefeuve-Mesgouez, 2009b
Coal	Nomura et al., 1999		
	Díaz et al., 2007		
Glass	Griggs, 1939	Jones and Grasley, 2009	
Ice	Morland, 1991		
Limestone	Griggs, 1939		
Marble	Heard, 1963		
Peat		Zwanenburg and Barends, 2007	
Salt rock	Le Comte, 1965		
	Paraschiv-Munteanu and Cristescu, 2001		
	Carcione et al., 2006		
Sandstone/ siltstone	Teufel, 1983	Mikami et al., 2002	Mesgouez and Lefeuve-Mesgouez, 2009a
	Teufel, 1985	Jourine et al., 2004	Mesgouez and Lefeuve-Mesgouez, 2009b
	El Rabaa and Meadows, 1986	Comerlati et al., 2005	
	Blanton and Teufel, 1986		
	Owen et al., 1988		
	Warpinski and Teufel, 1989		
Shale/ mudstone	Blanton, 1983	Lecampion et al., 2006	Hoang and Abousleiman, 2010
	Teufel, 1983		
	Owen et al., 1988		
	Warpinski and Teufel, 1989		
	Carcione and Cavallini, 1995		
	Bloch et al., 1997		

1.2.2 Poroviscoelasticity in Biomechanics

Biological tissues are all viscoelastic
Fung, 1981

The fact that all biological tissues exhibit viscoelastic behavior when subjected to loading (Fung, 1981) and that they are filled with water (**Table 1.2**) makes poroviscoelasticity indispensable in biomechanics. In fact, poroviscoelasticity has been applied effectively to study natural tissues such as articular cartilage (Mak, 1986) and brain (Cheng and Bilston, 2007) as well as artificial biological materials such as fibrin gels (Noailly et al., 2008).

Table 1.2 – Water content of tissues of different species (after Khalil and Abdel-Messeih, 1954).

Tissue	Human	Monkey	Ox, sheep, pig	Rabbit	Dog
Skeletal muscles	75-78	79	78-79	80	68
Liver	70-75	79	77-78	74	73
Kidney	78-83	-	-	78	-
Skin	72	70	-	75	55
Bone	50	61	-	-	58
Fat	6-20	-	-	-	-

Furthermore, anisotropic viscoelastic properties have also been widely observed on many biological tissues such as cartilage (Jin and Lewis, 2004), meniscus (Anderson et al., 1991), cortical bone (Iyo et al., 2004), and trabecular bone (Deligianni et al., 1994). Moreover, there are biomaterials such as arteries, bones, chondrocytes, and meniscus that have been investigated under both viscoelasticity and poroelasticity but not yet under poroviscoelasticity as shown in **Table 1.3**. Therefore, an anisotropic poroviscoelastic model to simulate relaxation, creep, or hysteresis would be very useful in simulating experimental results and validating numerical schemes for biomaterials.

Table 1.3 – Tissues investigated under viscoelasticity, poroelasticity, and poroviscoelasticity.

Tissue	Modeling		
	Viscoelasticity	**Poroelasticity**	**Poroviscoelasticity**
Arteries	Patel et al., 1973	Kenyon, 1979	
		Simon and Gaballa, 1988	
Articular cartilage	Parsons and Black, 1977	Mow et al., 1980	Mak, 1986
	Hayes and Bodine, 1978	Armstrong et al., 1984	Suh and DiSilvestro, 1999
	Woo et al., 1980	Eisenberg and Grodzinsky, 1987	Huang et al., 2001
	Jin and Lewis, 2004	Cohen et al., 1998	Ehlers and Markert, 2001
		Soulhat et al., 1999	DiSilvestro and Suh, 2001
		Bursać et al., 1999	Wilson et al., 2004
		Li et al., 2000	Wilson et al., 2005
			García and Cortés, 2006
			García and Cortés, 2007
			Hoang and Abousleiman, 2009
			Hoang and Abousleiman, 2010
Bone, cortical	Iyo et al., 2004	Cowin, 1999	
Bone, trabecular	Deligianni et al., 1994	Cowin, 1999	
	Baroud et al., 2003		
Brain		Peña et al., 1999	Cheng and Bilston, 2007
Chondrocytes	Leipzig et al., 2005	Leipzig et al., 2005	
Corneal stroma		Friedman, 1971	
		Eisenberg and Grodzinsky, 1987	
Fat pad, heel	Miller-Young et al., 2002		
Fibrin gels		Noailly et al., 2008	Noailly et al., 2008
Intervertebral disk		Simon et al., 1985	
Meniscus	Anderson et al., 1991	Spilker et al., 1992	
Skin		Oomens et al., 1987	

1.3 Review of Existing Poroviscoelastic Analytical Solutions

The origin of poromechanics can be traced back to 1941 with Biot's ground breaking article "General theory of three-dimensional consolidation". This pioneering

work is now commonly referred to as Biot's theory of poroelasticity. In that paper, Biot offered a consistent phenomenological analysis of saturated porous media, taking into account the full coupling between pore fluid diffusion and solid deformation of a linear elastic matrix. The inclusion of matrix viscoelasticity within the poromechanics framework was also laid out by Biot (1956). In both of those classical papers, Biot offered the analytical solution for the one-dimensional consolidation problem as an example of application. Since then, a number of engineering problems have been investigated under the realm of poroelasticity and poroviscoelasticity, including one-dimensional consolidation problem (**Table 1.4**), Mandel's problem or rectangular geometry (**Table 1.5**), cylinders (**Table 1.6**), and wellbore drilling problem (**Table 1.7**), with various degrees of matrix anisotropy.

Table 1.4 – Studies on the one dimensional consolidation problem.

Anisotropy	**Poroelasticity**	**Poroviscoelasticity**
Isotropy	Biot, 1941	Biot, 1956 Mak, 1986 Schanz and Cheng, 2001
Transverse isotropy		This study

Table 1.5 – Studies on the Mandel's problem (rectangular strip).

Anisotropy	**Poroelasticity**	**Poroviscoelasticity**
Isotropy	Mandel, 1953 Kameo et al., 2008	
Transverse isotropy	Abousleiman et al., 1996a	
Orthotropy		This study

Table 1.6 – Studies on the cylindrical geometry.

Anisotropy	Poroelasticity	Poroviscoelasticity
Isotropy	Armstrong et al., 1984 Cui and Abousleiman, 2001 Sawaguchi and Kurashige, 2005	Abousleiman et al., 1996b Abousleiman and Cheng, 1996 Huang et al., 2001
Transverse isotropy	Abousleiman and Cui, 1998 Zwanenburg and Barends, 2007 Cowin and Mehrabadi, 2007	This study
Weak orthotropy		This study

Table 1.7 – Studies on wellbores.

Anisotropy	Poroelasticity	Poroviscoelasticity
Isotropy	Carter and Booker, 1982 Carter and Booker, 1984 Detournay and Cheng, 1988 Rajapakse, 1993 Cui et al., 1997 Cui et al., 1998 Li, 1999 Li and Flores-Berrones, 2002 Ekbote et al., 2004	Carter and Booker, 1983 Abousleiman et al., 1996b
Transverse isotropy	Abousleiman and Cui, 1998	This study

1.4 Research Objectives and Approach

This study first and foremost aims to establish a correspondence principle between poroviscoelasticity and poroelasticity with general anisotropy through rigorous mathematical and physical considerations. The newly-derived proof of the correspondence principle is given in Chapter 2. Using this correspondence principle, analytical solutions in Laplace transform domain for poroviscoelasticity and poroelasticity can be transferred readily from one model to the other. Armed with such a correspondence principle, the rest of the dissertation aims to derive the analytical poroviscoelastic solutions for the practical engineering problems described below:

Transversely isotropic cylinders under various loading and unloading conditions, with the axis of material symmetry coinciding with the axis of geometrical symmetry, will be analyzed in Chapter 3. This is one of the most useful and versatile class of solutions in both geomechanics and biomechanics. When the lateral surface of the cylinder is confined by a rigid ring (for example uniaxial strain, oedometer, or K_0 test in geomechanics and confined compression test in biomechanics), physically and mathematically the problem becomes a one-dimensional consolidation problem in the axial direction. On the other hand, when the sample is not constrained to uniaxial strain deformation, the setup can be used to simulate a wide range of laboratory testing conditions (unconfined compression test, unjacketed triaxial test, and jacketed triaxial test). Furthermore, the time-dependent deformation of drill cores due to the unloading from in-situ state of stress can also be simulated using this class of solutions. Information about the in-situ stress state, which is crucial in various petroleum engineering and civil engineering applications, can be extracted from the analysis of drill core relaxation, as will be shown in details in Chapter 3.

Cylinders with weak cylindrical-orthotropy under laboratory loading conditions, also with the axis of material symmetry coinciding with the axis of geometrical symmetry, are investigated next. This is an extension of the study on transversely isotropic cylinders under laboratory conditions and can be of particular importance for cylindrically-reinforced low permeability clays with significant viscoelastic behavior or cylindrically orthotropic poroviscoelastic biological tissues. Details of the modeling are presented in Chapter 4.

For geo-materials and biological tissues with Cartesian mechanical orthotropy, the symmetry of material properties implies that rectangular strips are the best sample geometry to use for mechanical characterization. This setup is the famous Mandel's problem in poromechanics. Orthotropic rectangular strips under unconfined compression loading will be studied in Chapter 5.

Finally, the important problem of wellbore drilling through transversely isotropic rocks is considered in Chapter 6, with the emphasis on time-dependent displacement of the wellbore wall. This chapter targets wellbore instability instances where the time-dependent borehole deformation is so excessive that the viscoelastic nature of the rock matrix must be explicitly considered in the modeling. Notable rock formations with this type of borehole failure are salt rock and shale. Some shales are known to cause repeated instability problems such as tight hole and stuck pipe despite repeated reaming and hole cleaning. Salt rock, on the other hand, can produce significant wellbore contraction and can even flow like a viscoelastic liquid under certain downhole conditions and the drilling engineers may have only a short time window to install the casing before the wellbore becomes inaccessible. The modeling and results of this chapter can be easily applied to other circular excavations such as tunnels and drill shafts.

1.5 Important Background Information

1.5.1 Assumptions

Only linear poroviscoelasticity will be considered in this study. This restriction ensures that an overall complex problem can be decomposed into elementary problems and the results for those simpler problems can be superposed to form the desired

solution. Furthermore, only small strains and displacements will be considered. More specifically, the formulation will be for infinitesimal strains and displacements.

1.5.2 Sign Convention

Throughout this dissertation, compressive stresses and strains are taken as positive.

1.5.3 Short-Hand Notation for Material Symmetry

The poroelastic constitutive relations with general anisotropy are as follows:

$$\sigma_{ij} = M_{ijkl}\varepsilon_{kl} + \alpha_{ij} p \,. \tag{1.1}$$

The short-hand notations for some frequently encountered classes of material symmetry are given below:

Orthotropic materials,

$$\sigma_{xx} = M_{11}\varepsilon_{xx} + M_{12}\varepsilon_{yy} + M_{13}\varepsilon_{zz} + \alpha_1 p \,, \tag{1.2}$$

$$\sigma_{yy} = M_{12}\varepsilon_{xx} + M_{22}\varepsilon_{yy} + M_{23}\varepsilon_{zz} + \alpha_2 p \,, \tag{1.3}$$

$$\sigma_{zz} = M_{13}\varepsilon_{xx} + M_{23}\varepsilon_{yy} + M_{33}\varepsilon_{zz} + \alpha_3 p \,, \tag{1.4}$$

$$\sigma_{xy} = 2M_{44}\varepsilon_{xy} \,, \tag{1.5}$$

$$\sigma_{xz} = 2M_{55}\varepsilon_{xz} \,, \tag{1.6}$$

$$\sigma_{yz} = 2M_{66}\varepsilon_{yz} \,, \tag{1.7}$$

$$p = M\left(\alpha_1\varepsilon_{xx} + \alpha_2\varepsilon_{yy} + \alpha_3\varepsilon_{zz} + \zeta\right). \tag{1.8}$$

Transversely isotropic materials,

$$\sigma_{xx} = M_{11}\varepsilon_{xx} + M_{12}\varepsilon_{yy} + M_{13}\varepsilon_{zz} + \alpha_1 p \,, \tag{1.9}$$

$$\sigma_{yy} = M_{12}\varepsilon_{xx} + M_{11}\varepsilon_{yy} + M_{13}\varepsilon_{zz} + \alpha_1 p \,, \tag{1.10}$$

$$\sigma_{zz} = M_{13}\varepsilon_{xx} + M_{13}\varepsilon_{yy} + M_{33}\varepsilon_{zz} + \alpha_3 p \,, \tag{1.11}$$

$$\sigma_{xy} = 2M_{44}\varepsilon_{xy}\,, \tag{1.12}$$

$$\sigma_{xz} = 2M_{55}\varepsilon_{xz}\,, \tag{1.13}$$

$$\sigma_{yz} = 2M_{55}\varepsilon_{yz}\,, \tag{1.14}$$

$$p = M\left(\alpha_1\varepsilon_{xx} + \alpha_1\varepsilon_{yy} + \alpha_3\varepsilon_{zz} + \zeta\right). \tag{1.15}$$

1.5.4 Frequently Used Parameters

Undrained stiffness coefficients:

$$M_{ij}^{u} = M_{ij} + \alpha_i\alpha_j M\,. \tag{1.16}$$

Frequently encountered material coefficient groups in analytical solutions:

$$\lambda_{ijk} = M_{ij}\alpha_k - M_{ik}\alpha_j\,. \tag{1.17}$$

1.5.5 Engineering Parameters

Familiar engineering parameters such as Young's moduli, shear moduli, and Poisson's ratios can be calculated from the stiffness coefficients using the following relations (Abousleiman and Cui, 2000):

For orthotropic materials, E_i denotes the Young's modulus in the x_i direction, G_{ij} denotes the shear modulus in the plane x_ix_j, and ν_{ij} denotes the Poisson's ratio associated with a compressive stress in the x_i direction and resulting tensile strain in the x_j direction,

$$M_{11} = \frac{E_1(\nu_{23}\nu_{12} - 1)}{D_d}\,, \tag{1.18}$$

$$M_{12} = -\frac{E_2(\nu_{13}\nu_{32} + \nu_{12})}{D_d}\,, \tag{1.19}$$

$$M_{13} = -\frac{E_3(v_{12}v_{23} + v_{13})}{D_d}, \tag{1.20}$$

$$M_{22} = \frac{E_2(v_{13}v_{31} - 1)}{D_d}, \tag{1.21}$$

$$M_{23} = -\frac{E_1(v_{13}v_{21} + v_{23})}{D_d}, \tag{1.22}$$

$$M_{33} = \frac{E_3(v_{12}v_{21} - 1)}{D_d}, \tag{1.23}$$

$$M_{44} = G_{12}, \tag{1.24}$$

$$M_{55} = G_{13}, \tag{1.25}$$

$$M_{66} = G_{23}, \tag{1.26}$$

with,

$$D_d = v_{21}v_{12} + v_{31}v_{13} + v_{23}v_{32} + v_{12}v_{23}v_{31} + v_{13}v_{32}v_{21} - 1. \tag{1.27}$$

For transversely isotropic materials, E_1 and E_3 denote the Young's moduli in the isotropic plane and the transverse direction, respectively, ν_1 and ν_3 are the Poisson's ratios in the isotropic plane and the transverse direction, respectively, and G_3 is the shear modulus in a plane through the material symmetry axis,

$$M_{11} = \frac{E_1(E_3 - E_1v_3^2)}{(1 + v_1)(E_3 - E_3v_1 - 2E_1v_3^2)}, \tag{1.28}$$

$$M_{12} = \frac{E_1(E_3v_1 + E_1v_3^2)}{(1 + v_1)(E_3 - E_3v_1 - 2E_1v_3^2)}, \tag{1.29}$$

$$M_{13} = \frac{E_1E_3v_3}{E_3 - E_3v_1 - 2E_1v_3^2}, \tag{1.30}$$

$$M_{33} = \frac{E_3^2(1 - v_1)}{E_3 - E_3v_1 - 2E_1v_3^2}, \tag{1.31}$$

$$M_{44} = G_1 = \frac{E_1}{2(1+\nu_1)}, \tag{1.32}$$

$$M_{55} = G_3 . \tag{1.33}$$

For isotropic materials, only two parameters, for example Young's modulus E and Poisson's ratio ν, are required to characterize the material mechanical behavior. The corresponding relations between stiffness coefficients and engineering parameters simplify as follows:

$$M_{11} = M_{22} = M_{33} = \frac{E(1-\nu)}{(1+\nu)(1-2\nu)}, \tag{1.34}$$

$$M_{12} = M_{13} = M_{23} = \frac{E\nu}{(1+\nu)(1-2\nu)}, \tag{1.35}$$

$$M_{44} = M_{55} = M_{66} = G = \frac{E}{2(1+\nu)} . \tag{1.36}$$

1.5.6 Laplace Transform and Carson Transform

Laplace transformation will be used extensively in this dissertation. For convenience, the tilde will be used to denote Laplace transform as shown below:

$$\widetilde{f} = L\{f(t)\} . \tag{1.37}$$

Carson transforms will also be used extensively for material parameters. The over bar will be used to denote Carson transform as follows:

$$\bar{f} = s\widetilde{f} . \tag{1.38}$$

1.5.7 Spring-Dashpot Models

Spring-dashpot models have been traditionally used to gain physical insights into a variety of viscoelastic behaviors. Using only simple linearly elastic springs (stress is

proportional to strain) and simple Newtonian dashpot (stress is proportional to strain rate), a wide range of viscoelastic behaviors can be simulated using an appropriate configuration.

An elegant method to find the material behavior of a particular spring-dashpot model is to construct its differential stress-strain relations in time domain and then apply the Laplace transform to obtain its Carson-transformed viscoelastic stiffness in Laplace transform domain. The Laplace-transformed stress-strain relation can be used to derive both the relaxation function and the creep function for that particular model. The relaxation function is obtained by substituting the Heaviside function for the strain (relaxation test) while the creep function is obtained by substituting the Heaviside function for the stress (creep test). A few examples demonstrating the technique are given below. The Young's modulus, E, was chosen in these example for illustration; other stiffness parameters can be modeled similarly.

1.5.7.1 Kelvin Model

The Kelvin model consists of a spring and a dashpot in parallel, as shown in **Fig. 1.1**.

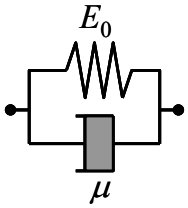

Fig. 1.1 – Kelvin model.

The differential stress-strain relation is therefore as follows:

$$\sigma = E_0\varepsilon + \mu\dot{\varepsilon}\,, \tag{1.39}$$

with the dot denoting time derivatives. Laplace transformation of the above equation gives,

$$\tilde{\sigma} = (E_0 + s\mu)\tilde{\varepsilon} \,. \tag{1.40}$$

The Carson-transformed viscoelastic Young's modulus is therefore,

$$\bar{E} = \frac{\tilde{\sigma}}{\tilde{\varepsilon}} = E_0 + s\mu \,. \tag{1.41}$$

The creep function for a Kelvin material is obtained by substituting the Heaviside function for the stress in Eq. (1.40), $\tilde{\sigma} = 1/s$, which leads to $\tilde{\varepsilon} = 1/s(E_0 + s\mu)$ or $\varepsilon = (1/E_0)(1 - e^{-E_0 t/\mu})$. The Kelvin model however gives an initial infinite stiffness if a stress is applied. Therefore, this model is not suitable for the modeling of the porous matrix for bio- or geo-materials.

1.5.7.2 Maxwell Model

The Maxwell model consists of a spring and a dashpot in series, as shown in **Fig. 1.2**.

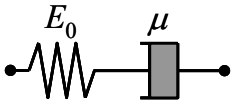

Fig. 1.2 – Maxwell model.

The differential stress-strain relations are therefore as follows:

$$\sigma = E_0\varepsilon_1, \sigma = \mu\dot{\varepsilon}_2, \varepsilon = \varepsilon_1 + \varepsilon_2 \,. \tag{1.42}$$

Therefore,

$$\dot{\varepsilon} = \frac{\dot{\sigma}}{E_0} + \frac{\sigma}{\mu} \,. \tag{1.43}$$

Laplace transformation of the above equation gives,

$$s\widetilde{\varepsilon} = \frac{s\widetilde{\sigma}}{E_0} + \frac{\widetilde{\sigma}}{\mu}. \tag{1.44}$$

The Carson-transformed viscoelastic Young's modulus is therefore,

$$\overline{E} = \frac{\widetilde{\sigma}}{\widetilde{\varepsilon}} = \frac{sE_0\mu}{E_0 + s\mu}. \tag{1.45}$$

The relaxation function for a Maxwell material is obtained by substituting Heaviside function for the strain in Eq. (1.44), $\widetilde{\varepsilon} = 1/s$, which leads to $\widetilde{\sigma} = E_0\mu/(E_0 + s\mu)$ or $\sigma = E_0 e^{-E_0 t/\mu}$. Since the Maxwell model gives infinite strain at long time if a stress is applied, it is limited to the modeling of bio or geo-materials with such behavior.

1.5.7.3 Zener (Standard Linear Solid) Models

The simplest spring-dashpot models that can simulate both relaxation and creep characteristics are the Zener or the standard linear solid models, as illustrated in **Fig. 1.3**. These models consist of two spring and one dashpot, with two possible configurations as shown in **Fig. 1.3a** and **Fig. 1.3b**.

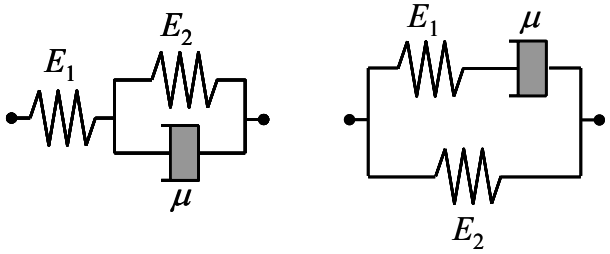

a) b)

Fig. 1.3 – Zener (standard linear solid) models.

For configuration a), the model consists of a spring in series with a Kelvin model. The stress-strain relation in Laplace transform domain is therefore as follows:

$$\widetilde{\varepsilon} = \frac{\widetilde{\sigma}}{E_1} + \frac{\widetilde{\sigma}}{E_2 + s\mu}. \tag{1.46}$$

The Carson-transformed viscoelastic Young's modulus is therefore,

$$\overline{E} = \frac{\widetilde{\sigma}}{\widetilde{\varepsilon}} = \frac{E_1 E_2 + sE_1\mu}{E_1 + E_2 + s\mu}. \tag{1.47}$$

For configuration b), the model consists of a spring in parallel with a Maxwell model. The stress-strain relation in Laplace transform domain is therefore as follows:

$$\widetilde{\sigma} = \frac{sE_1\mu}{E_1 + s\mu}\widetilde{\varepsilon} + E_2\widetilde{\varepsilon}. \tag{1.48}$$

The Carson-transformed viscoelastic Young's modulus is therefore,

$$\overline{E} = \frac{\widetilde{\sigma}}{\widetilde{\varepsilon}} = \frac{E_1 E_2 + s(E_1 + E_2)\mu}{E_1 + s\mu}. \tag{1.49}$$

The relaxation and creep functions are summarized in **Table 1.8**.

Table 1.8 – Time-domain properties of the Zener (standard linear solid) models.

Property	Configuration a)	Configuration b)
Relaxation function	$E_1 - \frac{E_1^2}{E_1 + E_2}[1 - e^{-(E_1+E_2)t/\mu}]$	$E_1 + E_2 - E_1(1 - e^{-E_1 t/\mu})$
Creep function	$\frac{1}{E_1}\left[1 + \frac{E_1}{E_2}(1 - e^{-E_2 t/\mu})\right]$	$\frac{1}{E_1 + E_2}\left\{1 + \frac{E_1}{E_2}\left[1 - e^{-\frac{E_1 E_2 t}{(E_1+E_2)\mu}}\right]\right\}$

It is easy to show that the two configurations are equivalent. Specifically, their parameters are related by the following relations:

$$E_1^a = E_1^b + E_2^b \tag{1.50}$$

$$E_2^a = \frac{E_2^b(E_1^b + E_2^b)}{E_1^b} \tag{1.51}$$

$$\mu^a = \mu^b \frac{(E_1^b + E_2^b)^2}{(E_1^b)^2} \tag{1.52}$$

Chapter 2: Correspondence Principle

2.1 Introduction

The theory of anisotropic poroviscoelasticity was developed by Biot (1956) based on his earlier work on anisotropic poroelasticity (Biot, 1955). This theory has received much attention recently as shown by an explosion of applications in both geomechanics (Abousleiman et al., 1996b; Schanz and Cheng, 2001; Wong et al., 2008; Hoang and Abousleiman, 2010) and biomechanics (Mak, 1986; Huang et al., 2001; Cheng and Bilston, 2007; Noailly et al., 2008; Hoang and Abousleiman, 2009a; Hoang and Abousleiman, 2010).

Biot (1956) also discovered a formal similarity between poroelasticity and poroviscoelasticity for the general case of matrix anisotropy using thermodynamics. However, the micromechanical aspects of this formal similarity were never investigated and the physical meaning of the macroscopic parameters remained obscure. Taylor and Aifantis (1982) and later Vgenopoulou and Beskos (1992) reestablished the correspondence principle between poroelasticity and poroviscoelasticity for isotropic media in Laplace transform domain. Abousleiman et al. (1993) used micromechanics considerations to show a similar correspondence between the poroelastic and poroviscoelastic Biot's effective stress coefficients, also for isotropic media. Coussy (1991, 1995) obtained correspondence relations in the time domain for general anisotropy and micromechanics relations for material parameters for isotropic media.

This chapter revisits anisotropic poroviscoelasticity using micromechanics. The correspondence principle is established in both time domain (Section 2.3) and Laplace transform domain (Section 2.4).

2.2 Review of Anisotropic Poroelasticity

In this section, some important relations in anisotropic poroelasticity (Cheng, 1997) are reproduced for later comparison with anisotropic poroviscoelasticity in Sections 2.3 and 2.4.

The constitutive relations for anisotropic poroelasticity can be written in pure compliance form as follows:

$$\varepsilon_{ij} = C_{ijkl}\sigma_{kl} - \frac{1}{3}CB_{ij}p\,, \tag{2.1}$$

$$\zeta = -\frac{1}{3}CB_{ij}\sigma_{ij} + Cp\,, \tag{2.2}$$

where ε_{ij} and σ_{ij} are the strain and stress tensors, respectively, C_{ijkl} is the compliance tensor, B_{ij} is the Skempton's coefficient tensor, p is the pore pressure, ζ is the variation of fluid content, C is the storage coefficient under constant total stress, and the Einstein convention for repeated indices is used.

From Eq. (2.1), the stresses can be expressed as functions of the strains and pore pressure by multiplying both sides with the stiffness tensor M_{ijkl} and simplifying,

$$\sigma_{ij} = M_{ijkl}\varepsilon_{kl} + \frac{1}{3}M_{ijkl}CB_{kl}p\,, \tag{2.3}$$

using the identity,

$$M_{ijkl}C_{klmn} = \frac{1}{2}\left(\delta_{im}\delta_{jn} + \delta_{in}\delta_{jm}\right), \tag{2.4}$$

where δ_{ij} is the Kronecker's delta. Comparison of Eq. (2.3) and the following familiar formula for total stresses,

$$\sigma_{ij} = M_{ijkl}\varepsilon_{kl} + \alpha_{ij}p\,, \tag{2.5}$$

where α_{ij} is the Biot's effective stress coefficient tensor, leads to,

$$\alpha_{ij} = \frac{1}{3} M_{ijkl} C B_{kl} , \tag{2.6}$$

which can be inverted to yield,

$$B_{ij} = 3 C_{ijkl} C^{-1} \alpha_{kl} . \tag{2.7}$$

Similarly, manipulation of Eq. (2.2) and comparison with the following familiar formula for pore pressure, with M is the inverse of the storage coefficient under constant volume,

$$p = M\zeta + M\alpha_{ij}\varepsilon_{ij} , \tag{2.8}$$

yields the following relation,

$$C = M^{-1} + \alpha_{ij}\alpha_{kl} C_{ijkl} . \tag{2.9}$$

The total strain and stress tensors can be decomposed into the solid (superscript s) and the pore (superscript p) components as follows:

$$\varepsilon_{ij} = (1-\phi)\varepsilon_{ij}^{s} + \phi\varepsilon_{ij}^{p} , \tag{2.10}$$

$$\sigma_{ij} = (1-\phi)\sigma_{ij}^{s} + \phi\delta_{ij} p , \tag{2.11}$$

where ϕ is the porosity.

The relationships between material coefficients of the porous medium and those of the constituents are explored next using a generalization of Nur and Byerlee's analysis (Nur and Byerlee, 1971). Consider an anisotropic micro-homogeneous porous medium with an arbitrary network of connected pores, subjected to a state of total stress σ_{ij} and pore pressure p. Due to the linearity of the mechanical behavior of the medium, this state of total stress and pore pressure can be decomposed into two modes of loading: a total stress $\sigma_{ij} - \delta_{ij} p$ without pore pressure and a pore pressure p and an equal confining pressure. The total strains due to the first mode of loading are as follows:

$$\varepsilon_{ij} = C_{ijkl}\sigma_{kl} - C_{ijkk}p\,. \tag{2.12}$$

From Eq. (2.11), the solid stress state is as follows:

$$\sigma_{ij}^{s} = \frac{1}{1-\phi}\left(\sigma_{ij} - \delta_{ij}p\right), \tag{2.13}$$

which gives rise to the following solid strains:

$$\varepsilon_{ij}^{s} = C_{ijkl}^{s}\sigma_{kl}^{s}\,, \tag{2.14}$$

where C_{ijkl}^{s} denotes the compliance tensor of the solid. The existence of the compliance tensor of the solid phase is a consequence of the micro-homogeneity of the porous medium. The pore strains due to this mode of loading can then be calculated using Eq. (2.10),

$$\varepsilon_{ij}^{p} = \frac{1}{\phi}\left(C_{ijkl} - C_{ijkl}^{s}\right)\sigma_{kl} - \frac{1}{\phi}\left(C_{ijkk} - C_{ijkk}^{s}\right)p\,. \tag{2.15}$$

For the second mode of loading, i.e., pore pressure p and an equal confining pressure, following Nur and Byerlee (1971), we consider first a homogeneous solid with the pores filled with the same solid material. When this domain is subjected to the confining pressure p, the following state of strain is obtained:

$$\varepsilon_{ij}^{s} = C_{ijkk}^{s}p\,. \tag{2.16}$$

This confining pressure causes a hydrostatic pressure p everywhere in the solid. Therefore, using the uniqueness theorem for stress boundary value problems of anisotropic elastic bodies (see for example Ezzat and El-Karamany (2002)), we can replace the material inside the original pores with fluid while maintaining the same pore pressure and obtain the same deformation field in the solid. In other words,

$$\varepsilon_{ij} = \varepsilon_{ij}^{p} = \varepsilon_{ij}^{s} = C_{ijkk}^{s}p\,. \tag{2.17}$$

Using the principle of superposition, the total strains and the pore strains due to the two modes of loading can be found as follows:

$$\varepsilon_{ij} = C_{ijkl}\sigma_{kl} - \left(C_{ijkk} - C^s_{ijkk}\right)p\,, \tag{2.18}$$

$$\varepsilon^p_{ij} = \frac{1}{\phi}\left(C_{ijkl} - C^s_{ijkl}\right)\sigma_{kl} - \left(\frac{1}{\phi}C_{ijkk} - \frac{1+\phi}{\phi}C^s_{ijkk}\right)p\,. \tag{2.19}$$

Comparison of Eqs. (2.1) and (2.18) yields,

$$B_{ij} = \frac{3\left(C_{ijkk} - C^s_{ijkk}\right)}{C}. \tag{2.20}$$

The Biot's effective stress coefficient tensor can then be calculated using Eq. (2.6),

$$\alpha_{ij} = \delta_{ij} - M_{ijkl}C^s_{klmm}\,. \tag{2.21}$$

From Eq. (2.19), the variation of fluid content ζ can be found using the following consideration:

$$\varepsilon^p_{ii} = e^{fluid} = e^{fluid}_{compressibility} - e^{fluid}_{fluid\ content}$$

$$\varepsilon^p_{ii} = C_f p - \frac{\zeta}{\phi}\,, \tag{2.22}$$

with e and C_f denoting the volumetric strain and fluid bulk modulus, respectively. The variation of fluid content takes the form:

$$\zeta = -\left(C_{ijkl} - C^s_{ijkl}\right)\sigma_{kl} + \left(C_{ijkk} - C^s_{ijkk}\right)p + \phi\left(C_f - C^s_{ijkk}\right)p\,. \tag{2.23}$$

Comparison with Eq. (2.2) yields,

$$C = \left(C_{ijkk} - C^s_{ijkk}\right) + \phi\left(C_f - C^s_{ijkk}\right). \tag{2.24}$$

Finally, Eq. (2.9) gives the expression for M:

$$M^{-1} = M_{ijmn}C^s_{mnll}\left(C_{ijkk} - C^s_{ijkk}\right) + \phi\left(C_f - C^s_{ijkk}\right). \tag{2.25}$$

The material coefficients α_{ij}, B_{ij}, C, and M given above can be further simplified for porous media having micro-isotropy or material symmetry (orthotropy, transversely isotropy, isotropy, etc.) (Cheng, 1997).

2.3 Poroviscoelasticity in Time Domain

A similar treatment for linear poroviscoelastic media will be given in this section. We start with the constitutive relations in pure compliance form ("creep" formulation),

$$\varepsilon_{ij} = C_{ijkl} \otimes \sigma_{kl} - \frac{1}{3} A_{ij} \otimes p \,, \tag{2.26}$$

$$\zeta = -\frac{1}{3} A_{ij} \otimes \sigma_{ij} + C \otimes p \,, \tag{2.27}$$

where the symbol $\otimes$ denotes the Stieltjes convolution product,

$$f(t) \otimes g(t) = \int_{-\infty}^{t} f(t-\tau) dg(\tau) . \tag{2.28}$$

Eqs. (2.26) and (2.27) are written in the general form for linear poroviscoelasticity and the nature of A_{ij} will be made clear shortly through micromechanical analysis. In place of Eqs. (2.5) and (2.8), we have the following general relations:

$$\sigma_{ij} = M_{ijkl} \otimes \varepsilon_{kl} + \alpha_{ij} \otimes p \,, \tag{2.29}$$

$$p = M \otimes \zeta + Q_{ij} \otimes \varepsilon_{ij} \,. \tag{2.30}$$

The nature of Q_{ij} will also be explored later. Inverting Eq. (2.26) gives the stresses in terms of strains and pore pressure,

$$\sigma_{ij} = M_{ijkl} \otimes \varepsilon_{kl} + \frac{1}{3} M_{ijkl} \otimes A_{kl} \otimes p \,, \tag{2.31}$$

where M_{ijkl} is the inverse of the C_{ijkl} with respect to the convolution product,

$$M_{ijkl} \otimes C_{klmn} = \frac{1}{2}\left(\delta_{im}\delta_{jn} + \delta_{in}\delta_{jm}\right)H(t), \tag{2.32}$$

with $H(t)$ is the Heaviside step function. In this chapter, for brevity, the Heaviside step function will not be written explicitly except when required to prevent ambiguity. Comparison of Eqs. (2.29) and (2.31) yields,

$$\alpha_{ij} = \frac{1}{3} M_{ijkl} \otimes A_{kl}, \tag{2.33}$$

which can be inverted to give,

$$A_{ij} = 3C_{ijkl} \otimes \alpha_{kl}, \tag{2.34}$$

Similarly, comparison of Eq. (2.30) and the inversion of Eq. (2.27) provides the following identities:

$$C = M^{-1} + C_{ijkl} \otimes \alpha_{ij} \otimes \alpha_{kl}, \tag{2.35}$$

$$Q_{ij} = M \otimes \alpha_{ij}. \tag{2.36}$$

The second identity transforms Eq. (2.30) to the following form:

$$p = M \otimes \zeta + M \otimes \alpha_{ij} \otimes \varepsilon_{ij}. \tag{2.37}$$

Using the uniqueness theorem for stress boundary and initial value problems of anisotropic viscoelastic bodies (Ezzat and El-Karamany (2002)), a generalization of Nur and Byerlee's analysis similar to the one for anisotropic poroelasticity presented in Section 2.2 can be constructed to yield the following relations:

$$A_{ij} = 3\left(C_{ijkk} - C^s_{ijkk}\right), \tag{2.38}$$

$$\alpha_{ij} = \delta_{ij} - M_{ijkl} \otimes C^s_{klmm}, \tag{2.39}$$

$$C = \left(C_{ijkk} - C^s_{ijkk}\right) + \phi\left(C_f - C^s_{ijkk}\right), \tag{2.40}$$

$$M^{-1} = M_{ijmn} \otimes C^s_{mnll} \otimes \left(C_{ijkk} - C^s_{ijkk}\right) + \phi\left(C_f - C^s_{ijkk}\right). \tag{2.41}$$

From Eq. (2.38), we can formally define,

$$B_{ij} = A_{ij} \otimes C^{-1}, \tag{2.42}$$

or,

$$B_{ij} = 3\left(C_{ijkk} - C^{s}_{ijkk}\right) \otimes C^{-1}, \tag{2.43}$$

then Eqs. (2.26) and (2.27) become,

$$\varepsilon_{ij} = C_{ijkl} \otimes \sigma_{kl} - \frac{1}{3} C \otimes B_{ij} \otimes p, \tag{2.44}$$

$$\zeta = -\frac{1}{3} C \otimes B_{ij} \otimes \sigma_{ij} + C \otimes p, \tag{2.45}$$

The physical meaning of B_{ij} becomes apparent when we let $\zeta = 0$ in Eq. (2.45) ("undrained" condition),

$$p = \frac{1}{3} B_{ij} \otimes \sigma_{ij}, \tag{2.46}$$

or B_{ij} is the poroviscoelastic Skempton's coefficient tensor.

Comparison of poroelastic and poroviscoelastic constitutive relations and the micromechanical expressions of material coefficients leads to the following correspondence principle in time domain:

Correspondence principle in time domain: *Any constitutive relation or formula for material coefficients of anisotropic linear poroviscoelasticity can be obtained from the corresponding expression in anisotropic linear poroelasticity by replacing multiplication with the Stieltjes convolution product.*

Coussy (1991, 1995) obtained the same conclusions about the constitutive relations of anisotropic poroviscoelasticity. However, he only provided formulas for material coefficients for the special case of isotropic media.

2.4 Poroviscoelasticity in Laplace Transform Domain

The following elementary table of poroelastic and poroviscoelastic formulas in time domain and Laplace transform domain can be easily derived:

Table 2.1 – Comparison of poroelastic and poroviscoelastic formulas in time domain and Laplace transform domain.

Poroelasticity (t)	Poroelasticity (s)	Poroviscoelasticity (t)	Poroviscoelasticity (s)
$(a_1 \pm a_2) f(t)$	$(a_1 \pm a_2)\tilde{f}(s)$	$[a_1(t) \pm a_2(t)] \otimes f(t)$	$[\bar{a}_1(s) \pm \bar{a}_2(s)]\tilde{f}(s)$
$a_1 \cdot a_2 \cdot f(t)$	$a_1 \cdot a_2 \cdot \tilde{f}(s)$	$a_1(t) \otimes a_2(t) \otimes f(t)$	$\bar{a}_1(s) \cdot \bar{a}_2(s) \cdot \tilde{f}(s)$
$\frac{a_1}{a_2} f(t)$	$\frac{a_1}{a_2}\tilde{f}(s)$	$a_1(t) \otimes a_2^{-1}(t) \otimes f(t)$	$\frac{\bar{a}_1(s)}{\bar{a}_2(s)}\tilde{f}(s)$

where s is the Laplace transform variable, the tilde and the bar accents denote Laplace transform and Carson transform, respectively. Using these elementary formulas, more complex relations can be easily obtained. In particular, Laplace transformation of Eqs. (2.44), (2.45), (2.29), (2.37), (2.39), (2.43), (2.35), and (2.41) provides respectively,

$$\tilde{\varepsilon}_{ij} = \bar{C}_{ijkl}\tilde{\sigma}_{kl} - \frac{1}{3}\bar{C}\,\bar{B}_{ij}\tilde{p}\,, \tag{2.47}$$

$$\tilde{\zeta} = -\frac{1}{3}\bar{C}\,\bar{B}_{ij}\tilde{\sigma}_{ij} + \bar{C}\,\tilde{p}\,, \tag{2.48}$$

$$\tilde{\sigma}_{ij} = \bar{M}_{ijkl}\tilde{\varepsilon}_{kl} + \bar{\alpha}_{ij}\tilde{p}\,, \tag{2.49}$$

$$\tilde{p} = \bar{M}\,\tilde{\zeta} + \bar{M}\,\bar{\alpha}_{ij}\tilde{\varepsilon}_{ij}\,, \tag{2.50}$$

$$\bar{\alpha}_{ij} = \delta_{ij} - \bar{M}_{ijkl}\bar{C}^{s}_{klmm}\,, \tag{2.51}$$

$$\bar{B}_{ij} = \frac{3\left(\bar{C}_{ijkk} - \bar{C}^{s}_{ijkk}\right)}{\bar{C}}, \tag{2.52}$$

$$\bar{C} = \frac{1}{\bar{M}} + \bar{C}_{ijkl}\bar{\alpha}_{ij}\bar{\alpha}_{kl}\,, \tag{2.53}$$

$$\frac{1}{\overline{M}} = \overline{M}_{ijmn}\overline{C}^{s}_{mnll}\left(\overline{C}_{ijkk} - \overline{C}^{s}_{ijkk}\right) + \phi\left(C_f - \overline{C}^{s}_{ijkk}\right). \tag{2.54}$$

It is clear that any formula in anisotropic linear poroviscoelasticity can be obtained from the corresponding expression in anisotropic linear poroelasticity by replacing poroelastic material coefficients with the Carson transform of the poroviscoelastic counter parts. Since for the same boundary and initial value problem, other equations for the poroelastic and poroviscoelastic formulations are identical, we have the following correspondence principle in Laplace transform domain:

Correspondence principle in Laplace transform domain: *The formulation and solution to the same boundary and initial value problem in anisotropic linear poroviscoelasticity can be obtained from those in poroelasticity by replacing poroelastic material coefficients with the Carson transform of the poroviscoelastic counterparts.*

Similar observations for the special case of material isotropy has been presented by Taylor and Aifantis (1982), Vgenopoulou and Beskos (1992), and Abousleiman et al. (1993). It is also noted that while the correspondence principle between poroelasticity and poroviscoelasticity will be most useful to find poroviscoelastic solutions from existing poroelastic ones, it can be used in the other direction to generate the poroelastic solution if the poroviscoelastic solution to the same boundary and initial value problem is available.

2.5 Numerical Examples – Biot's Effective Stress Coefficients

Armed with the correspondence principle between poroviscoelasticity and poroelasticity, the formulas for material coefficients of anisotropic poroviscoelasticity

can be immediately obtained from those of anisotropic poroelasticity (for example Cheng (1997)). Of particular interest are the Biot's effective stress coefficients α_{ij}, as listed below:

$$\overline{\alpha}_{ij} = \delta_{ij} - \overline{M}_{ijkl}\overline{C}^{s}_{klmm} . \tag{2.55}$$

A few examples are given below to demonstrate the intricate behavior of the poroviscoelastic Biot's effective stress coefficients in time domain. For sedimentary rocks with material transverse isotropy and elastic micro-isotropic grains, α_{ij} simplifies as follows in short-hand notation:

$$\overline{\alpha}_1 = 1 - \frac{\overline{M}_{11} + \overline{M}_{12} + \overline{M}_{13}}{3K_s}, \tag{2.56}$$

$$\overline{\alpha}_3 = 1 - \frac{2\overline{M}_{13} + \overline{M}_{33}}{3K_s}. \tag{2.57}$$

It has been reported that the characteristic time of creep for many rocks including shale, siltstone, and sandstone, falls in the range of 10 to 15 hours (Warpinski and Teufel, 1989). In the following example, all matrix drained moduli $M_{ij}(t)$ are assumed to behave according to the Zener model with the same characteristic creep time of 10 hours. Initial stiffness coefficients are assumed as follows: $M_{11}(0^+)$ = 11.93 GPa, $M_{12}(0^+)$ = 4.93 GPa, $M_{13}(0^+)$ = 3.37 GPa, and $M_{33}(0^+)$ = 5.90 GPa. All moduli are assumed to retain 50% of initial values at long time. The matrix grain bulk modulus is assumed to have insignificant viscoelasticity, K_s = 40 GPa. Since the bulk moduli are monotonically decreasing and K_s is constant, the Biot's effective stress coefficients are monotonically increasing, as shown in **Fig. 2.1**.

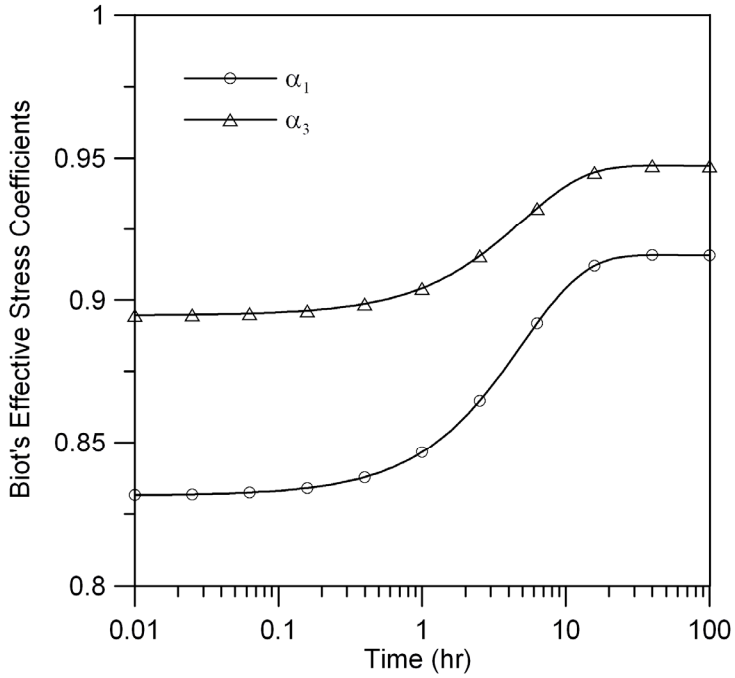

Fig. 2.1 – Biot's effective stress coefficients for a transversely isotropic rock with elastic K_s.

On the other hand, K_s could be viscoelastic for biological tissues. For micro-isotropic biomaterials, the Biot's effective stress coefficients simplify as follows:

$$\overline{\alpha}_1 = 1 - \frac{\overline{M}_{11} + \overline{M}_{12} + \overline{M}_{13}}{3\overline{K}_s}, \tag{2.58}$$

$$\overline{\alpha}_3 = 1 - \frac{2\overline{M}_{13} + \overline{M}_{33}}{3\overline{K}_s}. \tag{2.59}$$

A transversely isotropic articular cartilage with the following properties will be considered: $M_{11}(0^+)$ = 0.56 MPa, $M_{12}(0^+)$ = 0.032 MPa, $M_{13}(0^+)$ = 0.029 MPa, and $M_{33}(0^+)$ = 1.2 MPa. For simplicity of illustration, all moduli are assumed to follow the Zener model with the same characteristic relaxation time of 60 seconds and to retain 50% of initial values at long time. The matrix grain bulk modulus is also assumed to behave according to the Zener model with an initial value of 3.0 MPa. Three different long-time to short-time ratios of 2/3, 0.5, and 1/3 and three different characteristic

relaxation times T_{K_s} of 30, 60, and 600 seconds are considered for K_s in the following analysis.

For $T_{K_s} = 60\,\text{s}$ which is the same as the characteristic relaxation time of the bulk moduli, α_1 and α_3 either stay constant or vary monotonically as shown in **Fig. 2.2**. The Biot's effective stress coefficients increase when the percentage decrease in K_s is less than that in the bulk moduli and vice versa.

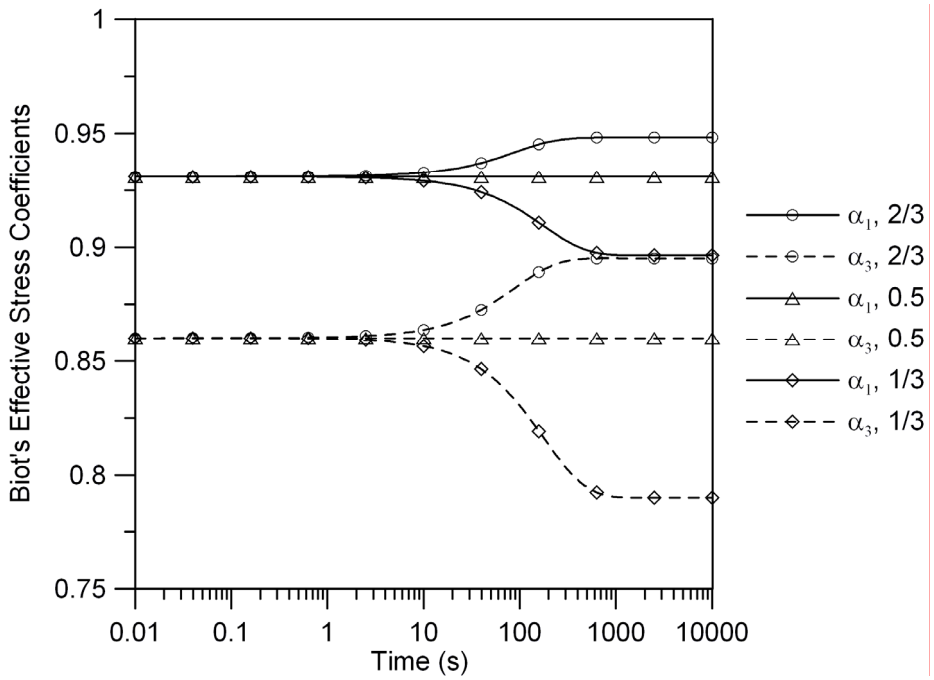

Fig. 2.2 – Biot's effective stress coefficients for a transversely isotropic articular cartilage, characteristic relaxation time of K_s is 60 s.

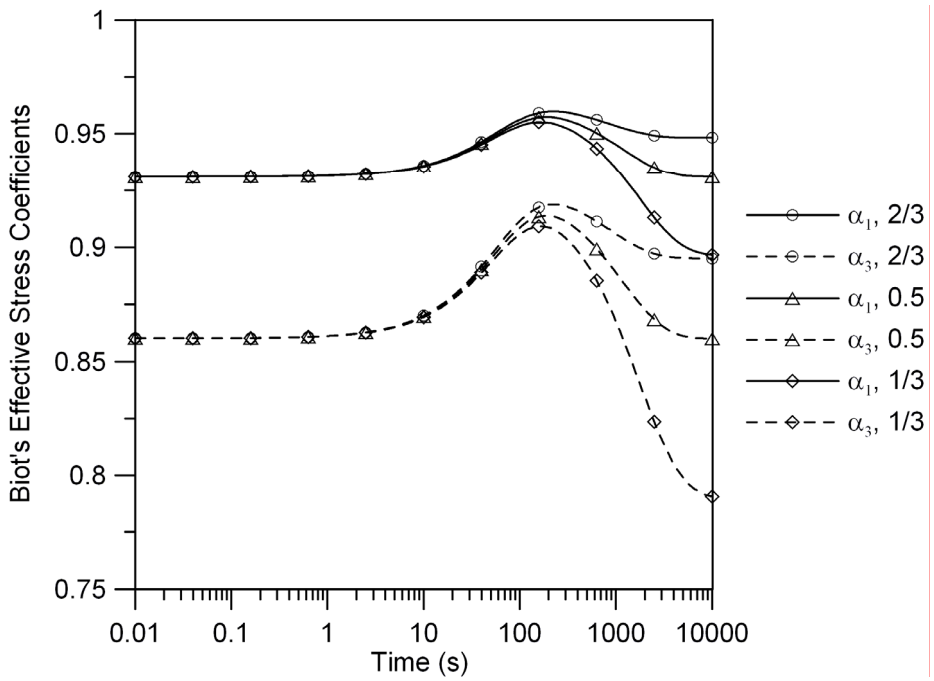

Fig. 2.3 – Biot's effective stress coefficients for a transversely isotropic articular cartilage, characteristic relaxation time of K_s is 600 s.

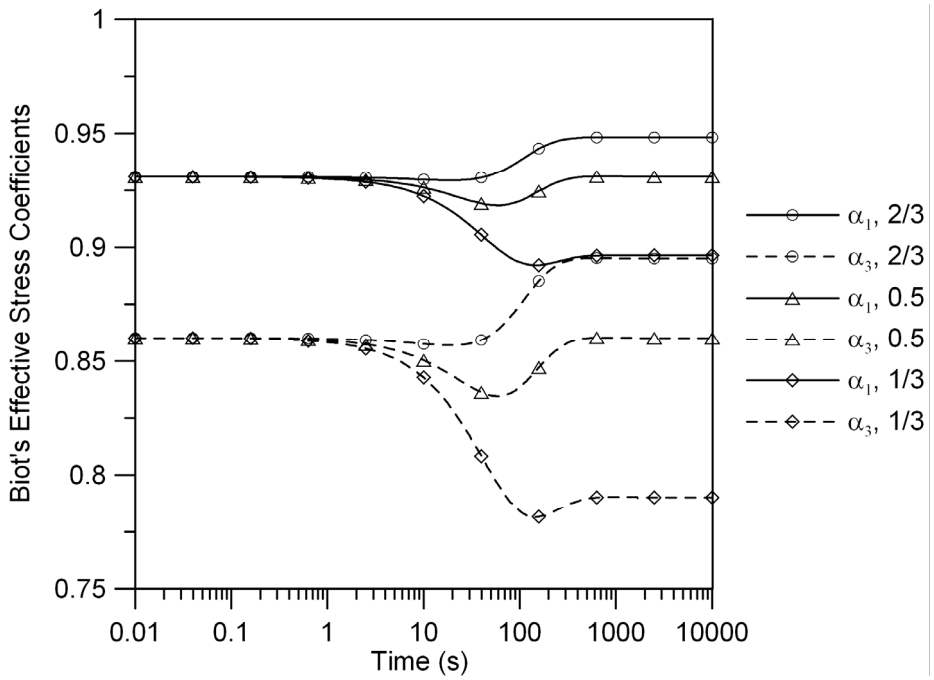

Fig. 2.4 – Biot's effective stress coefficients for a transversely isotropic articular cartilage, characteristic relaxation time of K_s is 30 s.

For a longer $T_{K_s} = 600\,\mathrm{s}$, the time-dependent variations of α_1 and α_3 are no longer monotonic, as shown in **Fig. 2.3**. Compared to the case of $T_{K_s} = 60\,\mathrm{s}$, α_1 and α_3 obtain

the same short-time and long-time values. However, in intermediate times, since K_s decays more slowly than the bulk moduli, α_1 and α_3 are higher than the case of $T_{K_s} = 60\,\text{s}$. The reverse is observed for a shorter $T_{K_s} = 30\,\text{s}$ as shown in **Fig. 2.4**. This complex interplay between the bulk moduli and the grain bulk modulus on the Biot's effective stress coefficients has been observed earlier for isotropic materials (Abousleiman et al., 1993).

Chapter 3: Transversely Isotropic Cylinders[1]

3.1 Introduction

In both laboratory and field testing, cylinders are one of the most common sample geometries. Moreover, for transversely isotropic materials, which are abundant in both biomechanics and geomechanics, material characterization testing using cylinders with axis of geometrical symmetry coinciding with axis of mechanical symmetry becomes a natural choice. This chapter will investigate the poroviscoelastic behavior of such specimens under some of the most common laboratory settings: unconfined compression, confined compression, unjacketed triaxial, jacketed triaxial, and oedometer tests. A special field test with very important applications in the petroleum industry, the strain recovery method, is also analyzed herein.

Following this introduction is a description of the testing configurations in Section 3.2. Section 3.3 presents the analytical solutions of the sample behavior under such settings. Finally, Sections 3.4 and 3.5 give some numerical examples and discussion on this class of engineering problems.

3.2 Problem Description

3.2.1 Laboratory Testing: Unconfined Compression Test, Triaxial Test, K_0 (Oedometer) Test, and Confined Compression Test

Fig. 3.1a shows a cylindrical sample with radius R and height H and an attached coordinate system. **Fig. 3.1b** shows the sample under the conventional unconfined compression test, with a general time-dependent axial load $F(t)$ (load control) or an apparent axial strain $\varepsilon_{zz}(t)$ (stroke control) applied through the perfectly rigid,

[1] Parts of this chapter have been published in Hoang and Abousleiman (2009b) and Hoang and Abousleiman (2010)

frictionless, and impermeable end caps. **Fig. 3.1c** demonstrates the unjacketed triaxial test, with the addition of a time-dependent confining pressure $P_o(t)$. **Fig. 3.1d** shows a general jacketed triaxial loading configuration, with the sample subjected to both confining pressure $P_o(t)$ and pore pressure $p_o(t)$ using a two-jacket system. It is worth noting that the modeling of the jacketed triaxial test can be used to simulate both the unjacketed triaxial test and the unconfined compression test. Specifically, we recover the unjacketed triaxial test when $P_o(t) = p_o(t)$, and the unconfined compression test when $P_o(t) = p_o(t) = 0$. **Fig. 3.1e** shows the sample confined by rigid, frictionless, and impermeable bottom plate and lateral ring while being loaded on top using a porous loading plate. This configuration is the popular confined compression test in biomechanics research. Finally, **Fig. 3.1f** illustrates the K_0 or oedometer test in soil mechanics, with the sample sandwiched between two porous loading plates and confined laterally by a rigid and impermeable ring. It is evident that for the laboratory configuration in **Fig. 3.1f**, the mid-height plane is a plane of symmetry with no in-plane shear stresses or transverse pore fluid flux. In other words, from a physical as well as a mathematical point of view, either the top or the bottom half of a sample subjected to the oedometer test can be modeled using the confined test. Therefore, the oedometer test will not be explicitly discussed in this paper. Interested readers are referred to the discussion on the confined compression test. Material-wise, the tested sample is transversely isotropic, with the axis of material symmetry coinciding with the axis of geometrical symmetry.

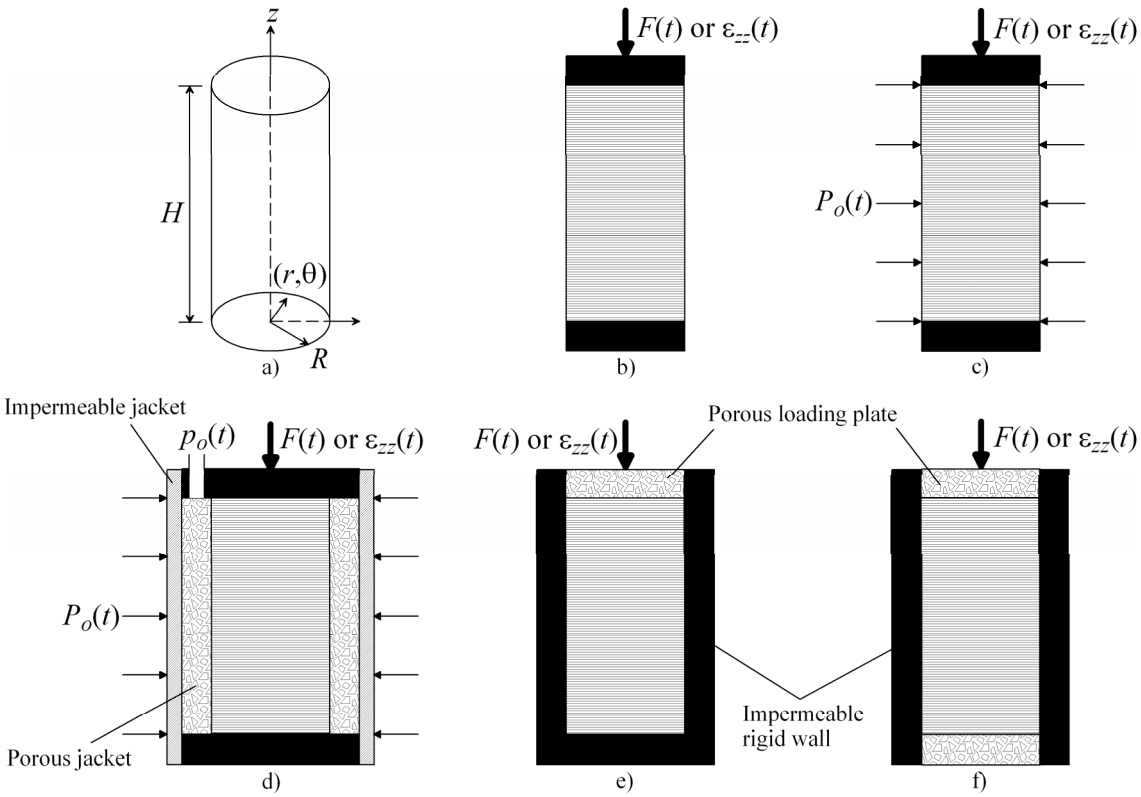

Fig. 3.1 – Schematic of compression testing of anisotropic cylindrical samples, a) sample dimensions and coordinate system, b) unconfined compression test, c) unjacketed triaxial test, d) jacketed triaxial test, e) confined compression test, f) oedometer test.

For the unconfined compression, unjacketed triaxial, or jacketed triaxial setup, the boundary conditions at $r = R$ are as follows:

$$\sigma_{rr} = P_o(t),\ p = p_o(t),\ \sigma_{r\theta} = \sigma_{rz} = 0\,. \tag{3.1}$$

The boundary conditions at the two ends are as follows:

$$q_z = 0,\ \sigma_{zr} = \sigma_{z\theta} = 0,\ u_z\big|_{z=0} = 0\,. \tag{3.2}$$

Finally, equilibrium condition in the z direction requires,

$$F(t) = \int_0^R 2\pi\sigma_{zz} r dr\,. \tag{3.3}$$

With the aforementioned conditions, the experimental setup becomes a generalized plane-strain axisymmetric problem, with all shear stresses and shear strains vanish, and all dynamic and kinematic variables except u_z independent of z.

On the other hand, for the confined compression test, the boundary conditions at the top are as follows:

$$p = 0, \sigma_{zr} = \sigma_{z\theta} = 0 . \tag{3.4}$$

The boundary conditions at the bottom are as follows:

$$q_z = 0, \sigma_{zr} = \sigma_{z\theta} = 0, u_z = 0 . \tag{3.5}$$

The boundary conditions on the lateral surface are as follows:

$$q_r = 0, \sigma_{rz} = \sigma_{r\theta} = 0, u_r = 0 . \tag{3.6}$$

Equilibrium condition in the z direction still requires Eq. (3.3) to hold. With the aforementioned conditions, the experimental setup becomes a one-dimensional problem in the z direction with all shear stresses and shear strains vanish, $\varepsilon_{rr} = \varepsilon_{\theta\theta} = 0$, $q_r = q_\theta = 0$, and all non-zero dynamic and kinematic variables dependent upon z and t only.

3.2.2 Field Testing: Strain Recovery Method

The importance of accurate determination of in-situ maximum and minimum horizontal stress orientations and magnitudes can never be over-emphasized in geomechanics-related operations in the oil and gas industry. An accurate estimate of the in-situ stress state is critical throughout the reservoir life cycle, from basin characterization at the very beginning to flow anisotropy modeling in reservoirs, borehole stability study for well drilling, hydraulic fracturing for reservoir stimulation, sand/solids production during oil and gas production, and modeling and prediction of earthquakes induced by the extraction of oil and gas from underground formations.

The strain recovery method was first proposed by Voight (1968) for estimating in-situ stress orientations and magnitudes from cores retrieved from shallow and dry wellbores. Since then, several analyses of the technique using viscoelasticity theory have been conducted for isotropic rock formations (Blanton, 1983; Warpinski and Teufel, 1989). Unfortunately, for the petroleum industry, wells are much deeper and both the well and the surrounding rock formation are filled with fluid. Therefore, viscoelastic analyses are inherently inadequate. Instead, poroviscoelastic modeling and simulation should be used, yet the early attempts to include pore pressure in such problems fell short from any real field conditions (Abousleiman and Cheng, 1996).

The complexity of the application of the strain recovery method to real field cases is further compounded by the anisotropy frequently exhibited by rock formations. In particular, the commonly encountered transverse isotropy of many sandstones, siltstones, shales, etc., could significantly influence the coupled responses including pore pressure generation and relaxation behavior. An attempt to incorporate the rock transverse isotropy into the analysis was made by Blanton and Teufel (1983) with many simplifying assumptions.

Furthermore, the actual stress and pressure evolution imposed on the retrieved cores are time-dependent functions, depending on not only in-situ state of stress but also on operational details such as core retrieval time. All existing analyses simplify the actual time-dependent boundary conditions to sudden unloading of the core. This simplified unloading scenario clearly does not portray real field conditions and could lead to misinterpretation of the strain recovery data.

This study aims to simulate the poroviscoelastic transversely isotropic relaxation of a drill core from a vertical well, from the time it is cored, during retrieval, and during sample monitoring in laboratory conditions, using realistic time-dependent stress and pressure unloading conditions.

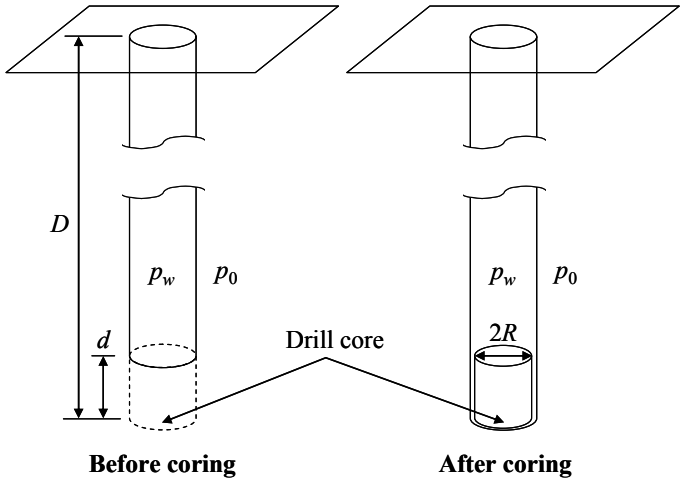

Fig. 3.2 – Problem schematic of the strain recovery method, not to scale.

A schematic of the problem is presented in **Fig. 3.2**. A vertical wellbore is cored to a depth D, with a retrieved core of length d and radius R. For most field cases, $D >> d >> 2R$. Typical ranges for D, d, and R are hundreds to thousands of meters, tens of meters, and centimeters to tens of centimeters, respectively. For balanced drilling, the wellbore pressure p_w and the formation pore pressure p_0 are equal. Following field practice, the study will focus on the behavior of the core section close to the bottom of the coring barrel.

The stress state of this core section at the start of coring is as follows:

$$\sigma_{zz} = S_V, \sigma_{rr} = S_r, \sigma_{r\theta} = S_{r\theta}, p = p_0, \tag{3.7}$$

where S_V is the overburden stress, S_r and $S_{r\theta}$ are the radial and shear in-situ stresses, and p_0 is the formation pore pressure. S_r and $S_{r\theta}$ relate to the minimum and maximum horizontal in-situ stresses S_{hmin} and S_{Hmax} as follows:

$$S_r = \frac{S_{Hmax} + S_{hmin}}{2} + \frac{S_{Hmax} - S_{hmin}}{2} \cos 2\left(\theta - \theta_{S_H}\right),$$

$$S_r = \frac{S_{Hmax} + S_{hmin}}{2} + \frac{S_{Hmax} - S_{hmin}}{2} \cos 2\left(\theta - \theta_{S_H}\right), \tag{3.8}$$

with θ is the azimuth around the core and θ_{S_H} is the azimuth of the maximum horizontal in-situ stress.

The stress state of the same core section at the end of coring is as follows:

$$\sigma_{zz} = p_w, \sigma_{rr} = p_w, \sigma_{r\theta} = 0, p = p_0 . \tag{3.9}$$

Finally, at the end of the retrieval, all stresses and pore pressure on the core surface vanish. In this study, the time interval from the end of coring to the end of retrieval is termed retrieval time while the time interval from the end of retrieval to the beginning of sample relaxation monitoring is termed sample preparation time.

Since the core length is much greater than the core diameter, pore pressure diffusion will occur predominantly in the radial direction. The relaxation behavior, therefore, can be examined using generalized plane-strain analysis, provided that relaxation data are measured not too close from the bottom of retrieved core.

3.3 Poroviscoelastic Analytical Solutions

3.3.1 Review of Relevant Analytical Solutions

Relevant studies on one-dimensional consolidation problem are summarized in **Table 3.1**. Biot investigated this problem as an example of application in both his 1941 paper on poroelasticity and his 1956 paper on poroviscoelasticity. Mak (1986) revisited the poroviscoelastic 1-D consolidation problem when he investigated the behavior of articular cartilage under confined compression testing. Recently, Schanz and Cheng (2001) incorporated dynamic effects in the analysis. All of the aforementioned solutions

concern only isotropic materials. This study extends the analysis to transversely isotropic materials.

Table 3.1 – Relevant studies on one-dimensional consolidation.

Anisotropy	Poroelasticity	Poroviscoelasticity
Isotropy	Biot, 1941	Biot, 1956 Mak, 1986 Schanz and Cheng, 2001
Transverse isotropy		This study

Table 3.2 – Relevant studies on cylindrical geometry.

Anisotropy	Poroelasticity	Poroviscoelasticity
Isotropy	Armstrong et al., 1984 Cui and Abousleiman, 2001 Sawaguchi and Kurashige, 2005	Abousleiman et al., 1996b Abousleiman and Cheng, 1996 Huang et al., 2001
Transverse isotropy	Abousleiman and Cui, 1998 Zwanenburg and Barends, 2007 Cowin and Mehrabadi, 2007	This study

Similarly, relevant studies on the behavior of poroelastic and poroviscoelastic cylinders are summarized in **Table 3.2**. Many authors have worked on the subject due to the practical importance of this class of problem in both geomechanics and biomechanics. Armed with the correspondence principle of poroviscoelasticity and poroelasticity established in Chapter 2, the analytical solutions for poroelastic transversely isotropic cylinders given by Abousleiman and Cui (1998) will be the most useful; these results can be readily transferred to poroviscoelasticity to obtain the desired solutions for poroviscoelastic transversely isotropic cylindrical samples under testing conditions. It is noted that the sign convention has been changed from tension positive in Abousleiman and Cui (1998) to compression positive in this study. Consequently, the derivation of the analytical solutions will be presented in details for completeness.

3.3.2 Governing Equations

The constitutive relations in cylindrical coordinates for a transversely isotropic poroviscoelastic material are as follows:

$$\widetilde{\sigma}_{rr} = \overline{M}_{11}\widetilde{\varepsilon}_{rr} + \overline{M}_{12}\widetilde{\varepsilon}_{\theta\theta} + \overline{M}_{13}\widetilde{\varepsilon}_{zz} + \overline{\alpha}_1\widetilde{p}\,, \tag{3.10}$$

$$\widetilde{\sigma}_{\theta\theta} = \overline{M}_{12}\widetilde{\varepsilon}_{rr} + \overline{M}_{11}\widetilde{\varepsilon}_{\theta\theta} + \overline{M}_{13}\widetilde{\varepsilon}_{zz} + \overline{\alpha}_1\widetilde{p}\,, \tag{3.11}$$

$$\widetilde{\sigma}_{zz} = \overline{M}_{13}\widetilde{\varepsilon}_{rr} + \overline{M}_{13}\widetilde{\varepsilon}_{\theta\theta} + \overline{M}_{33}\widetilde{\varepsilon}_{zz} + \overline{\alpha}_3\widetilde{p}\,, \tag{3.12}$$

$$\widetilde{p} = \overline{\alpha}_1\overline{M}\widetilde{\varepsilon}_{rr} + \overline{\alpha}_1\overline{M}\widetilde{\varepsilon}_{\theta\theta} + \overline{\alpha}_3\overline{M}\widetilde{\varepsilon}_{zz} + \overline{M}\widetilde{\zeta}\,, \tag{3.13}$$

with σ_{ij} is the stress tensor, ε_{ij} is the strain tensor, and M_{ij} is the stiffness tensor, p is the pore pressure, ζ is the variation of fluid content, α_1 and α_3 are the Biot's effective stress coefficients in the isotropic plane and in the transverse direction, respectively, and M is the inverse of storage coefficient under constant strains. Other governing relations include Darcy's law, strain-displacement relations, equilibrium equations, and continuity equation as listed below.

Darcy's law,

$$\widetilde{q}_r = -\frac{k_1}{\mu}\frac{\partial\widetilde{p}}{\partial r}\,, \tag{3.14a}$$

$$\widetilde{q}_\theta = -\frac{k_1}{\mu}\frac{1}{r}\frac{\partial\widetilde{p}}{\partial\theta}\,, \tag{3.14b}$$

$$\widetilde{q}_z = -\frac{k_3}{\mu}\frac{\partial\widetilde{p}}{\partial z}\,, \tag{3.14c}$$

with k_1 and k_3 are the permeability in the isotropic plane and in the transverse direction; and μ denotes pore fluid viscosity.

Strain-displacement relations,

$$\widetilde{\varepsilon}_{rr} = \frac{\partial \widetilde{u}_r}{\partial r}, \tag{3.15a}$$

$$\widetilde{\varepsilon}_{\theta\theta} = \frac{\widetilde{u}_r}{r} + \frac{1}{r}\frac{\partial \widetilde{u}_\theta}{\partial \theta}, \tag{3.15b}$$

$$\widetilde{\varepsilon}_{r\theta} = \frac{1}{2}\left(\frac{1}{r}\frac{\partial \widetilde{u}_r}{\partial \theta} + \frac{\partial \widetilde{u}_\theta}{\partial r} - \frac{\widetilde{u}_\theta}{r}\right), \tag{3.15c}$$

$$\widetilde{\varepsilon}_{zz} = \frac{\partial \widetilde{u}_z}{\partial z}. \tag{3.15d}$$

Equilibrium equations,

$$\frac{\partial \widetilde{\sigma}_{rr}}{\partial r} + \frac{1}{r}\frac{\partial \widetilde{\sigma}_{\theta r}}{\partial \theta} + \frac{\widetilde{\sigma}_{rr} - \widetilde{\sigma}_{\theta\theta}}{r} = 0, \tag{3.16a}$$

$$\frac{\partial \widetilde{\sigma}_{r\theta}}{\partial r} + \frac{1}{r}\frac{\partial \widetilde{\sigma}_{\theta\theta}}{\partial \theta} + 2\frac{\widetilde{\sigma}_{r\theta}}{r} = 0, \tag{3.16b}$$

$$\frac{\partial \widetilde{\sigma}_{zz}}{\partial z}. \tag{3.16c}$$

Continuity equation,

$$s\widetilde{\zeta} - \frac{k_1}{\mu}\left(\frac{\partial^2}{\partial r^2} + \frac{1}{r}\frac{\partial}{\partial r} + \frac{1}{r^2}\frac{\partial^2}{\partial \theta^2}\right)\widetilde{p} = 0. \tag{3.17}$$

3.3.3 K_0 Test or Confined Compression Test

The experimental setup becomes a one-dimensional problem in the axial direction. In particular,

$$u_r = u_\theta = 0, \varepsilon_{rr} = \varepsilon_{\theta\theta} = 0, q_r = q_\theta = 0, \tag{3.18}$$

and all non-trivial variables are dependent on z and t only. Substitution of the constitutive relations and the equilibrium equation in axial direction transforms the diffusion equation into:

$$s\widetilde{\zeta} - c_3 \frac{\partial^2 \widetilde{\zeta}}{\partial z^2} = 0, c_3 = \frac{k_3}{\mu} \frac{\overline{M}_{33} \overline{M}}{\overline{M}_{33}^u}, \tag{3.19}$$

which admits the following solution:

$$\widetilde{\zeta} = C_1 \exp(z\sqrt{s/c_3}) + C_2 \exp(-z\sqrt{s/c_3}). \tag{3.20}$$

Using the boundary conditions, it can be shown that for load-controlled testing condition:

$$C_1 = C_2 = -\frac{\overline{\alpha}_3}{2\overline{M}_{33}} \frac{\widetilde{S}_o}{\cosh(H\sqrt{s/c_3})}. \tag{3.21}$$

The variation of fluid content therefore takes the form:

$$\widetilde{\zeta} = -\frac{\overline{\alpha}_3}{\overline{M}_{33}} \widetilde{S}_o \frac{\cosh(z\sqrt{s/c_3})}{\cosh(H\sqrt{s/c_3})}. \tag{3.22}$$

Other variables can then be found easily to be as follows:

$$\widetilde{p} = \frac{\overline{\alpha}_3 \overline{M}}{\overline{M}_{33}^u} \widetilde{S}_o \left[1 - \frac{\cosh(z\sqrt{s/c_3})}{\cosh(H\sqrt{s/c_3})}\right], \tag{3.23}$$

$$\widetilde{q}_z = \frac{k_3}{\mu} \frac{\overline{\alpha}_3 \overline{M}}{\overline{M}_{33}^u} \sqrt{\frac{s}{c_3}} \widetilde{S}_o \frac{\sinh(z\sqrt{s/c_3})}{\cosh(H\sqrt{s/c_3})}, \tag{3.24}$$

$$\widetilde{\varepsilon}_{zz} = \frac{1}{\overline{M}_{33}^u} \widetilde{S}_o \left[1 + \frac{\overline{\alpha}_3^2 \overline{M}}{\overline{M}_{33}} \frac{\cosh(z\sqrt{s/c_3})}{\cosh(H\sqrt{s/c_3})}\right], \tag{3.25}$$

$$\widetilde{\sigma}_{rr} = \widetilde{\sigma}_{\theta\theta} = \frac{1}{\overline{M}_{33}^u} \widetilde{S}_o \left[\overline{M}_{13}^u - \frac{\overline{\alpha}_3 \overline{\lambda}_{331} \overline{M}}{\overline{M}_{33}} \frac{\cosh(z\sqrt{s/c_3})}{\cosh(H\sqrt{s/c_3})}\right]. \tag{3.26}$$

For stroke-controlled testing configuration, the average axial stress S_o can be calculated from the displacement u_z using the following relation:

$$\widetilde{u}_z = \frac{\widetilde{S}_o}{\overline{M}_{33}^u} \left[H + \frac{\overline{\alpha}_3^2 \overline{M}}{\overline{M}_{33}} \frac{\tanh(H\sqrt{s/c_3})}{\sqrt{s/c_3}}\right]. \tag{3.27}$$

3.3.4 Unconfined Compression Test and Triaxial Tests

Substitution of the constitutive relations into the equilibrium equation in radial direction yields the following Navier-type equation:

$$\frac{\partial\left(\widetilde{\varepsilon}_{rr}+\widetilde{\varepsilon}_{\theta\theta}\right)}{\partial r}=-\frac{\overline{\alpha}_1\overline{M}}{\overline{M}_{11}^{u}}\frac{\partial\widetilde{\zeta}}{\partial r}. \tag{3.28}$$

This equation and the constitutive relations transform the diffusion equation into:

$$s\widetilde{\zeta}-c_1\left(\frac{\partial^2}{\partial r^2}+\frac{1}{r}\frac{\partial}{\partial r}\right)\widetilde{\zeta}=0,\ c_1=\frac{k_1}{\mu}\frac{\overline{M}_{11}\overline{M}}{\overline{M}_{11}^{u}}, \tag{3.29}$$

of which the analytical solution is as follows:

$$\widetilde{\zeta}=\frac{\overline{M}_{11}^{u}}{\overline{M}}C_1I_0\left(\xi\right), \tag{3.30}$$

with $\xi=r\sqrt{s/c_1}$ and I_n is the modified Bessel function of the first kind of order n. Substituting this solution into the Navier-type equation and integrating with respect to r yields the expression for the radial displacement,

$$\widetilde{u}_r=-\overline{\alpha}_1C_1r\frac{I_1\left(\xi\right)}{\xi}+\frac{C_2r}{2}. \tag{3.31}$$

The Laplace-domain solutions for all stresses, strains, pore fluid pressure, and flux can then be obtained using equations (3.10) to (3.15). For stroke-control testing condition, $\varepsilon_{zz}=\varepsilon_{zz}(t)$, the parameters take the form:

$$C_1=\frac{1}{D_\varepsilon}\left[\left(\overline{M}_{11}^{u}+\overline{M}_{12}^{u}\right)\widetilde{p}_o-2\overline{\alpha}_1\overline{M}\widetilde{P}_o-\left(\overline{\lambda}_{113}+\overline{\lambda}_{123}\right)\overline{M}\widetilde{\varepsilon}_{zz}\right], \tag{3.32}$$

$$C_2=\frac{1}{D_\varepsilon}\left\{\begin{array}{l}-4\overline{G}\,\overline{\alpha}_1\dfrac{I_1\left(\beta\right)}{\beta}\widetilde{p}_o+2\overline{M}_{11}I_0\left(\beta\right)\widetilde{P}_o\\+2\left[2\overline{G}\,\overline{\alpha}_1\overline{\alpha}_3\overline{M}\dfrac{I_1\left(\beta\right)}{\beta}-\overline{M}_{11}\overline{M}_{13}^{u}I_0\left(\beta\right)\right]\widetilde{\varepsilon}_{zz}\end{array}\right\}, \tag{3.33}$$

with new coefficients as follows:

$$\overline{G} = (\overline{M}_{11} - \overline{M}_{12})/2\,, \tag{3.34}$$

$$D_{\varepsilon} = \overline{M}_{11}\left(\overline{M}^{u}_{11} + \overline{M}^{u}_{12}\right)I_0(\beta) - 4\overline{G}\,\overline{\alpha}_1^2\,\overline{M}\,\frac{I_1(\beta)}{\beta}\,, \tag{3.35}$$

and $\beta = R\sqrt{s/c_1}$. For load-control testing condition, $F = F(t)$, using equation (3.3), the resultant axial strain can be obtained as follows:

$$\widetilde{\varepsilon}_{zz} = \frac{1}{D_{\sigma}}\left\{\begin{aligned} &2\left[\overline{\lambda}_{113}\left(\overline{M}^{u}_{11} + \overline{M}^{u}_{12}\right) - 2\overline{G}\,\overline{\alpha}_1\overline{M}^{u}_{13}\right]\frac{I_1(\beta)}{\beta}\,\widetilde{p}_o \\ &+2\left[\overline{M}_{11}\overline{M}^{u}_{13}I_0(\beta) - 2\overline{\alpha}_1\overline{\lambda}_{113}\overline{M}\,\frac{I_1(\beta)}{\beta}\right]\widetilde{P}_o \\ &+\left[4\overline{G}\,\overline{\alpha}_1^2\overline{M}\,\frac{I_1(\beta)}{\beta} - \overline{M}_{11}\left(\overline{M}^{u}_{11} + \overline{M}^{u}_{12}\right)I_0(\beta)\right]\widetilde{S}_o \end{aligned}\right\}, \tag{3.36}$$

with

$$\begin{aligned} D_{\sigma} = {} & \overline{M}_{11}\left[2\left(\overline{M}^{u}_{13}\right)^2 - \overline{M}^{u}_{33}\left(\overline{M}^{u}_{11} + \overline{M}^{u}_{12}\right)\right]I_0(\beta) \\ & + 2\overline{M}\left[\left(\overline{\lambda}_{113} + \overline{\lambda}_{123}\right)\overline{\lambda}_{113} + 2\overline{G}\,\overline{\alpha}_1\overline{\lambda}_{331}\right]\frac{I_1(\beta)}{\beta}\,, \end{aligned} \tag{3.37}$$

and the average axial stress S_o is defined as follows:

$$S_o(t) = \frac{F(t)}{\pi R^2}\,. \tag{3.38}$$

3.3.5 Strain Recovery Method

The overall unloading of the core can be decomposed into two parts: axisymmetric unloading and deviatoric unloading. The deviatoric unloading is controlled by the following boundary conditions:

$$\sigma_{rr}\big|_{r=R} = -\frac{S_{Hmax} - S_{hmin}}{2}\cos 2\left(\theta - \theta_{S_H}\right)H(t)\,,$$

$$\sigma_{r\theta}\big|_{r=R} = \frac{S_{Hmax} - S_{hmin}}{2} \sin 2\left(\theta - \theta_{S_H}\right) H(t)\,, \tag{3.39}$$

with $H(t)$ is the Heaviside unit step function. As shown by Abousleiman et al. (1996), the relaxation displacements take the form:

$$\widetilde{u}_r\big|_{r=R} = -\frac{S_{Hmax} - S_{hmin}}{4s\overline{G}} r\cos 2\left(\theta - \theta_{S_H}\right),\ \widetilde{u}_\theta\big|_{r=R} = \frac{S_{Hmax} - S_{hmin}}{4s\overline{G}} \sin 2\left(\theta - \theta_{S_H}\right). \tag{3.40}$$

The axisymmetric unloading is composed of the remaining of the stress and pressure boundary conditions, with the following general form:

$$\sigma_{rr}\big|_{r=R} = P_o(t),\ p\big|_{r=R} = p_o(t),\ \sigma_{zz}\big|_{r=R} = S_o(t),\ \sigma_{r\theta}\big|_{r=R} = 0\,. \tag{3.41}$$

For this mode of unloading, it can be shown that the diffusion equation takes the form:

$$s\widetilde{\zeta} - c_1\left(\frac{\partial^2}{\partial r^2} + \frac{1}{r}\frac{\partial}{\partial r}\right)\widetilde{\zeta} = 0\,, \tag{3.42}$$

of which the analytical solution is as follows:

$$\widetilde{\zeta} = \frac{\overline{M}_{11}^{u}}{\overline{M}} C_1 I_0\left(\xi\right), \tag{3.43}$$

with $\xi = r\sqrt{s/c_1}$ and I_n is the modified Bessel function of the first kind of order n. Substituting this solution into the Navier-type equation and integrating with respect to r yields the expression for the radial displacement,

$$\widetilde{u}_r = -\overline{\alpha}_1 C_1 r \frac{I_1\left(\xi\right)}{\xi} + \frac{C_2 r}{2}\,. \tag{3.44}$$

The parameters C_1 and C_2 can then be easily determined from the time-dependent boundary conditions $P_o(t)$, $p_o(t)$, and $S_o(t)$.

Eq. (3.40) shows that the deviatoric unloading behavior of the core only depends on the difference of horizontal in-situ stresses and on viscoelastic properties of the rock

matrix. In other words, pore fluid diffusion and coupled phenomena do not affect the deviatoric unloading behavior. This observation was recognized earlier by Warpinski and Teufel (1989). However, in practice, care must be taken to either measure the radial displacement only or separate the tangential displacement from the measured composite displacement.

The axisymmetric unloading behavior of the retrieved core, on the other hand, is extremely convoluted. It depends on the in-situ stress state, rock and fluid properties, as well as operational details such as core retrieval time and sample preparation time. The time for core retrieval affects the time-dependent stress and pore pressure unloading conditions while sample preparation time limits how much relaxation data can be recorded. These time durations, therefore, must be accounted for in the analysis.

3.4 Discussion on Analytical Solutions for Laboratory Testing

3.4.1 General Discussion

It is evident from the analytical expressions that the response of a transversely isotropic poroviscoelastic sample greatly depends on how it is tested, i.e., unconfined compression, triaxial configuration, or confined/oedometer testing. In particular, all four stiffness coefficients M_{11}, M_{12}, M_{13}, and M_{33} have significant influence on the behavior of a sample tested in unconfined compression or triaxial condition. On the other hand, M_{33} and to a lesser degree M_{13} take on a dominating role in determining the behavior of a sample tested in confined compression. Consequently, confined compression testing might be better for isolating and characterizing M_{13} and M_{33} than unconfined compression and triaxial tests. On the other hand, using the confined compression test alone could obviously result in misled conclusions about the anisotropic nature of the

tested material. A more in-depth example is given in the next section on biomechanics testing.

The presented formulation and solutions are general with regards to the form of the viscoelastic stiffness of the porous matrix. Spring-dashpot models such as the familiar Zener model (Carter and Booker, 1983; Leipzig and Athanasiou, 2005) can be easily employed. Alternatively, experimentally measured relaxation functions can also be used, provided their Laplace transforms exist.

From equations (3.19) and (3.29), it is clear that even when the intrinsic permeability is isotropic, i.e., $k_1 = k_3$, the diffusion coefficients in unconfined compression and triaxial setups, c_1, and confined compression or oedometer setup, c_3, could assume different values which reflect the anisotropy of the stiffness of the porous matrix. For fully coupled problems such as these, the diffusion of the pore fluid is governed not only by the intrinsic permeability of the matrix and the viscosity of the pore fluid but also by the anisotropic stiffness of the porous matrix. This issue must be taken into consideration when designing experimental protocols or analyzing laboratory data.

Finally, for the testing of poroviscoelastic transversely isotropic geo- and bio-materials using the investigated configurations, there are three different time scales involved that warrant careful consideration. The first time scale is dictated by the viscoelastic nature of the porous matrix. This time scale is an intrinsic material property and researchers have no control over it unless they actively modify the rock or the biological tissue. The second time scale involves the diffusion of pore fluid within the porous matrix, and is influenced by not only material properties but also sample

dimensions, giving researchers some command over it. The amount of control over this time scale is limited, however, in biomechanics mostly due to the physical limits in tissue size and thickness, and in geomechanics mostly due to the physical limits of the testing apparatus. The third and final time scale involves that of the deformation or load application and sample monitoring. Fortunately, this time scale can usually be controlled at the researcher's discretion. By understanding the intricate interplay between these three time scales, the laboratory tests can be designed to best suit the purpose of the experimentalist.

3.4.2 Numerical Examples of Biomechanics Testing

The response of an articular cartilage plug with dimensions of R = 2.5 mm and H = 1000 μm under two of the most popular setups in biomechanics research, i.e., unconfined compression and confined compression, is investigated to illustrate the applicability of the presented solutions. To demonstrate the viscoelastic effects of the matrix, all matrix drained moduli M_{ij}(t) are assumed to behave according to the Zener model. Initial stiffness coefficients are as follows: $M_{11}(0^+)$ = 0.560 MPa, $M_{12}(0^+)$ = 0.032 MPa, $M_{13}(0^+)$ = 0.029 MPa, and $M_{33}(0^+)$ = 1.200 MPa. All moduli are assumed to retain 2/3 of initial values at long time and to have the same characteristic relaxation time of 60 s. This assumption of a uniform relaxation function for all moduli serves to illustrate the material behavior more clearly and is not critical to the solutions. Different relaxation functions with diverging ratios of long-time value to initial value as well as different relaxation times can be used without any difficulty. Other material properties are time-independent as follows: porosity ϕ = 0.852, permeability in isotropic plane k_1 = 1.0×10^{-15} m^2, permeability in transverse direction k_3 = 1.0×10^{-15} m^2, fluid bulk modulus

K_f = 2.3 GPa, matrix grain bulk modulus K_s = 3.0 MPa, and fluid viscosity μ = 0.001 Pa·s. It is also worth noting that M_{11} and M_{33} are in fact the anisotropic aggregate moduli H_A in the isotropic plane and in the transverse direction within biomechanics context. Cyclic loading is of particular interest in the biomechanics testing; for this example, a stroke-controlled loading from 0-50 μm (0-5% apparent strain) with a frequency of 1 Hz is employed as shown in **Fig. 3.3**. The numerical results in this section were inverted from the analytical solutions using Durbin method with 800 terms (Cheng et al., 1994).

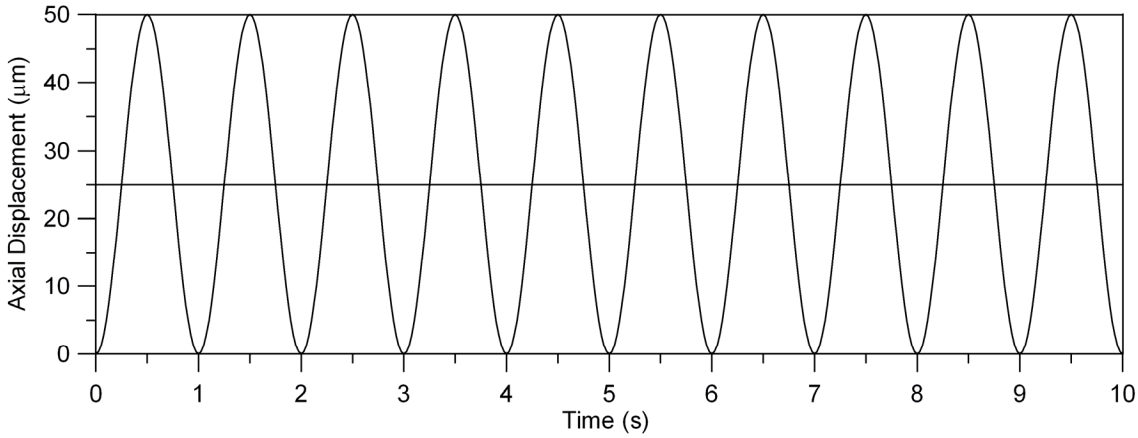

Fig. 3.3 – Applied cyclic axial deformation for both unconfined and confined compression tests.

Although the porous matrix of articular cartilage has long been recognized as a viscoelastic material, the tissue has been modeled as a poroelastic matter in some previous studies to simplify the analysis. The typical approach is to measure the long-time stiffness coefficients to determine the corresponding poroelastic parameters. Therefore, to further illustrate the poroviscoelastic behavior of the tissue, the response of a counterpart poroelastic sample is also investigated. Following the common analysis method, the stiffness coefficients are taken as $M_{ij\text{-elastic}} = M_{ij\text{-viscoelastic}}(\infty)$.

Furthermore, an isotropic poroviscoelastic sample is also analyzed to demonstrate the effects of material anisotropy. For illustration purposes, it is assumed that M_{33} and M_{13} are determined accurately; however, M_{11} and M_{12} are not evaluated but assumed to be the same as M_{33} and M_{13} based on the incorrect assumption of material isotropy.

Figs. 3.4–3.6 demonstrate the evolution of pore pressure and axial stress at the center and the lateral displacement of each side of the unconfined samples with time, respectively. Although the trends are similar, it is clear that under displacement-controlled loading, the poroelastic analysis could underestimate the magnitude of pore pressure and stress which is similar to results reported in earlier studies (Cohen et al., 1998; Bursać et al., 1999). It is also evident that the failure to account for material anisotropy could give rise to erroneous predictions of the articular cartilage response to external loading, even when poroviscoelastic modeling is used.

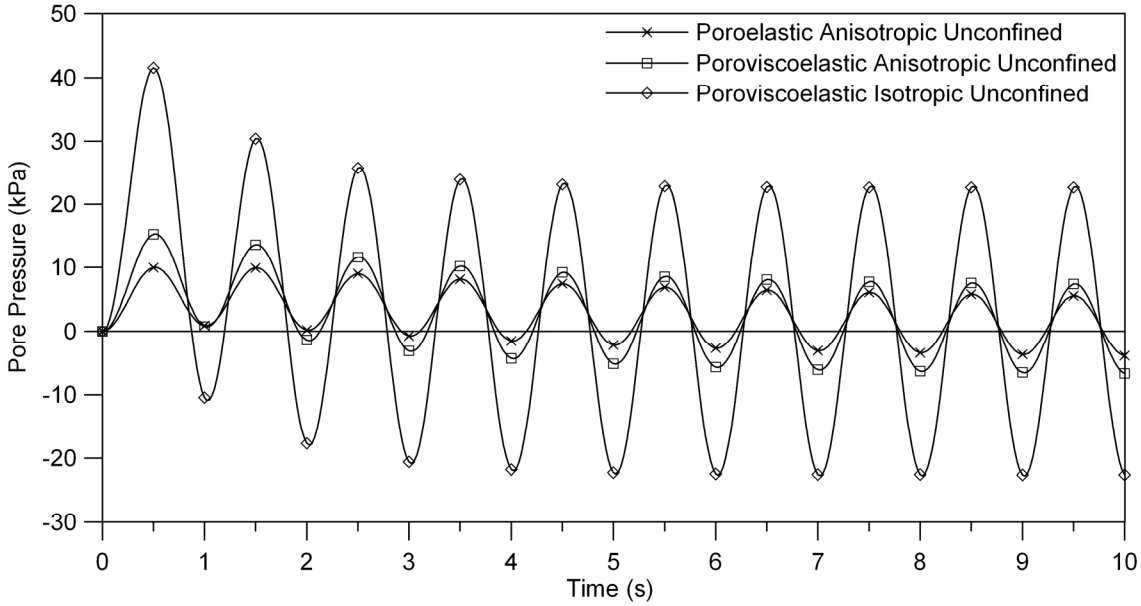

Fig. 3.4 – Pore pressure history at the center of the unconfined samples.

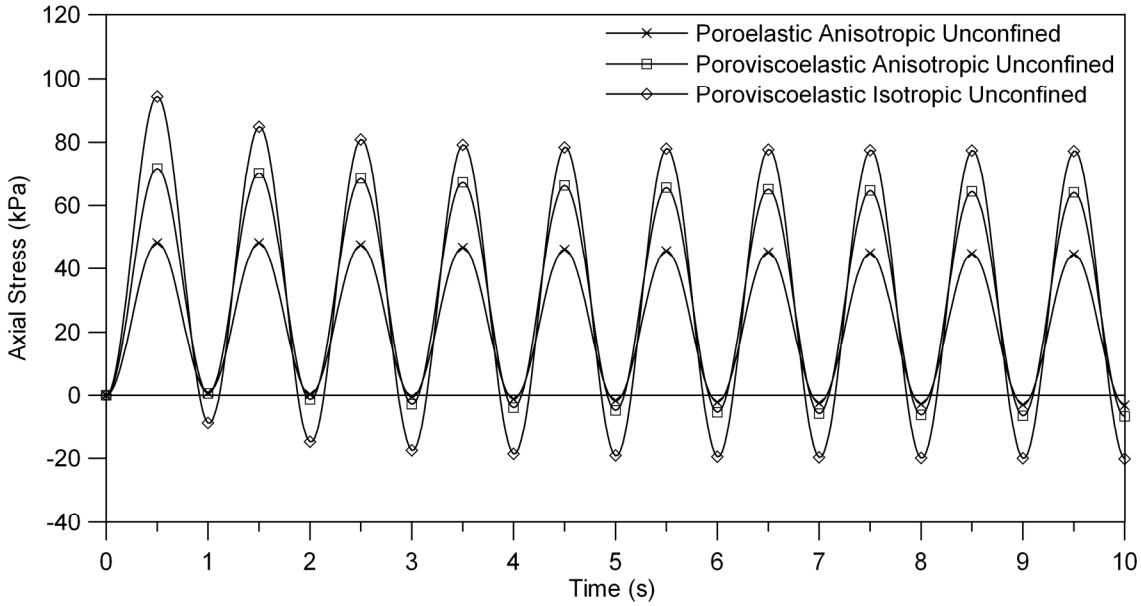

Fig. 3.5 – Evolution of axial stress at the center of the unconfined samples.

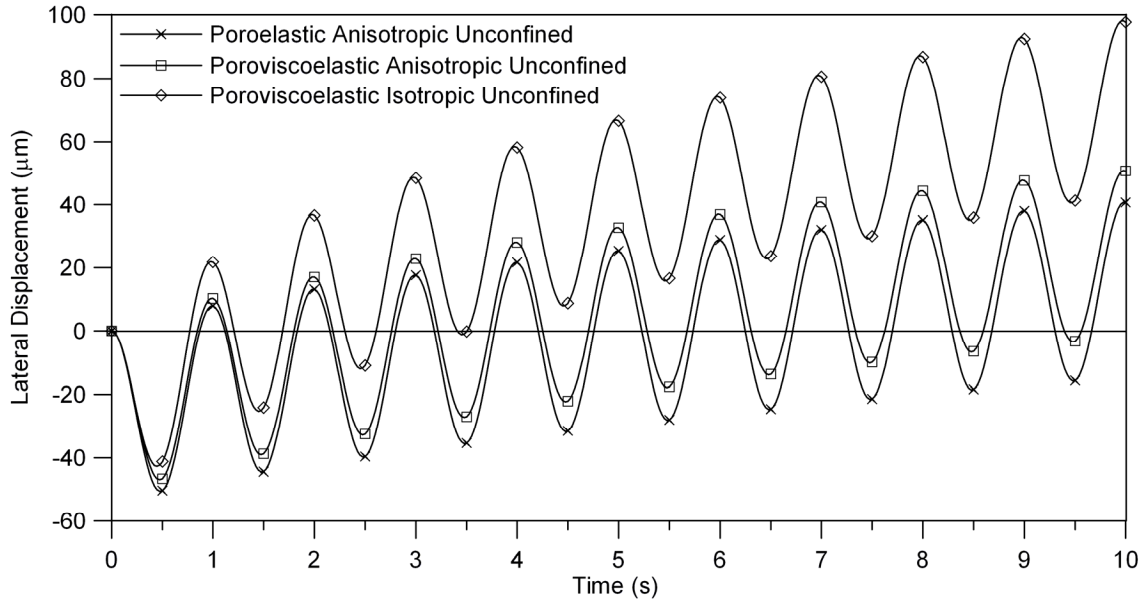

Fig. 3.6 – Evolution of lateral displacement of the side of the unconfined samples.

On the other hand, the differences in the confined compression tests are less pronounced, as shown in **Figs. 3.7–3.9**. Only minor difference exists between the poroviscoelastic anisotropic and the poroviscoelastic isotropic responses. The reason is that only two out of the four moduli, i.e., M_{33} and M_{13}, play a dominating role in determining the tissue behavior in this testing configuration, as explained in Section

3.4.1. Between the poroelastic results and the poroviscoelastic results, only the axial stress histories are significantly different while the evolution of the lateral stress and the pore pressure are almost the same for all three samples. Largely due to the small thickness of the tissue, i.e., H = 1000 μm, the diffusion time scale is relatively small. For example, the diffusion characteristic time for the poroelastic anisotropic sample is 1.06 s, comparable to the time scale of the 1-Hz applied loading while being much smaller than the viscoelastic relaxation characteristic time of 60 s. In other words, the pore pressure diffusion takes place fast enough compared to the applied loading as well as the viscoelastic relaxation of the porous tissue to render the difference between responses small. Under circumstances such as these, the use of the confined compression test alone could potentially mislead the experimentalist to conclude that the articular cartilage is poroelastic and/or isotropic. Therefore, other tests such as the unconfined compression test are recommended to supplement confined compression testing in material characterization for poroviscoelastic anisotropic biological tissues.

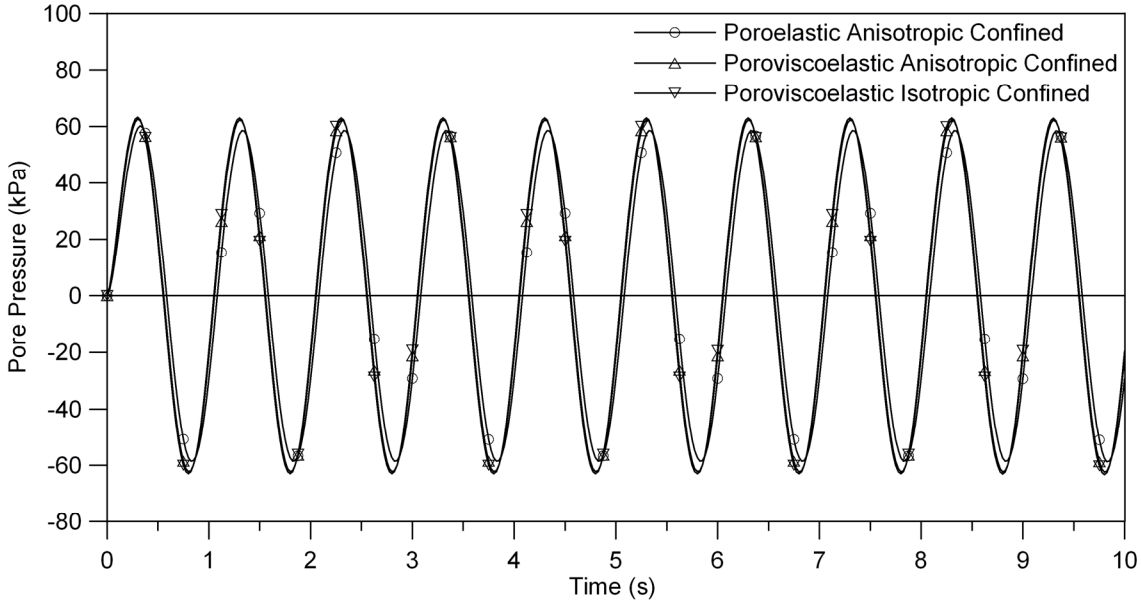

Fig. 3.7 – Pore pressure history at the bottom of the confined samples.

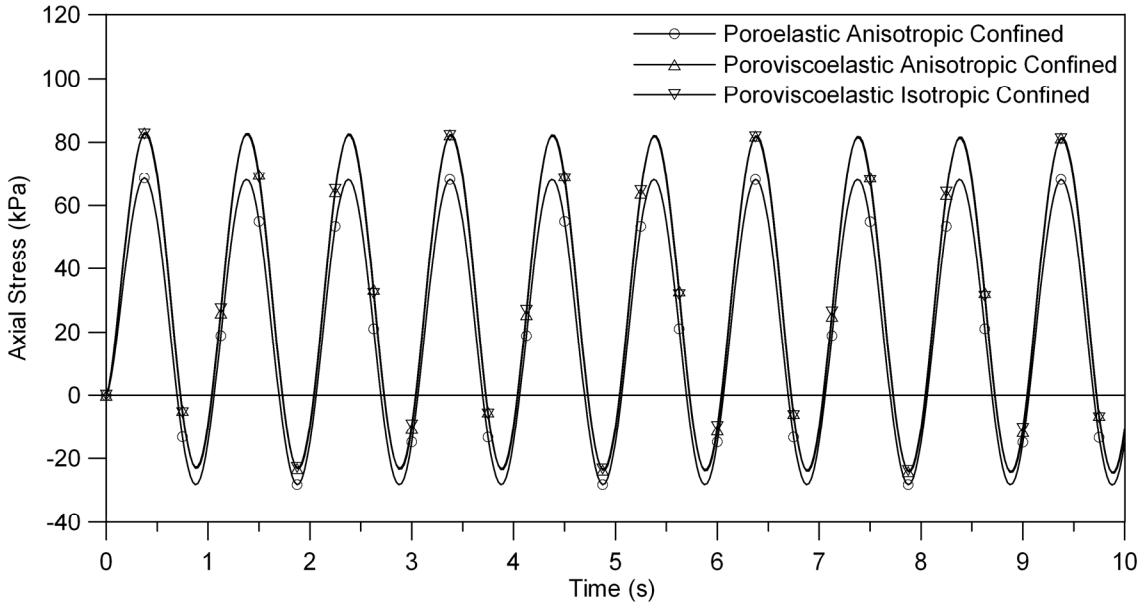

Fig. 3.8 – Evolution of axial stress at the center of the confined samples.

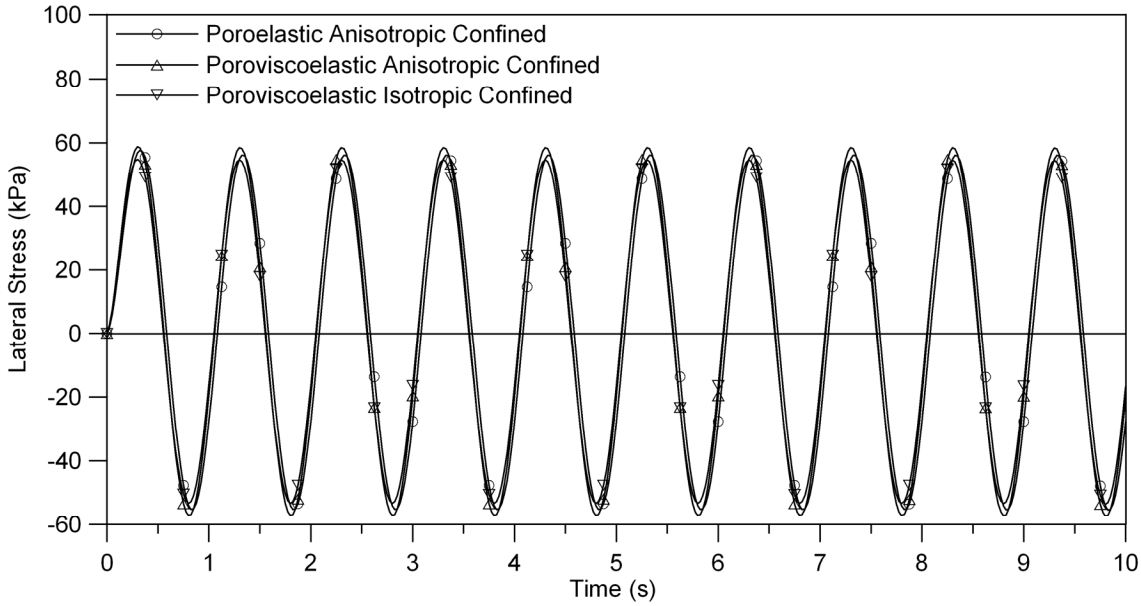

Fig. 3.9 – Evolution of lateral stress of the confined samples.

Similar phenomena have been observed in previous attempts to characterize articular cartilage using poroelasticity. Soulhat et al. (1999) reported that isotropic poroelastic modeling can give a reasonable description of the axial stress response in confined compression tests yet fails to describe the axial stress response in unconfined compression and transversely isotropic poroelastic modeling is required to improve the

match with experiments. Bursać et al. (1999) reported that even transversely isotropic poroelastic modeling cannot simultaneously match the axial and radial responses of confined and unconfined compression tests for calf articular cartilage. The numerical examples in this section illustrate that the failure to account for either anisotropy or viscoelasticity of the articular cartilage matrix could result in flawed predictions of the tissue behavior under general external loading.

3.4.3 Numerical Examples of Geomechanics Testing

In this section, the response of an oil shale rock sample with dimensions of R = 5 cm and H = 20 cm under jacketed triaxial setup is investigated. It has been reported that the characteristic time of creep for many rocks including shale, siltstone, and sandstone, falls in the range of 10 to 15 hours (Warpinski and Teufel, 1989). Therefore, in this example, all matrix drained moduli $M_{ij}(t)$ are assumed to behave according to the Zener model with the same characteristic creep time of 10 hours. Initial stiffness coefficients are assumed as follows: $M_{11}(0^+)$ = 11.93 GPa, $M_{12}(0^+)$ = 4.93 GPa, $M_{13}(0^+)$ = 3.37 GPa, and $M_{33}(0^+)$ = 5.90 GPa. All moduli are assumed to retain 50% of initial values at long time. Other material properties are time-independent as follows: porosity ϕ = 0.08, permeability $k_1 = k_3$ = 50 nD, fluid bulk modulus K_f = 300 MPa, matrix grain bulk modulus K_s = 40 GPa, and fluid viscosity μ = 0.010 Pa·s. The numerical results presented in this section were inverted to time domain with Stehfest algorithm using 10 terms (Cheng et al., 1994).

A counterpart poroelastic sample is also examined to demonstrate the poroviscoelastic effects. Since the characteristic time of viscoelasticity of the rock matrix is substantially longer than most standard tests, material characterization using

conventional techniques would likely produce the short-time poromechanics parameters. Therefore, for the poroelastic sample, the stiffness coefficients are taken as $M_{ij\text{-elastic}} = M_{ij\text{-viscoelastic}}(0^+)$.

Finally, an isotropic poroviscoelastic sample is also studied to demonstrate the effects of material anisotropy. For illustration purposes, it is assumed that M_{33} and M_{13} are determined accurately; however, M_{11} and M_{12} are not assessed but assumed to be the same as M_{33} and M_{13} based on the incorrect assumption of material isotropy.

A drained triaxial test in geomechanics typically consists of a relatively rapid confinement to the desired confining pressure, a waiting period to ensure that the generated pore pressure has enough time to dissipate, and finally a linear-ramp axial displacement loading to the desired strain or failure. In this example, the samples will be confined rapidly to a confining pressure of 10 MPa. The linear ramp axial loading will be at the rate of 2% strain in 10 hours.

Figs. 3.10 to 3.12 show the response of the poroelastic anisotropic, poroviscoelastic anisotropic, and poroviscoelastic isotropic samples after the rapid confinement to 10 MPa, i.e., $P_o(t) = S_o(t) = 10$ MPa $\times H(t)$ and $p_o(t) = 0$. The actual buildup time is typically one minute or less, much shorter than the viscoelastic characteristic creep time of 10 hours. It is also much shorter than the diffusion characteristic times, for example 48.4 hours for the poroelastic sample. Therefore, the confining pressure buildup has been idealized as a Heaviside step function without loss of generality.

Fig. 3.10 shows the pore pressure generation at the center of the samples as a function of time. It is evident that the poroelastic analysis would severely underestimate how long the generated pore pressure can sustain inside the poroviscoelastic sample,

and therefore would estimate an inadequate waiting period before the application of axial loading.

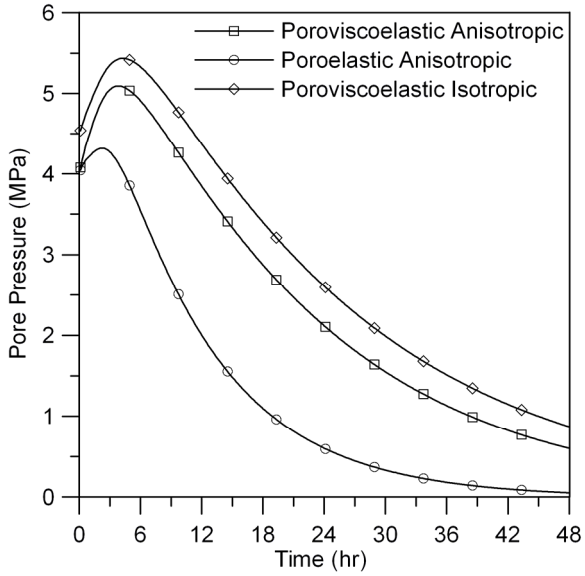

Fig. 3.10 – Evolution of pore pressure at the center of samples after sudden confinement.

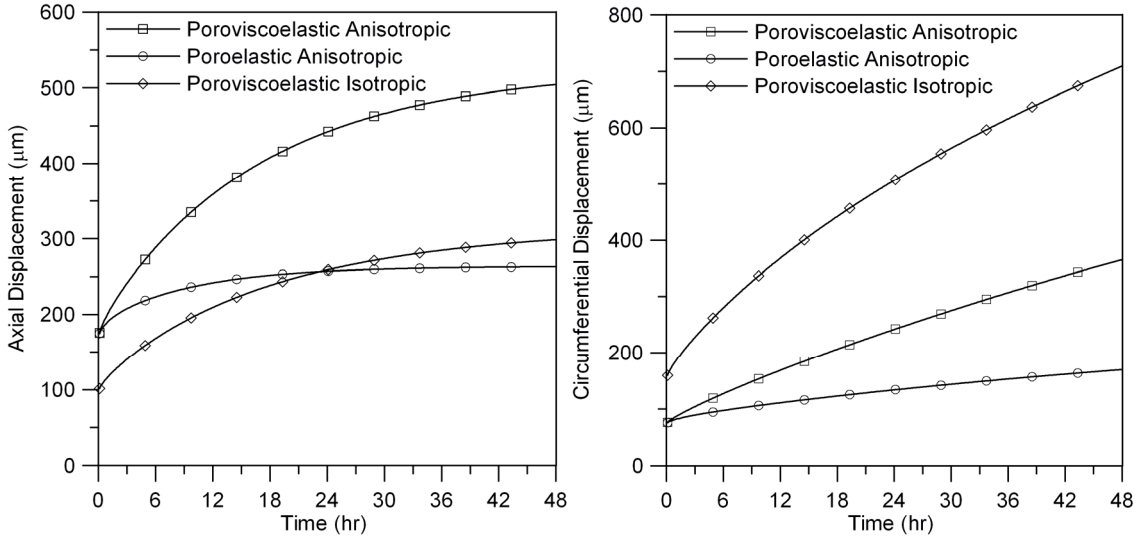

Fig. 3.11 – Evolution of axial and circumferential displacements after sudden confinement.

Fig. 3.11 presents the history of the axial and circumferential displacement after the rapid confinement, respectively, which can be readily measured in the experimental

setting. These displacements can clearly help differentiate between poroelastic and poroviscoelastic behavior, as well as anisotropic and isotropic rock properties.

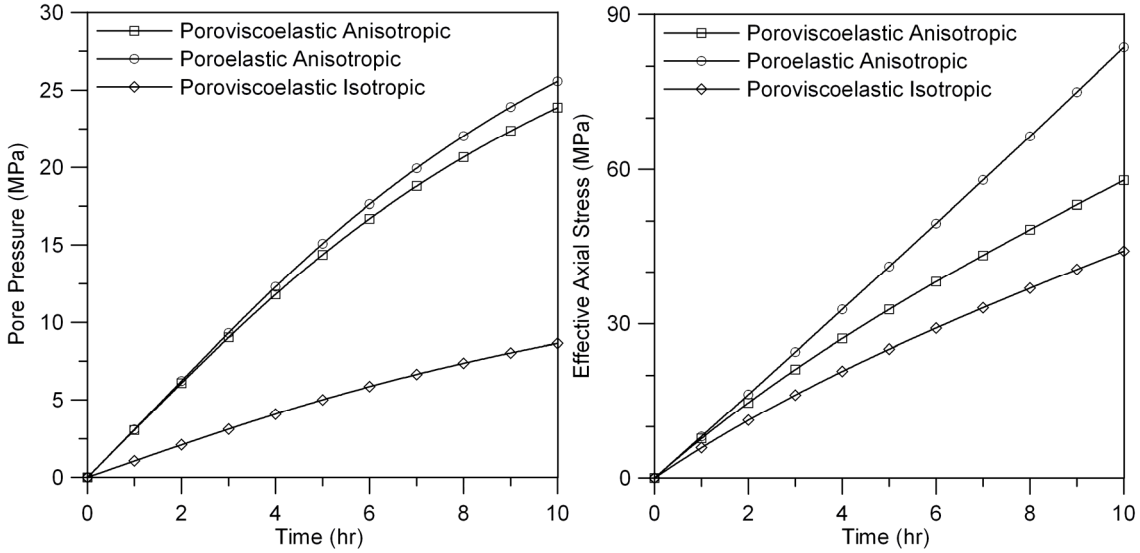

Fig. 3.12 – Evolution of pore pressure and effective axial stress at the center of samples during linear ramp axial loading.

Fig. 3.12 shows the pore pressure and effective axial stress at the center of the same three samples during the linear ramp axial displacement loading. The rate of loading is relatively slow, i.e., 2% apparent strain in 10 hours, to accommodate the long viscoelastic characteristic time as well as the long diffusion characteristic time. While the poroelastic analysis can relatively follow the poroviscoelastic trend in pore pressure prediction, it overestimates the effective stress at the center of the poroviscoelastic sample. On the other hand, **Fig. 3.12** clearly shows that the failure to account for material anisotropy could result in seriously flawed predictions or analysis of rock behavior even under well-controlled laboratory testing conditions.

3.5 Numerical Examples and Discussion on Strain Recovery Method

In this section, the response of a core sample with diameter of 15.24 cm (6 in) retrieved from a depth of 1000 m is investigated. The in-situ stress state is summarized below:

S_V = 2.31 SG, S_{Hmax} = 2.07 SG, S_{hmin} = 1.84 SG, p_0 = 1.0 SG, $\theta_{S_H} = 0$.

It has been reported that the characteristic time of creep for many rocks including shales, siltstones, and sandstones, falls in the range of 10 to 15 hours (Warpinski and Teufel, 1989). Therefore, in this example, all matrix drained moduli $M_{ij}(t)$ are assumed to behave according to the Zener model with the same characteristic creep time of 10 hours. Other models for the viscoelasticity of the rock matrix or experimentally measured relaxation/creep functions can be easily employed in the same manner. Initial Young's modulus perpendicular to bedding, $E_3(0^+)$, is assumed to be 5 GPa. The Poisson's ratios are assumed to be constant, $\nu_1 = \nu_3 = 0.3$. All moduli are assumed to retain 50% of initial values at long time. The Young's modulus in the direction parallel to bedding is assumed to be $E_1 = n_E E_3$. The anisotropy ratio n_E is typically from 1 to 2. Three different values of nE of 1.0, 1.5, and 2.0 will therefore be analyzed herein. Other material properties are as follows: porosity $\phi = 0.10$, permeability k_1 = 5 nD, fluid bulk modulus K_f = 2.3 GPa, matrix grain bulk modulus K_s = 42 GPa, and fluid viscosity μ = 1 cP.

The simplified analyses using viscoelasticity commonly used in the petroleum industry are also included to investigate their performance on these low-permeability shales. In these analyses, the pore pressure distribution is assumed to be uniform

throughout the core and equal the pore pressure on the core surfaces (Blanton and Teufel, 1986).

Figs 3.13 to 3.18 show the full relaxation evolution of the cores from the end of coring and the measured relaxation data during the actual test side by side with the corresponding simplified viscoelastic modeling. Although the viscoelastic modeling results roughly follow the trends of the poroviscoelastic rock samples, they cannot capture the actual relaxation behavior. It is also evident that the anisotropy of the formation significantly affects both the overall relaxation evolution and the recorded relaxation.

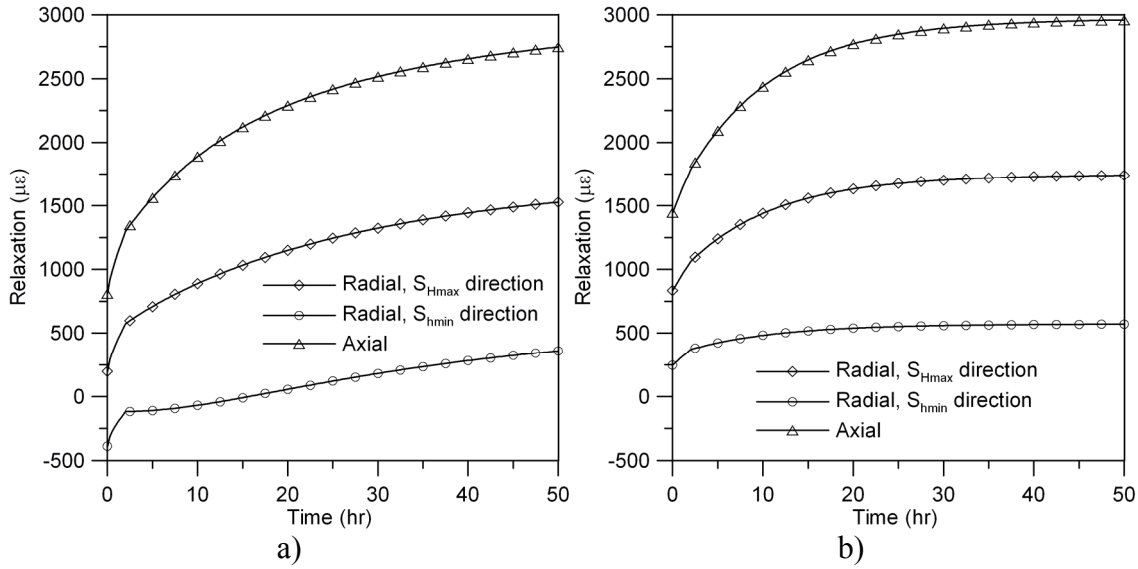

Fig. 3.13 – Poroviscoelastic relaxation evolution from the end of coring for $E_1 = E_3$, (a) and simplified viscoelastic modeling, (b).

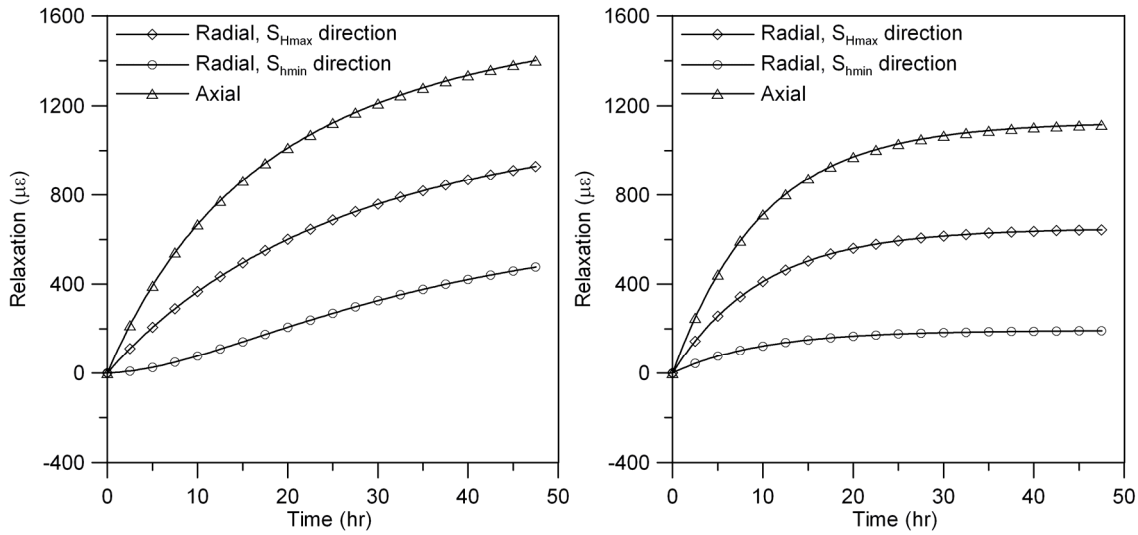

Fig. 3.14 – Measured poroviscoelastic relaxation data for $E_1 = E_3$, (a) and simplified viscoelastic modeling, (b).

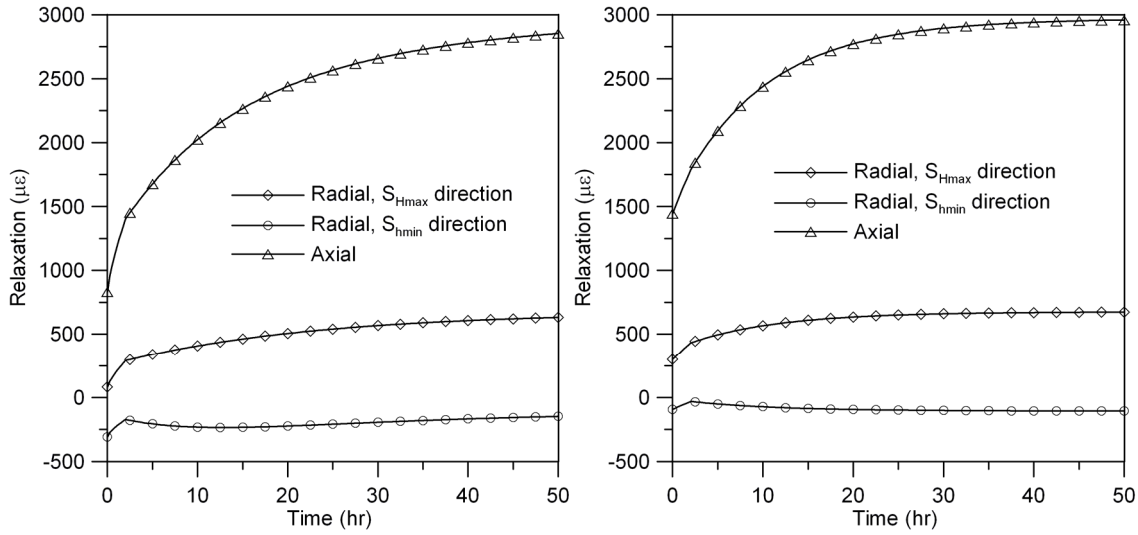

Fig. 3.15 – Poroviscoelastic relaxation evolution from the end of coring for $E_1 = 1.5E_3$, (a) and simplified viscoelastic modeling, (b).

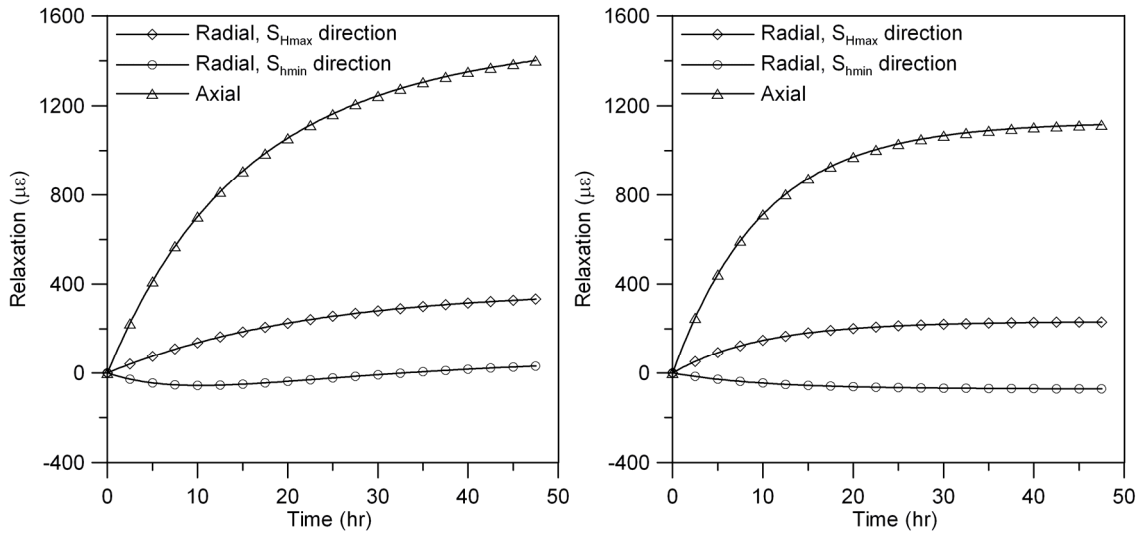

Fig. 3.16 – Measured poroviscoelastic relaxation data for $E_1 = 1.5E_3$, (a) and simplified viscoelastic modeling, (b).

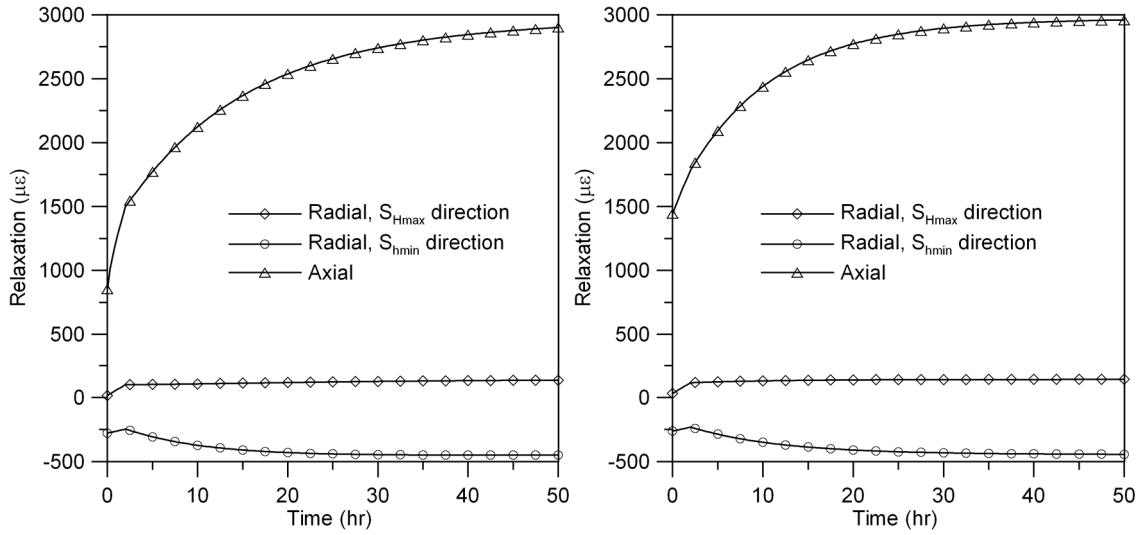

Fig. 3.17 – Poroviscoelastic relaxation evolution from the end of coring for $E_1 = 2E_3$, (a) and simplified viscoelastic modeling, (b).

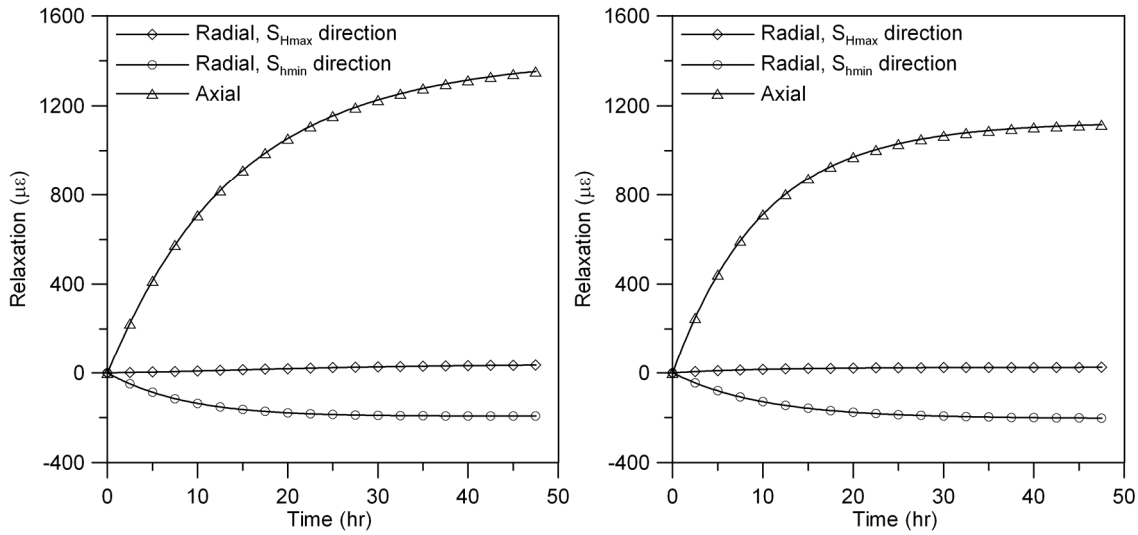

Fig. 3.18 – Measured poroviscoelastic relaxation data for $E_1 = 2E_3$, (a) and simplified viscoelastic modeling, (b).

3.6 Summary

The analytical solution for the poroviscoelastic transversely isotropic cylinder problem has been derived, accommodating a number of laboratory and field testing conditions. For the testing of poroviscoelastic anisotropic geo- and bio-materials, there are three different time scales involved that demand careful consideration. The first time scale comes from the viscoelastic nature of the porous matrix and is an intrinsic material property. The second time scale involves the diffusion of pore fluid within the porous matrix, and is influenced by material properties as well as sample dimensions. The final time scale belongs to load application and sample monitoring. Understanding the complex interplay between these three time scales is crucial for the design of laboratory tests on poroviscoelastic materials. Furthermore, even when the intrinsic permeability is isotropic, the diffusion coefficients in unconfined compression and triaxial setup could be very different from the diffusion coefficients in confined compression and oedometer configuration due to the anisotropy of the matrix stiffness. This issue must be taken into

consideration when designing experimental protocols or analyzing and interpreting laboratory data.

Inspection of the analytical expressions shows that the response of a transversely isotropic poroviscoelastic sample would significantly depend on which testing configuration is chosen. In particular, all four stiffness coefficients M_{11}, M_{12}, M_{13}, and M_{33} have significant influence on the behavior of a sample tested under unconfined compression and triaxial condition while only M_{33} and M_{13} dominate the behavior of the same sample tested in confined compression and oedometer condition. As a consequence, the use of the confined compression or oedometer test alone could potentially mislead the researcher that the anisotropic material is isotropic. Furthermore, in some cases the researcher can also be deceived into believing that the material is poroelastic instead of poroviscoelastic as demonstrated in the numerical example of articular cartilage confined compression testing with cyclic loading. In short, unconfined compression or triaxial tests would probably yield more accurate material characterization than confined compression or oedometer testing for poroviscoelastic anisotropic geo-materials and biological tissues.

For poroviscoelastic geo-materials tested under a drained triaxial setup with confinement followed by linear ramp axial loading, the sample response should be closely monitored during the waiting period after confinement in addition to during the axial loading, as these data can help characterize both the poroviscoelastic and the anisotropic nature of the rocks. The failure to account for either the viscoelasticity or the anisotropy of the rock matrix can detrimentally affect the estimation of effective stress for poroviscoelastic rocks subjected to external loading.

In this chapter, an analytical simulation of the poroviscoelastic transversely isotropic relaxation of a drill core from a vertical well, from the time it is cored, during retrieval, and during sample monitoring in laboratory conditions, using realistic time-dependent stress and pressure unloading conditions, has also been presented. Deviatoric unloading behavior of the core has been shown to depend only on the difference of horizontal in-situ stresses and on viscoelastic properties of the rock matrix. The axisymmetric unloading behavior, on the other hand, is extremely convoluted. It depends on the in-situ stress state, rock and fluid properties, as well as operational details such as core retrieval time and sample preparation time. Through the numerical examples demonstrated herein, it is clear that both the poroviscoelasticity and anisotropy of the rock formation must be accounted for in order to realistically capture the actual core relaxation.

In conclusion, the presented analytical solutions could serve as benchmarks for validating numerical schemes and simulations or assist directly in calibrating and interpreting test results on poroviscoelastic anisotropic geo- and bio-materials.

Chapter 4: Weakly Orthotropic Cylinders

4.1 Introduction

This chapter presents the analytical solutions for the time-dependent evolution of pore pressure, axial, radial, and tangential stresses, as well as axial and radial displacements, of a poroelastic or poroviscoelastic cylindrical sample with cylindrical weak orthotropy under triaxial or unconfined compression testing conditions. These solutions are of particular importance for cylindrically-reinforced low permeability clays with significant viscoelastic behavior. Potential applications of these materials might include nuclear waste storage, chemical waste storage, and viscoelastic settlement estimation.

4.2 Problem Description

A time-dependent axial force $F(t)$ is applied through the rigid frictionless end caps as shown in **Fig. 4.1**. Time-dependent confining pressure $P_o(t)$ and pore pressure $p_o(t)$ can also be applied to the lateral surface. The tested material has weak cylindrical orthotropy ($|M_{11} - M_{22}| << M_{11}, M_{22}$ and $|M_{13} - M_{23}| << M_{13}, M_{23}$), with the axis of material symmetry coinciding with the axis of geometrical symmetry. The analytical solutions derived herein are also applicable to more familiar subsets of weak cylindrical orthotropy such as transverse isotropy and isotropy.

The general boundary conditions at $r = R$ are as follows:

$$\sigma_{rr} = P_o(t),\ p = p_o(t),\ \sigma_{r\theta} = \sigma_{rz} = 0\,. \tag{4.1}$$

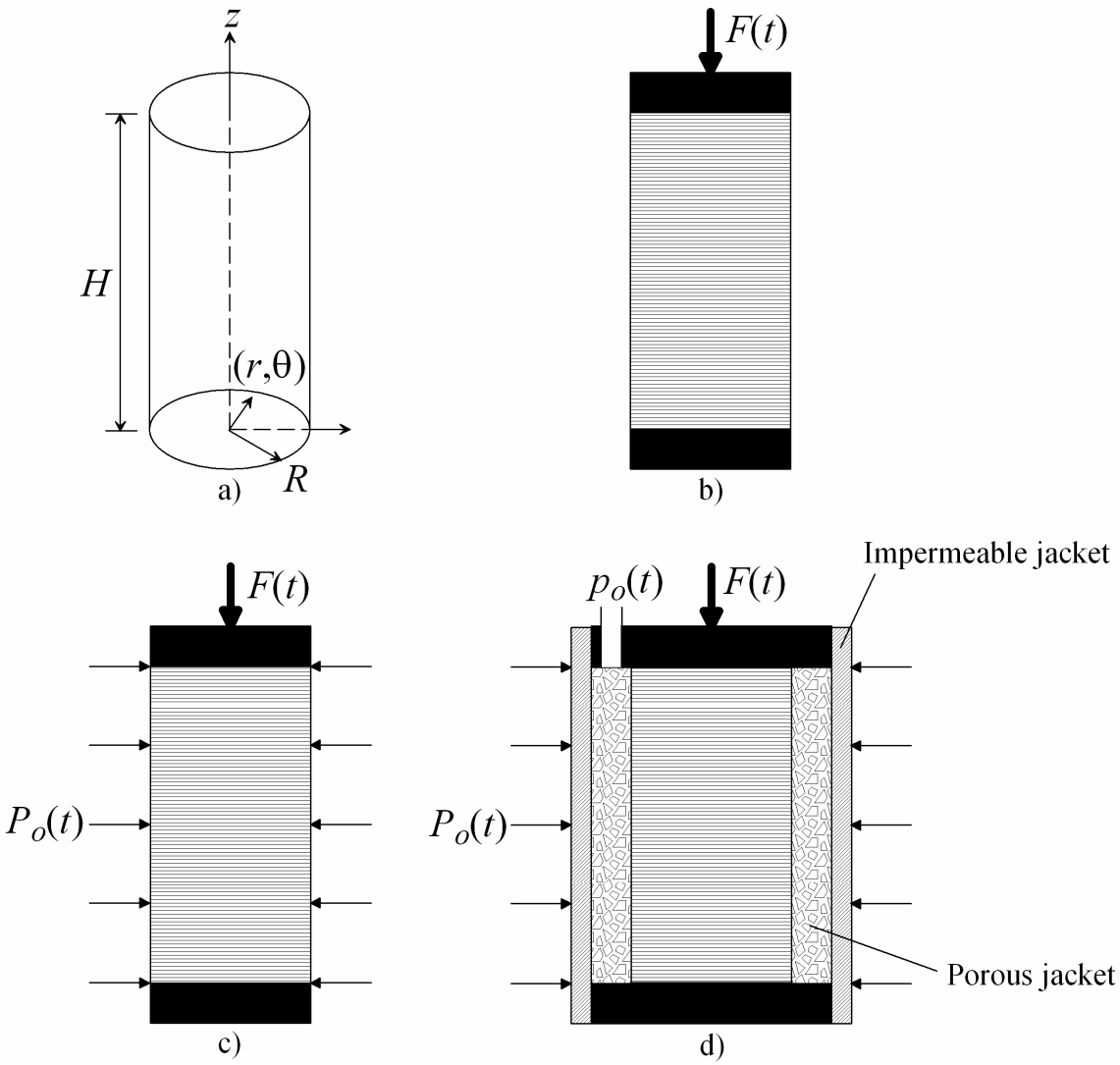

Fig. 4.1 – Compression testing of anisotropic cylindrical sample, a) sample dimension and attached polar coordinate system, b) unconfined compression test, c) unjacketed triaxial test, d) jacketed triaxial test.

The boundary conditions at the two ends are as follows:

$$q_z = 0, \sigma_{zr} = \sigma_{z\theta} = 0, u_z\big|_{z=0} = 0 . \tag{4.2}$$

Finally, equilibrium condition in the z direction requires,

$$\frac{F(t)}{2\pi} = \int_0^R \sigma_{zz} r dr . \tag{4.3}$$

With the aforementioned conditions, the experimental setup becomes a generalized plane-strain axisymmetric problem, with all shear stresses and shear strains on the

principal planes vanish, and all dynamic and kinematic variables except u_z independent of z.

4.3 Analytical Solution

4.3.1 Poroelastic Solution

The constitutive relations for cylindrically orthotropic poroelasticity in polar coordinates are as follows:

$$\sigma_{rr} = M_{11}\varepsilon_{rr} + M_{12}\varepsilon_{\theta\theta} + M_{13}\varepsilon_{zz} + \alpha_1 p\,, \tag{4.4}$$

$$\sigma_{\theta\theta} = M_{12}\varepsilon_{rr} + M_{22}\varepsilon_{\theta\theta} + M_{23}\varepsilon_{zz} + \alpha_2 p\,, \tag{4.5}$$

$$\sigma_{zz} = M_{13}\varepsilon_{rr} + M_{23}\varepsilon_{\theta\theta} + M_{33}\varepsilon_{zz} + \alpha_3 p\,, \tag{4.6}$$

$$p = M\left(\alpha_1\varepsilon_{rr} + \alpha_2\varepsilon_{\theta\theta} + \alpha_3\varepsilon_{zz} + \zeta\right), \tag{4.7}$$

where σ_{ij} is the stress tensor, ε_{ij} is the strain tensor, M_{ij}'s are the drained moduli of the soil/rock matrix, p is the pore pressure, ζ is the variation of fluid content, α_i's are the anisotropic pore pressure coefficients, and M is the inverse of storage coefficient under constant strains. Other governing relations include:

Darcy's law in the radial direction,

$$q_r = -\frac{k_1}{\mu}\frac{\partial p}{\partial r}\,, \tag{4.8}$$

strain-displacement relations,

$$\varepsilon_{rr} = \frac{\partial u_r}{\partial r}\,, \tag{4.9}$$

$$\varepsilon_{\theta\theta} = \frac{u_r}{r}\,, \tag{4.10}$$

equilibrium in radial direction,

$$\frac{\partial \sigma_{rr}}{\partial r} + \frac{\sigma_{rr} - \sigma_{\theta\theta}}{r} = 0\,, \tag{4.11}$$

and continuity equation,

$$\frac{\partial \zeta}{\partial t} - \frac{k_1}{\mu}\left(\frac{\partial^2}{\partial r^2} + \frac{1}{r}\frac{\partial}{\partial r}\right)p = 0\,, \tag{4.12}$$

where q_r, k_1, and u_r are the fluid flux, permeability, and displacement in the radial direction, and μ is the pore fluid viscosity.

Substitution of constitutive relations into the equilibrium equation yields,

$$\begin{aligned} -\alpha_1 M \frac{\partial \zeta}{\partial r} = &\left(\frac{M_{11}}{\alpha_1} + \alpha_1 M\right)\frac{\partial}{\partial r}\left(\alpha_1 \varepsilon_{rr} + \alpha_2 \varepsilon_{\theta\theta}\right) \\ &+ M\left(\alpha_1 - \alpha_2\right)\frac{1}{r}\left(\alpha_1 \varepsilon_{rr} + \alpha_2 \varepsilon_{\theta\theta}\right) \\ &+ \left(M_{11} - M_{12}\right)\frac{\varepsilon_{rr}}{r} + \left(M_{12} - M_{22}\right)\frac{\varepsilon_{\theta\theta}}{r} + \left(M_{12} - M_{11}\frac{\alpha_2}{\alpha_1}\right)\frac{\partial \varepsilon_{\theta\theta}}{\partial r} \\ &+ \left[M_{13} - M_{23} + \alpha_3 M\left(\alpha_1 - \alpha_2\right)\right]\frac{\varepsilon_{zz}}{r} - \left(\alpha_1 - \alpha_2\right)M\frac{\zeta}{r}\,. \end{aligned} \tag{4.13}$$

This equation can be rewritten in the form:

$$-\alpha_1 M \frac{\partial \zeta}{\partial r} = \left(\frac{M_{11}}{\alpha_1} + \alpha_1 M\right)\frac{\partial}{\partial r}\left(\alpha_1 \varepsilon_{rr} + \alpha_2 \varepsilon_{\theta\theta}\right) + \Delta\,, \tag{4.14}$$

with,

$$\begin{aligned} \Delta = &M\left(\alpha_1 - \alpha_2\right)\frac{1}{r}\left(\alpha_1 \varepsilon_{rr} + \alpha_2 \varepsilon_{\theta\theta}\right) \\ &+ \left(M_{11} - M_{12}\right)\frac{\varepsilon_{rr}}{r} + \left(M_{12} - M_{22}\right)\frac{\varepsilon_{\theta\theta}}{r} + \left(M_{12} - M_{11}\frac{\alpha_2}{\alpha_1}\right)\frac{\partial \varepsilon_{\theta\theta}}{\partial r} \\ &+ \left[M_{13} - M_{23} + \alpha_3 M\left(\alpha_1 - \alpha_2\right)\right]\frac{\varepsilon_{zz}}{r} - \left(\alpha_1 - \alpha_2\right)M\frac{\zeta}{r}\,. \end{aligned} \tag{4.15}$$

Since the drained moduli M_{ij}'s of the matrix are much smaller than the bulk modulus K_s of the grains for all soils and many rocks, α_1 and α_2 are very close to unity.

Therefore, the difference between α_1 and α_2 are negligible compared to each pore pressure coefficient. Furthermore, material weak orthotropy gives $|M_{11} - M_{22}| << M_{11}, M_{22}$ and $|M_{13} - M_{23}| << M_{13}, M_{23}$. Assuming that the term Δ can be neglected compared to other terms, Eq. (4.14) simplifies to,

$$-\alpha_1 M \frac{\partial \zeta}{\partial r} = \left(\frac{M_{11}}{\alpha_1} + \alpha_1 M \right) \frac{\partial}{\partial r} \left(\alpha_1 \varepsilon_{rr} + \alpha_2 \varepsilon_{\theta\theta} \right). \tag{4.16}$$

It should be noted that the simplified Eq. (4.16) correctly reduces to corresponding exact relations for transverse isotropy and isotropy. The use of Eqs. (4.16) and (4.7) transforms the continuity equation into,

$$\frac{\partial \zeta}{\partial t} - c_1 \left(\frac{\partial^2 \zeta}{\partial r^2} + \frac{1}{r} \frac{\partial \zeta}{\partial r} \right) = 0 , \tag{4.17}$$

with $c_1 = \dfrac{k_1 M_{11} M}{\mu M_{11}^u}$, which has the Laplace transform of the form:

$$s\tilde{\zeta} - c_1 \left(\frac{\partial^2 \tilde{\zeta}}{\partial r^2} + \frac{1}{r} \frac{\partial \tilde{\zeta}}{\partial r} \right) = 0 . \tag{4.18}$$

Let $\xi = r\sqrt{s/c_1}$, Eq. (4.18) takes the form:

$$\xi^2 \frac{\partial^2 \tilde{\zeta}}{\partial \xi^2} + \xi \frac{\partial \tilde{\zeta}}{\partial \xi} - \xi^2 \tilde{\zeta} = 0 . \tag{4.19}$$

Eq. (4.19) is a modified Bessel equation of 0^{th} degree with the following solution:

$$\tilde{\zeta} = \frac{M_{11}^u}{M} C_1 I_0(\xi) \tag{4.20}$$

Eq. (4.20) already takes into account the fact that the variation of fluid content must be finite at $r = 0$. This result together with the displacement-strain relations gives the radial displacement of the form:

$$\widetilde{u}_r = -\frac{\alpha_1 C_1}{1+\alpha_2/\alpha_1} r f(\xi) + \frac{C_2}{1+\alpha_2/\alpha_1} r, \tag{4.21}$$

where $f(\xi) = {}_1F_2\left(\frac{1+\alpha_2/\alpha_1}{2}; 1, \frac{3+\alpha_2/\alpha_1}{2}; \frac{\xi^2}{4}\right)$ is a hypergeometric function of ξ. In the case of transverse isotropy, $\alpha_1 = \alpha_2$, this hypergeometric function simplifies to the familiar expression:

$${}_1F_2\left(1; 1, 2; \frac{\xi^2}{4}\right) = 2\frac{I_1(\xi)}{\xi}. \tag{4.22}$$

Other dynamic and kinematic quantities can then be found as follows:

$$\widetilde{\varepsilon}_{rr} = -\alpha_1 C_1 I_0(\xi) + \frac{\alpha_2 C_1}{1+\alpha_2/\alpha_1} f(\xi) + \frac{C_2}{1+\alpha_2/\alpha_1}, \tag{4.23}$$

$$\widetilde{\varepsilon}_{\theta\theta} = -\frac{\alpha_1 C_1}{1+\alpha_2/\alpha_1} f(\xi) + \frac{C_2}{1+\alpha_2/\alpha_1}, \tag{4.24}$$

$$\widetilde{p} = M_{11} C_1 I_0(\xi) + \alpha_1 M C_2 + \alpha_3 M \widetilde{\varepsilon}_{zz}, \tag{4.25}$$

$$\widetilde{\sigma}_{rr} = \frac{\lambda_{112}}{1+\alpha_2/\alpha_1} C_1 f(\xi) + \frac{M_{11}^u + M_{12}^u}{1+\alpha_2/\alpha_1} C_2 + M_{13}^u \widetilde{\varepsilon}_{zz}, \tag{4.26}$$

$$\widetilde{\sigma}_{\theta\theta} = \lambda_{112} C_1 I_0(\xi) - \frac{\lambda_{221}}{1+\alpha_2/\alpha_1} C_1 f(\xi) + \frac{M_{12}^u + M_{22}^u}{1+\alpha_2/\alpha_1} C_2 + M_{23}^u \widetilde{\varepsilon}_{zz}, \tag{4.27}$$

$$\widetilde{\sigma}_{zz} = \lambda_{113} C_1 I_0(\xi) + \frac{\lambda_{312}}{1+\alpha_2/\alpha_1} C_1 f(\xi) + \frac{M_{13}^u + M_{23}^u}{1+\alpha_2/\alpha_1} C_2 + M_{33}^u \widetilde{\varepsilon}_{zz}, \tag{4.28}$$

$$\widetilde{q}_r = -\frac{k_r}{\mu} M_{11} C_1 \sqrt{\frac{s}{c_1}} I_1(\xi), \tag{4.29}$$

Solving for boundary conditions $P_o(t)$, $p_o(t)$, and $F(t)$, the unknown coefficients C_1, C_2, and the transformed axial strain $\widetilde{\varepsilon}_{zz}$ can be found to be as follows:

$$C_1 = \frac{\alpha_1+\alpha_2}{D}\begin{Bmatrix} -M(\lambda_{113}+\lambda_{123})\widetilde{S}_o \\ -M(\lambda_{331}+\lambda_{332})\widetilde{P}_o \\ +\left[\alpha_3 M(\lambda_{113}+\lambda_{123})-(M_{13}+M_{23})M_{13}^u+M_{33}(M_{11}^u+M_{12}^u)\right]\widetilde{p}_o \end{Bmatrix}, \tag{4.30}$$

$$C_2 = \frac{1+\alpha_2/\alpha_1}{D}\begin{Bmatrix} -\left[(\alpha_1+\alpha_2)M_{11}M_{13}^u I_0(\beta)-\alpha_1\alpha_3 M\lambda_{112}f(\beta)\right]\widetilde{S}_o \\ +\left[(\alpha_1+\alpha_2)M_{11}M_{33}^u I_0(\beta)-\alpha_3 M h(\beta)\right]\widetilde{P}_o \\ +\left[M_{13}^u h(\beta)-\alpha_1\lambda_{112}M_{33}^u f(\beta)\right]\widetilde{p}_o \end{Bmatrix}, \tag{4.31}$$

$$\widetilde{\varepsilon}_{zz} = \frac{1}{D}\begin{Bmatrix} (\alpha_1+\alpha_2)\left[M_{11}(M_{11}^u+M_{12}^u)I_0(\beta)-\alpha_1 M\lambda_{112}f(\beta)\right]\widetilde{S}_o \\ -(\alpha_1+\alpha_2)\left[M_{11}(M_{13}^u+M_{23}^u)I_0(\beta)-M h(\beta)\right]\widetilde{P}_o \\ +\left[\alpha_1\lambda_{112}(M_{13}^u+M_{23}^u)f(\beta)-(M_{11}^u+M_{12}^u)h(\beta)\right]\widetilde{p}_o \end{Bmatrix}, \tag{4.32}$$

where,

$$\beta = R\sqrt{s/c_1}\,, \tag{4.33}$$

$$\begin{aligned} D = {} & (\alpha_1+\alpha_2)M_{11}\left[M_{33}^u(M_{11}^u+M_{12}^u)-M_{13}^u(M_{13}^u+M_{23}^u)\right]I_0(\beta) \\ & -\alpha_1 M\lambda_{112}(\lambda_{331}+\lambda_{332})f(\beta)-M(\lambda_{113}-\lambda_{132})h(\beta) \end{aligned} \tag{4.34}$$

$$h(\xi) = 2(\alpha_1+\alpha_2)\lambda_{113}\frac{I_1(\xi)}{\xi}+\alpha_1\lambda_{312}g(\xi), \tag{4.35}$$

$$g(\xi) = {}_1F_2\left(\frac{1+\alpha_2/\alpha_1}{2}; 2, \frac{3+\alpha_2/\alpha_1}{2}; \frac{\xi^2}{4}\right). \tag{4.36}$$

The analytical solution for a poroelastic cylindrical sample is therefore complete in the Laplace transform domain and can be easily inverted numerically to time domain using appropriate inversion algorithms.

4.3.2 Poroviscoelastic Solution

Invoking the correspondence principle between poroviscoelasticity and poroelasticity, the solution for poroviscoelastic weakly-orthotropic cylinders take the form:

$$\widetilde{\zeta} = \frac{\overline{M}_{11}^{u}}{\overline{M}} C_1 I_0(\xi), \tag{4.37}$$

$$\widetilde{u}_r = -\frac{\overline{\alpha}_1 C_1}{1+\overline{\alpha}_2/\overline{\alpha}_1} r f(\xi) + \frac{C_2}{1+\overline{\alpha}_2/\overline{\alpha}_1} r, \tag{4.38}$$

$$\widetilde{\varepsilon}_{rr} = -\overline{\alpha}_1 C_1 I_0(\xi) + \frac{\overline{\alpha}_2 C_1}{1+\overline{\alpha}_2/\overline{\alpha}_1} f(\xi) + \frac{C_2}{1+\overline{\alpha}_2/\overline{\alpha}_1}, \tag{4.39}$$

$$\widetilde{\varepsilon}_{\theta\theta} = -\frac{\overline{\alpha}_1 C_1}{1+\overline{\alpha}_2/\overline{\alpha}_1} f(\xi) + \frac{C_2}{1+\overline{\alpha}_2/\overline{\alpha}_1}, \tag{4.40}$$

$$\widetilde{p} = \overline{M}_{11} C_1 I_0(\xi) + \overline{\alpha}_1 \overline{M} C_2 + \overline{\alpha}_3 \overline{M} \widetilde{\varepsilon}_{zz}, \tag{4.41}$$

$$\widetilde{\sigma}_{rr} = \frac{\overline{\lambda}_{112}}{1+\overline{\alpha}_2/\overline{\alpha}_1} C_1 f(\xi) + \frac{\overline{M}_{11}^{u} + \overline{M}_{12}^{u}}{1+\overline{\alpha}_2/\overline{\alpha}_1} C_2 + \overline{M}_{13}^{u} \widetilde{\varepsilon}_{zz}, \tag{4.42}$$

$$\widetilde{\sigma}_{\theta\theta} = \overline{\lambda}_{112} C_1 I_0(\xi) - \frac{\overline{\lambda}_{221}}{1+\overline{\alpha}_2/\overline{\alpha}_1} C_1 f(\xi) + \frac{\overline{M}_{12}^{u} + \overline{M}_{22}^{u}}{1+\overline{\alpha}_2/\overline{\alpha}_1} C_2 + \overline{M}_{23}^{u} \widetilde{\varepsilon}_{zz}, \tag{4.43}$$

$$\widetilde{\sigma}_{zz} = \overline{\lambda}_{113} C_1 I_0(\xi) + \frac{\overline{\lambda}_{312}}{1+\overline{\alpha}_2/\overline{\alpha}_1} C_1 f(\xi) + \frac{\overline{M}_{13}^{u} + \overline{M}_{23}^{u}}{1+\overline{\alpha}_2/\overline{\alpha}_1} C_2 + \overline{M}_{33}^{u} \widetilde{\varepsilon}_{zz}, \tag{4.44}$$

$$\widetilde{q}_r = -\frac{k_r}{\mu} \overline{M}_{11} C_1 \sqrt{\frac{s}{c}} I_1(\xi), \tag{4.45}$$

with,

$$C_1 = \frac{\overline{\alpha}_1 + \overline{\alpha}_2}{D} \begin{Bmatrix} -\overline{M}\left(\overline{\lambda}_{113} + \overline{\lambda}_{123}\right)\widetilde{S}_o \\ -\overline{M}\left(\overline{\lambda}_{331} + \overline{\lambda}_{332}\right)\widetilde{P}_o \\ +\left[\overline{\alpha}_3 \overline{M}\left(\overline{\lambda}_{113} + \overline{\lambda}_{123}\right) - \left(\overline{M}_{13} + \overline{M}_{23}\right)\overline{M}_{13}^{u} + \overline{M}_{33}\left(\overline{M}_{11}^{u} + \overline{M}_{12}^{u}\right)\right]\widetilde{p}_o \end{Bmatrix}, \tag{4.46}$$

$$C_2 = \frac{1+\overline{\alpha}_2/\overline{\alpha}_1}{D} \begin{Bmatrix} -\left[\left(\overline{\alpha}_1 + \overline{\alpha}_2\right)\overline{M}_{11}\overline{M}_{13}^{u} I_0(\beta) - \overline{\alpha}_1 \overline{\alpha}_3 \overline{M\lambda}_{112} f(\beta)\right]\widetilde{S}_o \\ +\left[\left(\overline{\alpha}_1 + \overline{\alpha}_2\right)\overline{M}_{11}\overline{M}_{33}^{u} I_0(\beta) - \overline{\alpha}_3 \overline{M} h(\beta)\right]\widetilde{P}_o \\ +\left[\overline{M}_{13}^{u} h(\beta) - \overline{\alpha}_1 \overline{\lambda}_{112} \overline{M}_{33}^{u} f(\beta)\right]\widetilde{p}_o \end{Bmatrix}, \tag{4.47}$$

$$\widetilde{\varepsilon}_{zz} = \frac{1}{D}\begin{Bmatrix} (\overline{\alpha}_1 + \overline{\alpha}_2)\left[\overline{M}_{11}\left(\overline{M}^u_{11} + \overline{M}^u_{12}\right)I_0(\beta) - \overline{\alpha}_1\overline{M\lambda}_{112}f(\beta)\right]\widetilde{S}_o \\ -(\overline{\alpha}_1 + \overline{\alpha}_2)\left[\overline{M}_{11}\left(\overline{M}^u_{13} + \overline{M}^u_{23}\right)I_0(\beta) - \overline{M}h(\beta)\right]\widetilde{P}_o \\ +\left[\overline{\alpha}_1\overline{\lambda}_{112}\left(\overline{M}^u_{13} + \overline{M}^u_{23}\right)f(\beta) - \left(\overline{M}^u_{11} + \overline{M}^u_{12}\right)h(\beta)\right]\widetilde{p}_o \end{Bmatrix}, \tag{4.48}$$

$$\begin{aligned} D = {} & (\overline{\alpha}_1 + \overline{\alpha}_2)\overline{M}_{11}\left[\overline{M}^u_{33}\left(\overline{M}^u_{11} + \overline{M}^u_{12}\right) - \overline{M}^u_{13}\left(\overline{M}^u_{13} + \overline{M}^u_{23}\right)\right]I_0(\beta) \\ & - \overline{\alpha}_1\overline{M\lambda}_{112}\left(\overline{\lambda}_{331} + \overline{\lambda}_{332}\right)f(\beta) - \overline{M}\left(\overline{\lambda}_{113} - \overline{\lambda}_{132}\right)h(\beta) \end{aligned} \tag{4.49}$$

4.4 Numerical Example

A cylindrical clay sample with diameter of 10 cm and length of 20 cm under unconfined compression is studied in this analysis. A sudden compressive load giving an average axial stress of 100 kPa is applied at $t = 0$. Material properties are as follows: grain bulk modulus K_s = 40 GPa, pore fluid bulk modulus K_f = 2.3 GPa, porosity ϕ = 47%, permeability in the radial direction $k_1 = 10^{-16}$ m^2, and pore fluid viscosity μ = 0.001 Pa.s. The original transversely isotropic clay has $E_1(0^+) = E_2(0^+) = 3.0$ MPa, $E_3(0^+) = 1.2$ MPa, and Poisson's ratios $\nu_{21} = 0.3$, and $\nu_{31} = \nu_{32} = 0.2$. The cylindrically reinforced clay has weak orthotropy with $E_2(0^+) = 3.5$ MPa while other properties remain unchanged. The three Young's moduli are assumed to behave according to the Zener model with the same characteristic relaxation time of 600 seconds and long-time values equal to 80% of their initial values. The three Poisson's ratios, on the other hand, are assumed to remain constant in this analysis. However, they can be easily made time-dependent by modeling viscoelastic effects on the moduli M_{ij}'s instead of E_i's.

Fig. 4.2 demonstrates the evolution of pore pressure at the center of the original transversely isotropic clay and the reinforced orthotropic clay specimens with the Mandel-Cryer effect clearly displayed. The two materials give similar responses, with the orthotropic clay producing a little higher peak pore pressure.

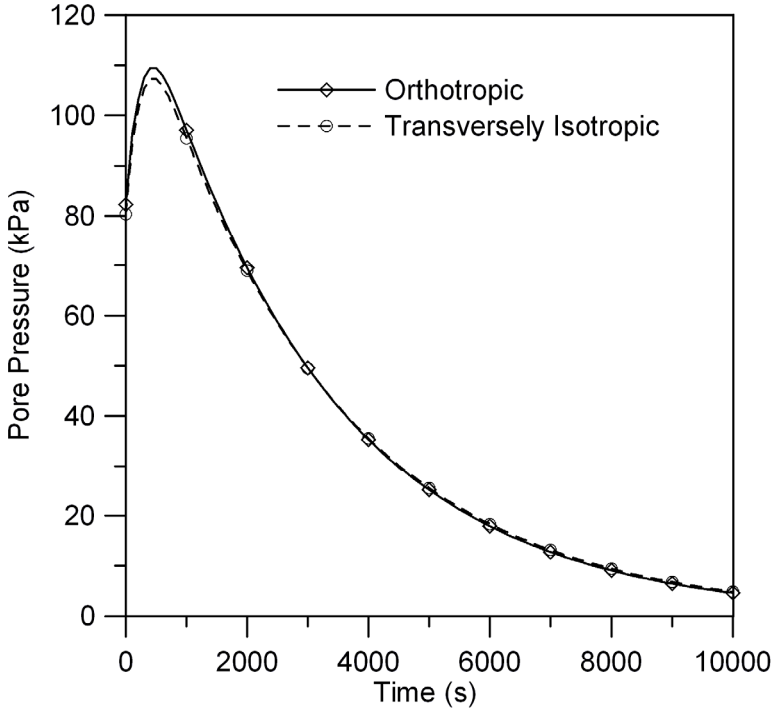

Fig. 4.2 – Pore pressure evolution at center of samples.

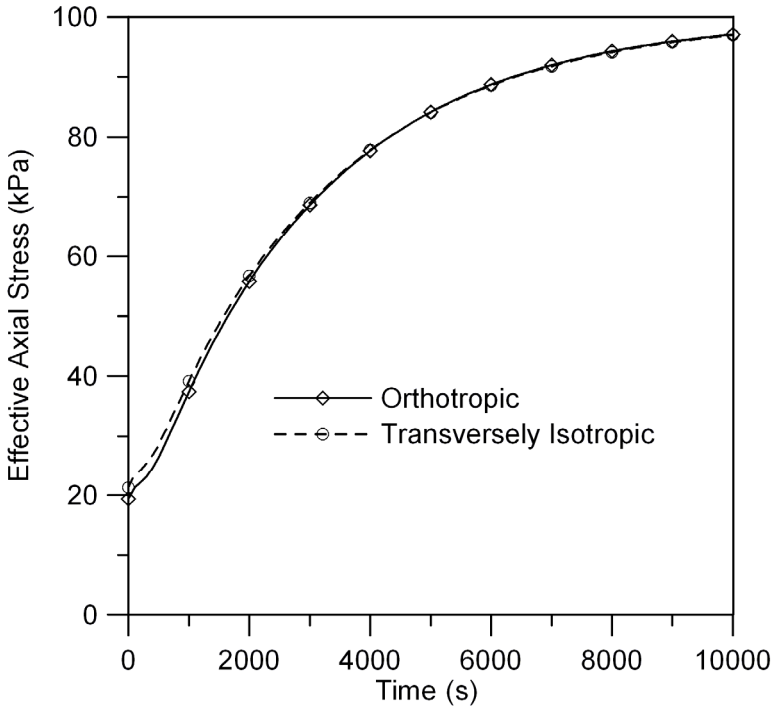

Fig. 4.3 – Evolution of effective axial stress at center of samples.

Fig. 4.3 and **Fig. 4.4** show the development with time of the effective axial stress and effective radial stress also at the center of the samples. The orthotropic clay

produces a little lower effective stresses partly due to the aforementioned presence of a higher pore pressure.

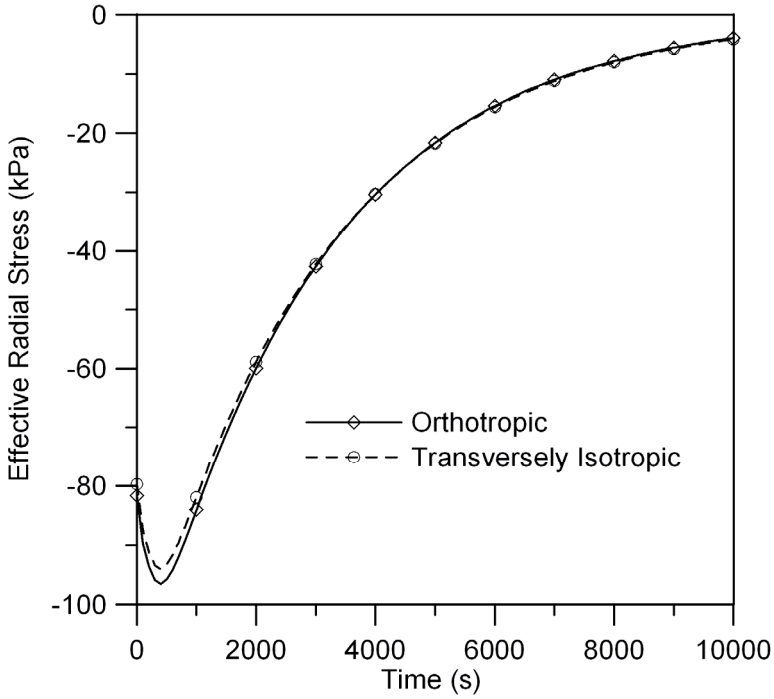

Fig. 4.4 – Evolution of effective radial stress at center of samples.

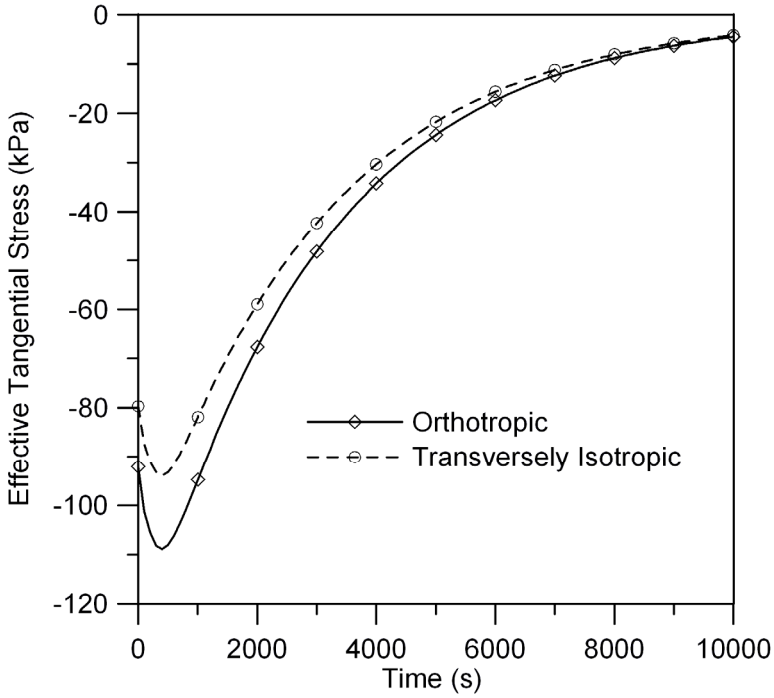

Fig. 4.5 – Evolution of effective tangential stress at center of sample.

The evolution of the effective tangential stress at the center of the samples is illustrated in **Fig. 4.5**. The two samples sustain very different stress levels because the impact of a changing E_2 is significant on the tangential stress.

The time-dependent axial compression of both samples is compared in **Fig. 4.6**. Since the axial compression in the unconfined compression test is predominantly controlled by the axial Young's modulus, E_3, it is natural that the two curves are similar.

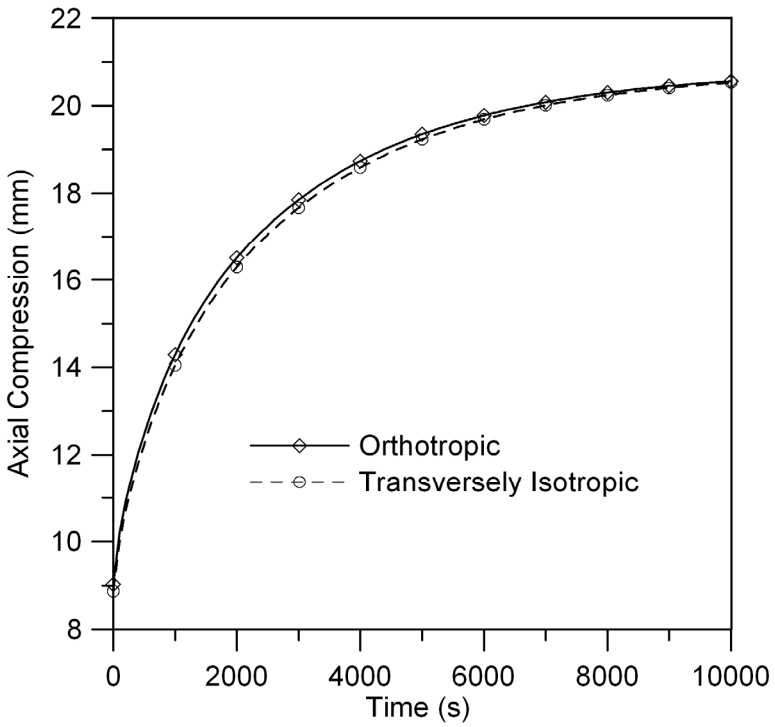

Fig. 4.6 – Axial compression of as functions of time.

Finally, the lateral dilation of the two specimens is compared in **Fig. 4.7**. Although they obtain the same long-time value due to identical Poisson's ratios, the transient behavior is appreciably different, with the orthotropic sample producing larger deformation.

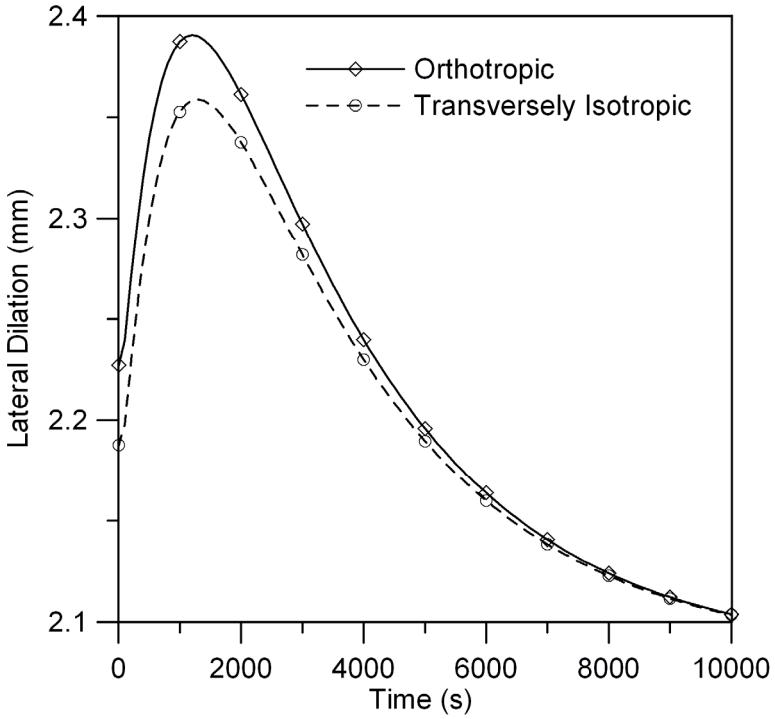

Fig. 4.7 – Lateral dilation as functions of time.

4.5 Summary

This chapter delineates the analytical solution for pore pressure, axial stress, radial stress, and tangential stress distributions, as well as the axial and radial displacements for weakly-orthotropic poroelastic or poroviscoelastic cylinders under triaxial or unconfined compression testing conditions. It has also been shown through numerical examples that compared to transversely isotropic samples, orthotropic specimens could have appreciably different effective tangential stress and lateral dilation evolutions.

Chapter 5: Orthotropic Rectangular Strips (Mandel's Problem)[2]

5.1 Introduction

Mandel's problem (Mandel, 1953) is one of the classical problems of poromechanics. In this problem, a long specimen with rectangular cross-section $2a \times 2b$ is sandwiched between two rigid, impermeable, frictionless plates, as illustrated in **Fig. 5.1**. A load $2F$ is then sudden applied at $t = 0$. Under these conditions, Mandel showed that the induced pore pressure at the center plane ($x = 0$) would increase above the initial "undrained" value before decreasing to 0. This non-monotonic behavior of the pore pressure response is termed the Mandel-Cryer effect and separates fully-coupled poromechanics from the earlier uncoupled theory of Terzaghi (1943). The Mandel-Cryer effect was confirmed experimentally first by Gibson et al. (1963). Since then, the Mandel's problem has been used extensively as a benchmark for validating numerical schemes in poromechanics (Christian and Boehmer, 1970; Cheng and Detournay, 1988; Cui et al., 1995).

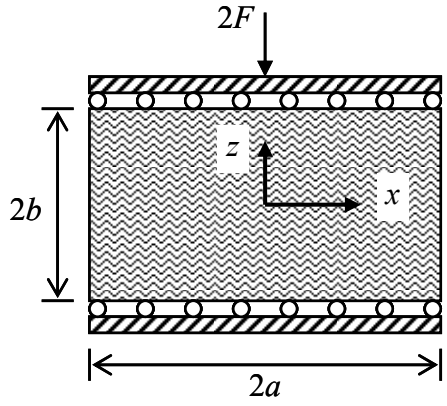

Fig. 5.1 – Schematic of the Mandel's problem.

[2] Parts of this chapter have been published in Hoang and Abousleiman (2005) and Hoang and Abousleiman (2009a)

Mandel's original paper (Mandel, 1953) only considered poroelastic isotropic materials. Abousleiman et al. (1996a) extended this solution to poroelastic transversely isotropic materials. In this chapter, the solution by Abousleiman et al. (1996a) will be extended to material orthotropy and general time-dependent loading $2F(t)$. Furthermore, the extended solution will be transferred to poroviscoelasticity using the correspondence principle developed in Chapter 2.

5.2 Potential Applications in Articular Cartilage Mechanics

The new solution will be of particular importance to the study of orthotropic articular cartilage. This vital load-bearing tissue has no blood supply. Therefore, an understanding of load-induced pore pressure and the resulting pore fluid diffusion is crucial in cartilage mechanics. Mechanically, this biological tissue composes of pore fluid, 60-85 percent by weight, and an anisotropic inhomogeneous viscoelastic matrix made up with proteoglycan aggregates and collagen fibers. The anisotropy and heterogeneity of the matrix are due in part to the orientation, size, and distribution of the collagen fibers. The cells, or chondrocytes, are limited in number and contribute little to the mechanical behavior of the tissue. However, cartilage components are produced by the cells, and cell behavior may be susceptible to stresses, fluid pressure, and pore fluid flux caused by external mechanical forces, especially since articular cartilage does not have a blood supply. Moreover, it has been speculated that the pore fluid squeezed out during mechanical loading of the tissue may play an important role in joint lubrication (McCutchen, 1962; Walker et al., 1968; Mansour and Mow, 1977). Ultimately, knowledge of stress and pore pressure distribution as well as pore fluid flow is essential to the understanding of cartilage biomechanics.

For orthotropic articular cartilage, an unconfined compression test of a strip with the length of the strip cut parallel or perpendicular to the split line, as shown in **Fig. 5.2**, can be conducted to take advantage of the newly-derived solution. With a large enough solution bath, the fluid pressure of the bath can be assumed to be constant.

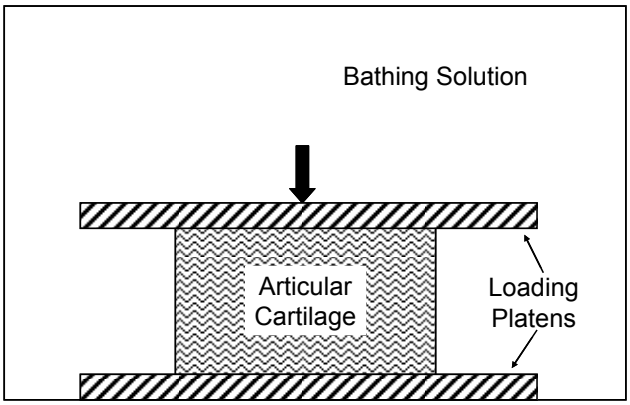

Fig. 5.2 – Unconfined compression test setup for a strip of articular cartilage.

5.3 Problem Description

As illustrated in **Fig. 5.1**, a long orthotropic specimen is sandwiched between two rigid, impermeable, frictionless plates. The *xy*, *xz*, and *yz* planes are chosen to coincide with the planes of material symmetry. Due to the sample geometry, material symmetry, and boundary conditions, every horizontal plane becomes a plane of folding symmetry and the pore fluid only diffuse along the *x* direction. It is also recognized that all shear stresses and shear strains vanish and all dynamic and kinematic variables except u_z independent of *z*.

The boundary conditions for this problem are as follows:

$$x = \pm a : \sigma_{xx} = \sigma_{xz} = p = 0 , \tag{5.1}$$

$$x = 0 : u_x = 0 , \tag{5.2}$$

$$z = \pm b : \sigma_{zx} = 0, q_z = 0, \int_{-a}^{a} \sigma_{zz} dx = 2F(t) , \tag{5.3}$$

$$z = -b : u_z = 0\,, \tag{5.4}$$

where u_i's are components of the displacement vector and $2F(t)$ is the time-dependent force per unit length applied to the rigid plates.

5.4 Analytical Solutions

5.4.1 Poroelastic Solution

Relevant orthotropic poroelastic constitutive relations for this problem are as follows:

$$\widetilde{\sigma}_{xx} = M_{11}\widetilde{\varepsilon}_{xx} + M_{12}\widetilde{\varepsilon}_{yy} + M_{13}\widetilde{\varepsilon}_{zz} + \alpha_1\widetilde{p}\,, \tag{5.5}$$

$$\widetilde{\sigma}_{yy} = M_{12}\widetilde{\varepsilon}_{xx} + M_{22}\widetilde{\varepsilon}_{yy} + M_{23}\widetilde{\varepsilon}_{zz} + \alpha_2\widetilde{p}\,, \tag{5.6}$$

$$\widetilde{\sigma}_{zz} = M_{13}\widetilde{\varepsilon}_{xx} + M_{23}\widetilde{\varepsilon}_{yy} + M_{33}\widetilde{\varepsilon}_{zz} + \alpha_3\widetilde{p}\,, \tag{5.7}$$

$$\widetilde{p} = M\left(\alpha_1\widetilde{\varepsilon}_{xx} + \alpha_2\widetilde{\varepsilon}_{yy} + \alpha_3\widetilde{\varepsilon}_{zz} + \widetilde{\zeta}\right). \tag{5.8}$$

Other governing equations include the equilibrium equation in the x direction,

$$\frac{\partial\widetilde{\sigma}_{xx}}{\partial x} = 0\,, \tag{5.9}$$

Darcy's law in the x direction,

$$\widetilde{q}_x = -\frac{k_1}{\mu}\frac{\partial\widetilde{p}}{\partial x}, \tag{5.10}$$

and the continuity equation,

$$s\widetilde{\zeta} + \frac{\partial\widetilde{q}_x}{\partial x} = 0\,. \tag{5.11}$$

The permeability k_1 is assumed to be independent of both time and deformation.

Combining the equations for Darcy's law and continuity yields,

$$s\widetilde{\zeta} - \frac{k_1}{\mu}\frac{\partial^2\widetilde{p}}{\partial x^2} = 0\,. \tag{5.12}$$

The constitutive relation for pore pressure transforms the above equation into,

$$s\tilde{\zeta} - \frac{k_1 M}{\mu}\frac{\partial^2 \tilde{\zeta}}{\partial x^2} - \frac{k_1 M \alpha_1}{\mu}\frac{\partial^2 \tilde{\varepsilon}_{xx}}{\partial x^2} = 0. \tag{5.13}$$

Substitution of Eqs. (1) and (4) into the equilibrium equation yields,

$$\frac{\partial \tilde{\varepsilon}_{xx}}{\partial x} = -\frac{M\alpha_1}{M_{11}^u}\frac{\partial \tilde{\zeta}}{\partial x}. \tag{5.14}$$

Substitution of Eq. (5.14) into Eq. (5.13) gives the diffusion equation for the variation of fluid content,

$$s\tilde{\zeta} - c_1\frac{\partial^2 \tilde{\zeta}}{\partial x^2} = 0, \tag{5.15}$$

with $c_1 = \dfrac{k_1 M_{11} M}{\mu M_{11}^u}$, which admits the following solution,

$$\tilde{\zeta} = C_1 \cosh\sqrt{\frac{s}{c_1}}x. \tag{5.16}$$

Eq. (5.16) already takes into account the fact that ζ is an even function of x. The axial stress and the pore pressure can then be expressed as functions of the axial strain ε_{zz}. Solving the boundary conditions for pore pressure and axial stress then gives the following formulas for ε_{zz} and C_1:

$$C_1 = \frac{M_{11}^u \lambda_{113}\sqrt{\dfrac{s}{c_1}}}{A_1 \sinh\sqrt{\dfrac{s}{c_1}}a - A_2\sqrt{\dfrac{s}{c_1}}a\cosh\sqrt{\dfrac{s}{c_1}}a}\tilde{F}, \tag{5.17}$$

$$\tilde{\varepsilon}_{zz} = -\frac{M_{11}M_{11}^u\sqrt{\dfrac{s}{c_1}}\cosh\sqrt{\dfrac{s}{c_1}}a}{A_1 \sinh\sqrt{\dfrac{s}{c_1}}a - A_2\sqrt{\dfrac{s}{c_1}}a\cosh\sqrt{\dfrac{s}{c_1}}a}\tilde{F}, \tag{5.18}$$

with,

$$A_1 = M\lambda_{113}^2, \tag{5.19}$$

$$A_2 = M_{11}[M_{11}^u M_{33}^u - (M_{13}^u)^2]. \tag{5.20}$$

The solution for the sample response can then be found explicitly as follows:

$$\widetilde{p} = \frac{MM_{11}\lambda_{113}\sqrt{\frac{s}{c_1}}\left(\cosh\sqrt{\frac{s}{c_1}}x - \cosh\sqrt{\frac{s}{c_1}}a\right)}{A_1\sinh\sqrt{\frac{s}{c_1}}a - A_2\sqrt{\frac{s}{c_1}}a\cosh\sqrt{\frac{s}{c_1}}a}\widetilde{F}, \tag{5.21}$$

$$\widetilde{\sigma}_{zz} = \frac{\sqrt{\frac{s}{c_1}}\left(A_1\cosh\sqrt{\frac{s}{c_1}}x - A_2\cosh\sqrt{\frac{s}{c_1}}a\right)}{A_1\sinh\sqrt{\frac{s}{c_1}}a - A_2\sqrt{\frac{s}{c_1}}a\cosh\sqrt{\frac{s}{c_1}}a}\widetilde{F}, \tag{5.22}$$

$$\widetilde{\varepsilon}_{xx} = \frac{\sqrt{\frac{s}{c_1}}\left(M_{11}M_{13}^u\cosh\sqrt{\frac{s}{c_1}}a - M\alpha_1\lambda_{113}\cosh\sqrt{\frac{s}{c_1}}x\right)}{A_1\sinh\sqrt{\frac{s}{c_1}}a - A_2\sqrt{\frac{s}{c_1}}a\cosh\sqrt{\frac{s}{c_1}}a}\widetilde{F}, \tag{5.23}$$

$$\widetilde{u}_x = \frac{M_{11}M_{13}^u\sqrt{\frac{s}{c_1}}x\cosh\sqrt{\frac{s}{c_1}}a - M\alpha_1\lambda_{113}\sinh\sqrt{\frac{s}{c_1}}x}{A_1\sinh\sqrt{\frac{s}{c_1}}a - A_2\sqrt{\frac{s}{c_1}}a\cosh\sqrt{\frac{s}{c_1}}a}\widetilde{F}, \tag{5.24}$$

$$\widetilde{u}_z = (z+b)\widetilde{\varepsilon}_{zz}, \tag{5.25}$$

$$\widetilde{q}_x = -\frac{k_1}{\mu}\frac{MM_{11}\lambda_{113}\frac{s}{c_1}\sinh\sqrt{\frac{s}{c_1}}x}{A_1\sinh\sqrt{\frac{s}{c_1}}a - A_2\sqrt{\frac{s}{c_1}}a\cosh\sqrt{\frac{s}{c_1}}a}\widetilde{F}. \tag{5.26}$$

5.4.2 Poroviscoelastic Solution

Invoking the correspondence principle between poroviscoelasticity and poroelasticity, the poroviscoelastic solution to the orthotropic Mandel's problem is as follows:

$$\widetilde{\varepsilon}_{xx} = \frac{\sqrt{\frac{s}{c_1}}\left(\overline{M}_{11}\overline{M}^{u}_{13}\cosh\sqrt{\frac{s}{c_1}}a - \overline{M}\overline{\alpha}_1\overline{\lambda}_{113}\cosh\sqrt{\frac{s}{c_1}}x\right)}{A_1\sinh\sqrt{\frac{s}{c_1}}a - A_2\sqrt{\frac{s}{c_1}}a\cosh\sqrt{\frac{s}{c_1}}a}\widetilde{F}, \tag{5.27}$$

$$\widetilde{\varepsilon}_{zz} = -\frac{\overline{M}_{11}\overline{M}^{u}_{11}\sqrt{\frac{s}{c_1}}\cosh\sqrt{\frac{s}{c_1}}a}{A_1\sinh\sqrt{\frac{s}{c_1}}a - A_2\sqrt{\frac{s}{c_1}}a\cosh\sqrt{\frac{s}{c_1}}a}\widetilde{F}, \tag{5.28}$$

$$\widetilde{u}_x = \frac{\overline{M}_{11}\overline{M}^{u}_{13}\sqrt{\frac{s}{c_1}}x\cosh\sqrt{\frac{s}{c_1}}a - \overline{M}\overline{\alpha}_1\overline{\lambda}_{113}\sinh\sqrt{\frac{s}{c_1}}x}{A_1\sinh\sqrt{\frac{s}{c_1}}a - A_2\sqrt{\frac{s}{c_1}}a\cosh\sqrt{\frac{s}{c_1}}a}\widetilde{F}, \tag{5.29}$$

$$\widetilde{u}_z = (z+b)\widetilde{\varepsilon}_{zz}, \tag{5.30}$$

$$\widetilde{p} = \frac{\overline{MM}_{11}\overline{\lambda}_{113}\sqrt{\frac{s}{c_1}}\left(\cosh\sqrt{\frac{s}{c_1}}x - \cosh\sqrt{\frac{s}{c_1}}a\right)}{A_1\sinh\sqrt{\frac{s}{c_1}}a - A_2\sqrt{\frac{s}{c_1}}a\cosh\sqrt{\frac{s}{c_1}}a}\widetilde{F}, \tag{5.31}$$

$$\widetilde{\sigma}_{zz} = \frac{\sqrt{\frac{s}{c_1}}\left(A_1\cosh\sqrt{\frac{s}{c_1}}x - A_2\cosh\sqrt{\frac{s}{c_1}}a\right)}{A_1\sinh\sqrt{\frac{s}{c_1}}a - A_2\sqrt{\frac{s}{c_1}}a\cosh\sqrt{\frac{s}{c_1}}a}\widetilde{F}, \tag{5.32}$$

$$\widetilde{q}_x = -\frac{\frac{k_1}{\mu}\overline{MM}_{11}\overline{\lambda}_{113}\frac{s}{c_1}\sinh\sqrt{\frac{s}{c_1}}x}{A_1\sinh\sqrt{\frac{s}{c_1}}a - A_2\sqrt{\frac{s}{c_1}}a\cosh\sqrt{\frac{s}{c_1}}a}\widetilde{F}, \tag{5.33}$$

with,

$$A_1 = \overline{M\lambda_{113}^2}, \tag{5.34}$$

$$A_2 = \overline{M}_{11}[\overline{M}_{11}^u \overline{M}_{33}^u - (\overline{M}_{13}^u)^2]. \tag{5.35}$$

5.5 Numerical Examples

An example illustrating the application of the analytical solution to cartilage mechanics is presented in this section. A specimen of 5 mm wide and 250 μm thick is cut along the split line direction. The force F on the specimen is chosen so that an average stress of 100 kPa is applied, or F = 2.5 N per cm of specimen length.

The familiar Zener model, used in many biomechanics studies to simulate material viscoelastic responses, (Leipzig and Athanasiou, 2005; Garcia and Cortes, 2007; Wilson et al., 2005) is adopted here for the moduli M_{11}, M_{22}, M_{33}, M_{12}, M_{23}, and M_{13}. More complex models can also be easily adopted. Based on the data reported by Chahine et al. (2004) for the superficial zone of bovine articular cartilage in 0.015M NaCl bathing solution, the orthotropic tissue is assumed to have the following long-time stiffness coefficients: $M_{11}(\infty)$ = 0.373 MPa, $M_{22}(\infty)$ = 0.464 MPa, $M_{33}(\infty)$ = 0.419 MPa, $M_{12}(\infty)$ = 0.0208 MPa, $M_{23}(\infty)$ = 0.0220 MPa, $M_{13}(\infty)$ = 0.0187 MPa. All six moduli are assumed to have the same characteristic relaxation time of 200 seconds and to retain 80% of their initial values at long time. Other parameters are assumed to be time-independent as follows: K_s = 3 MPa, ϕ = 0.852, $k_1/\mu = 4\times10^{-15}$ m^4/(N·s), K_f = 2.3 GPa. Another sample of the same dimensions is cut across the split line to investigate the effects of sample direction with respect to the natural fiber orientation. To investigate the effects of anisotropy, two simpler models of transverse isotropy (averaging M_{11} and M_{22} and averaging M_{13} and M_{23}) and isotropy (averaging M_{11}, M_{22}, and M_{33}, and averaging M_{12},

M_{13}, and M_{23}) are also considered. Finally, to investigate the effects of matrix viscoelasticity, the commonly used poroelastic analysis in cartilage biomechanics is also included; the six moduli, i.e. M_{11}, M_{22}, etc., in the poroelastic analysis are taken to be the long-time moduli following common biomechanics experimental practice.

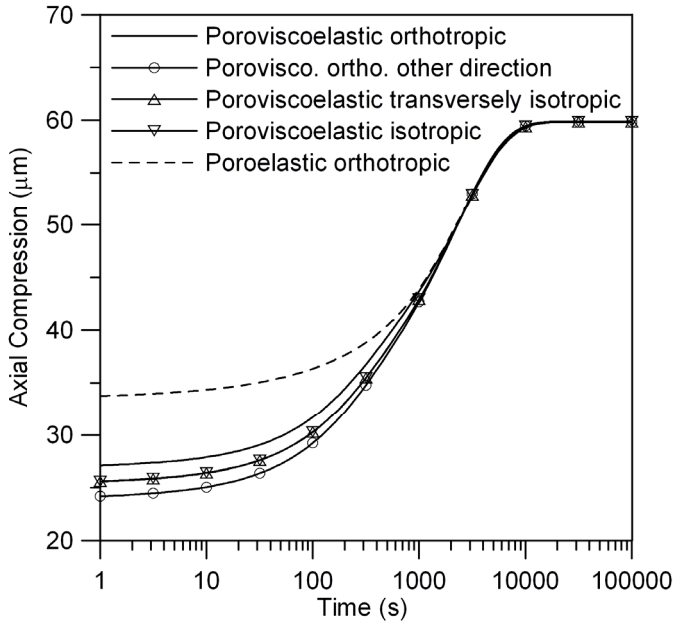

Fig. 5.3 – Axial compression of the specimen.

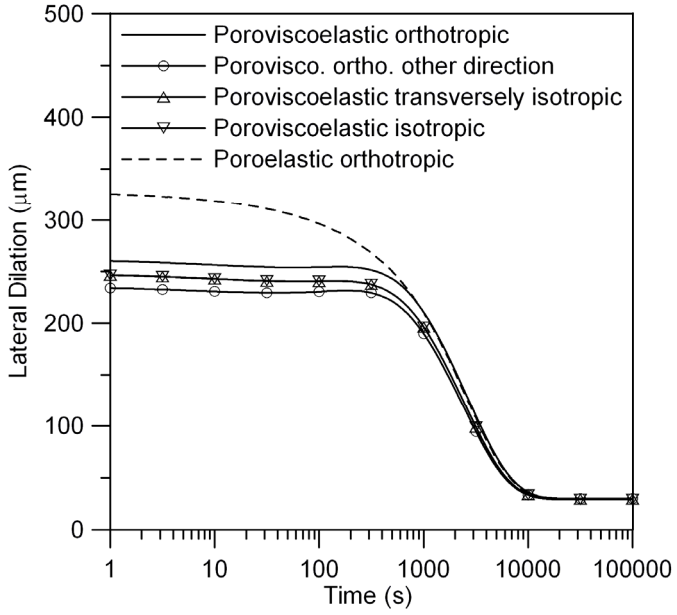

Fig. 5.4 – Lateral displacement of each side of the specimen.

The axial compression of the samples is shown in **Fig. 5.3**. Because the poroelastic modeling used long-time values of the stiffness coefficients, it matches very well with the sample behavior at long time. However, at short and intermediate times, it severely overestimates the compression of a stiffer poroviscoelastic sample, as expected. Regarding matrix anisotropy, the transversely isotropic and isotropic models with averaged properties produce predictions between those of the poroviscoelastic orthotropic samples.

Similarly, the lateral dilation of either side of the sample is captured very well by the poroelastic analysis at long time, as shown in **Fig. 5.4**. However, this commonly used model in biomechanics fails to capture the short-time and intermediate-time behavior of the poroviscoelastic tissue. Regarding matrix anisotropy, displacement predictions using models with lower degrees of anisotropy by averaging properties in different directions are between the real responses of the poroviscoelastic orthotropic samples.

5.6 Summary

The analytical solution for an orthotropic poroviscoelastic rectangular strip under axial loading (Mandel's problem) have been derived herein. The new solution will be particularly relevant to material testing and analysis of orthotropic poroviscoelastic biological tissues. Through the numerical examples, it has been shown that the poroelastic analysis commonly used in biomechanics will give erroneous predictions of the sample behavior at short and intermediate times even when the right degree of anisotropy is used. Similarly, any attempt to lower the anisotropy in poroviscoelastic

modeling by averaging material properties in different directions will compromise the prediction of sample responses to external loading.

Chapter 6: Transversely Isotropic Wellbores and Tunnels

6.1 Introduction

The stability of wellbores and tunnels is of fundamental importance in petroleum engineering and civil engineering. Wellbore instability issues cost the petroleum industry alone an estimated US$8 billions annually (Al-Wardy and Urdaneta, 2010; Diwan et al., 2011). Since the successful adaptation of Kirsch's classical elastic solution of a circular hole in an infinite plate (Kirsch, 1898) to simulate wellbore drilling and tunnel excavation (Bradley, 1979), many authors have advanced the modeling of this important problem by incorporating pore pressure effects (Carter and Booker, 1982; Carter and Booker, 1984; Detournay and Cheng, 1988; Rajapakse, 1993; Cui et al., 1997; Cui et al., 1998; Abousleiman and Cui, 1998; Cui et al., 1999; Li, 1999; Li and Flores-Berrones, 2002; Ekbote et al., 2004), poro-thermal effects (McTigue, 1990; Wang and Papamichos, 1994; Abousleiman and Ekbote, 2005; Chen and Ewy, 2005), poro-chemical effects (Sherwood and Bailey, 1994; Abousleiman et al., 1999; Abousleiman et al., 2000; Ekbote and Abousleiman, 2006; Nguyen and Abousleiman, 2010), poro-thermo-chemical effects (Ekbote and Abousleiman, 2005), effects of natural fractures (Li, 2003; Zhang et al., 2003; Nguyen et al., 2004; Abousleiman and Nguyen, 2005; Nguyen et al., 2007; Nguyen and Abousleiman, 2009; Nguyen et al., 2009), and rock rheology (Carter and Booker, 1983; Abousleiman et al., 1996b).

This chapter focuses on wellbore instability instances where the time-dependent borehole deformation is so excessive that it cannot be adequately explained by anything but the viscoelastic nature of the rock matrix itself. Notable rock formations with this

type of borehole failure are salt rock and shale. Some shales are known to cause repeated instability problems such as tight hole and stuck pipe despite repeated reaming and hole cleaning. Salt rock, on the other hand, has been known to flow like a viscoelastic liquid under certain downhole conditions and the drilling engineers may have only a short time window to install the casing before the wellbore becomes inaccessible. To model the poroviscoelastic response of the wellbore in such formations, the analytical poroelastic solution of an inclined borehole in a transversely isotropic rock formation (Abousleiman and Cui, 1998) is first revisited in this chapter. Sign convention for stresses and strains has been changed from tension positive (Abousleiman and Cui, 1998) to compression positive to accommodate common industry practice. The background (in-situ) state of stress and strain has been explicitly separated from the perturbation response since the focus of this study is the perturbation displacement field due to wellbore excavation. As a result of this explicit decomposition, Abousleiman and Cui's Problem II (uniaxial stress) is no longer needed. Furthermore, the wellbore pressure and the pore pressure boundary conditions have been modified from Heaviside step functions to general time-dependent functions to accommodate a wider range of field applications. The modified analytical poroelastic solution was then transferred to poroviscoelasticity using the correspondence principle established in Chapter 2. A numerical example of wellbore drilling through claystone using published field-measured rock viscoelastic properties (Zhifa et al., 2001) is also analyzed herein.

6.2 Problem Description

In this chapter, a wellbore drilled in any direction (inclination and azimuth) in a homogeneous and saturated soil/rock mass is considered. Specifically, vertical, horizontal, and inclined wellbores are special cases of the analysis. The surrounding formation is assumed to exhibit transverse isotropy, with the axis of material symmetry coinciding with the wellbore generator axis. The derived solution and analysis results in this chapter naturally extend to other circular excavations such as tunnels and drill shafts.

6.2.1 Coordinate Systems

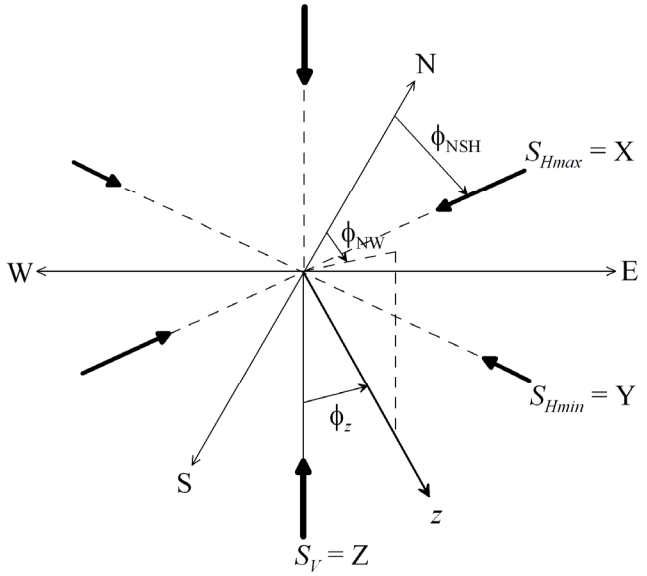

Fig. 6.1 – Wellbore generator axis with respect to the global coordinates N-E-Z and X-Y-Z.

In the global geological coordinate system N-E-Z with the Z axis pointing vertically downward, the azimuth of maximum horizontal in-situ stress S_{Hmax} and the inclination and azimuth of the wellbore generator axis are denoted ϕ_{NSH}, ϕ_z, and ϕ_{NW}, respectively, as illustrated in **Fig. 6.1**. For ease of mathematical modeling, a global geomechanics

coordinate system X-Y-Z is also used, with the X and Y axes coinciding with the directions of S_{Hmax} and S_{hmin}, respectively, as shown in **Fig. 6.1**.

To describe near-wellbore rock and fluid behaviors, local coordinate systems *x*-*y*-*z* and *r*-θ-*z* are also used, as shown in **Fig. 6.2**. The coordinate system *x*-*y*-*z* is obtained from X-Y-Z by such rotation that Z becomes *z* and *y* remains in the original horizontal plane (Cui et al., 1997). It is noted that in this configuration, the *x* axis always points toward the wellbore top for inclined and horizontal wellbores. Finally, the local polar coordinate system *r*-θ-*z* is simply the complementary polar coordinate system of *x*-*y*-*z*.

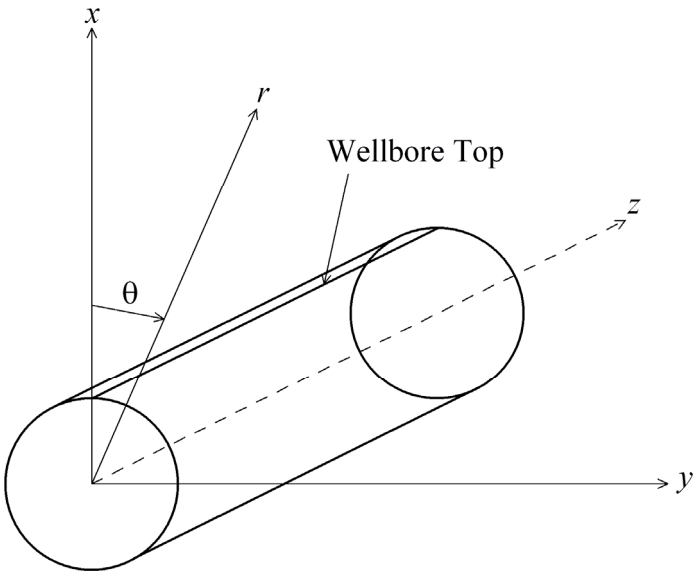

Fig. 6.2 – Local wellbore coordinates *x*-*y*-*z* and *r*-θ-*z*.

6.2.2 Boundary Conditions

Rotation of far-field stresses to the local wellbore coordinates *x*-*y*-*z* gives,

$$\begin{Bmatrix} S_x \\ S_y \\ S_z \\ S_{xy} \\ S_{yz} \\ S_{xz} \end{Bmatrix} = \begin{bmatrix} \left(a_x^X\right)^2 & \left(a_x^Y\right)^2 & \left(a_x^Z\right)^2 \\ \left(a_y^X\right)^2 & \left(a_y^Y\right)^2 & \left(a_y^Z\right)^2 \\ \left(a_z^X\right)^2 & \left(a_z^Y\right)^2 & \left(a_z^Z\right)^2 \\ a_x^X a_y^X & a_x^Y a_y^Y & a_x^Z a_y^Z \\ a_y^X a_z^X & a_y^Y a_z^Y & a_y^Z a_z^Z \\ a_z^X a_x^X & a_z^Y a_x^Y & a_z^Z a_x^Z \end{bmatrix} \begin{Bmatrix} S_H \\ S_h \\ S_V \end{Bmatrix}, \tag{6.1}$$

with the above [*a*] matrix coefficients expressed as,

$$\begin{bmatrix} a_x^X & a_y^X & a_z^X \\ a_x^Y & a_y^Y & a_z^Y \\ a_x^Z & a_y^Z & a_z^Z \end{bmatrix} = \begin{bmatrix} \cos\phi_z \cos\phi_{SH} & -\sin\phi_{SH} & \sin\phi_z \cos\phi_{SH} \\ \cos\phi_z \sin\phi_{SH} & \cos\phi_{SH} & \sin\phi_z \sin\phi_{SH} \\ -\sin\phi_z & 0 & \cos\phi_z \end{bmatrix}, \tag{6.2}$$

with $\phi_{SH} = \phi_{\mathrm{NSH}} - \phi_{\mathrm{NW}}$. Rotation of far-field stresses to the local wellbore coordinates *r*-θ-*z* yields,

$$S_r = P_0 + S_0 \cos 2\left(\theta - \theta_0\right), \tag{6.3}$$

$$S_\theta = P_0 - S_0 \cos 2\left(\theta - \theta_0\right), \tag{6.4}$$

$$S_{r\theta} = -S_0 \sin 2\left(\theta - \theta_0\right), \tag{6.5}$$

$$S_{rz} = S_{xz} \cos\theta + S_{yz} \sin\theta\,, \tag{6.6}$$

$$S_{\theta z} = -S_{xz} \sin\theta + S_{yz} \cos\theta\,, \tag{6.7}$$

with the following parameter definitions:

$$P_0 = \frac{S_x + S_y}{2}, \tag{6.8}$$

$$S_0 = \sqrt{\left(\frac{S_x - S_y}{2}\right)^2 + S_{xy}^2}\,, \tag{6.9}$$

$$\theta_0 = \frac{1}{2}\arctan\frac{2S_{xy}}{S_x - S_y}. \tag{6.10}$$

6.2.3 Decomposition Scheme

The original state of stress in the medium is as follows:

$$\sigma_{rr} = S_r, \tag{6.11}$$

$$\sigma_{\theta\theta} = S_\theta, \tag{6.12}$$

$$\sigma_{zz} = S_z, \tag{6.13}$$

$$\sigma_{r\theta} = S_{r\theta}, \tag{6.14}$$

$$\sigma_{rz} = S_{rz}, \tag{6.15}$$

$$\sigma_{\theta z} = S_{\theta z}, \tag{6.16}$$

$$p = p_0. \tag{6.17}$$

At far field, $r \to \infty$, all perturbation responses must vanish. The boundary conditions for the perturbation solution at far field are therefore as follows:

$$\sigma_{ij} = 0,\ p = 0. \tag{6.18}$$

On the other hand, the stresses and pressure at the wellbore wall are controlled by the introduction of the wellbore at $t = 0$. The boundary conditions for the perturbation solution at the wellbore wall, $r = R$, are therefore of the form:

$$\sigma_{rr} = -S_r H(t) + p_w(t), \tag{6.19}$$

$$\sigma_{r\theta} = -S_{r\theta} H(t), \tag{6.20}$$

$$\sigma_{rz} = -S_{rz} H(t), \tag{6.21}$$

$$p = -p_0 H(t) + p_i(t), \tag{6.22}$$

with p_w is the time-dependent mud pressure inside the well and p_i is the time-dependent mud pressure at the wellbore wall. The pressures p_w and p_i could have different values due to the presence of a mud cake. These complex boundary conditions at the wellbore wall for the perturbed state can be decomposed into three simpler problems as described below:

Plane strain axisymmetric problem, at $r = R$,

$$\sigma_{rr} = -P_0 H(t) + p_w(t), \tag{6.23}$$

$$\sigma_{r\theta} = 0, \tag{6.24}$$

$$p = -p_0 H(t) + p_i(t). \tag{6.25}$$

Plane strain deviatoric problem, at $r = R$,

$$\sigma_{rr} = -S_0 \cos 2(\theta - \theta_0) H(t), \tag{6.26}$$

$$\sigma_{r\theta} = S_0 \sin 2(\theta - \theta_0) H(t), \tag{6.27}$$

$$p = 0. \tag{6.28}$$

Anti-plane shear stress problem, at $r = R$,

$$\sigma_{rz} = -S_{rz} H(t). \tag{6.29}$$

These three problems can be solved separately and the resulting solutions can then be superposed to obtain the complete solution to the perturbation response. Superposition of the perturbed stress and pore pressure solution and the in-situ state of stress and pore pressure gives the actual time-dependent stress state of the formation surrounding the wellbore.

6.3 Analytical Solution

6.3.1 Poroelastic Solution

6.3.1.1 Poroelastic Governing Relations

The constitutive relations in cylindrical coordinates for a transversely isotropic poroelastic material are as follows:

$$\widetilde{\sigma}_{rr} = M_{11}\widetilde{\varepsilon}_{rr} + M_{12}\widetilde{\varepsilon}_{\theta\theta} + M_{13}\widetilde{\varepsilon}_{zz} + \alpha_1\widetilde{p}\,, \tag{6.30}$$

$$\widetilde{\sigma}_{\theta\theta} = M_{12}\widetilde{\varepsilon}_{rr} + M_{11}\widetilde{\varepsilon}_{\theta\theta} + M_{13}\widetilde{\varepsilon}_{zz} + \alpha_1\widetilde{p}\,, \tag{6.31}$$

$$\widetilde{\sigma}_{zz} = M_{13}\widetilde{\varepsilon}_{rr} + M_{13}\widetilde{\varepsilon}_{\theta\theta} + M_{33}\widetilde{\varepsilon}_{zz} + \alpha_3\widetilde{p}\,, \tag{6.32}$$

$$\widetilde{p} = M\left(\alpha_1\widetilde{\varepsilon}_{rr} + \alpha_1\widetilde{\varepsilon}_{\theta\theta} + \alpha_3\widetilde{\varepsilon}_{zz} + \widetilde{\zeta}\right), \tag{6.33}$$

$$\widetilde{\sigma}_{r\theta} = 2G\widetilde{\varepsilon}_{r\theta}\,, \tag{6.34}$$

with σ_{ij} is the stress tensor, ε_{ij} is the strain tensor, ζ is the variation of fluid content, M_{ij} is the stiffness tensor, α_1 and α_3 are the Biot's effective stress coefficients in the isotropic plane and the transverse direction, respectively, M is the inverse of the storage coefficient under constant strain, and G is the shear modulus in the isotropic plane. Other governing relations include Darcy's law, strain-displacement relations, equilibrium equations, and continuity equation as listed below.

Darcy's law,

$$\widetilde{q}_r = -\frac{k_1}{\mu}\frac{\partial\widetilde{p}}{\partial r}\,, \tag{6.35}$$

$$\widetilde{q}_\theta = -\frac{k_1}{\mu}\frac{1}{r}\frac{\partial\widetilde{p}}{\partial\theta}, \tag{6.36}$$

with k_1 is the permeability in the isotropic plane and μ denotes pore fluid viscosity.

Strain-displacement relations,

$$\widetilde{\varepsilon}_{rr} = \frac{\partial \widetilde{u}_r}{\partial r}, \tag{6.37}$$

$$\widetilde{\varepsilon}_{\theta\theta} = \frac{\widetilde{u}_r}{r} + \frac{1}{r}\frac{\partial \widetilde{u}_\theta}{\partial \theta}, \tag{6.38}$$

$$\widetilde{\varepsilon}_{r\theta} = \frac{1}{2}\left(\frac{1}{r}\frac{\partial \widetilde{u}_r}{\partial \theta} + \frac{\partial \widetilde{u}_\theta}{\partial r} - \frac{\widetilde{u}_\theta}{r}\right), \tag{6.39}$$

$$\widetilde{\omega}_z = \frac{1}{2}\left(-\frac{1}{r}\frac{\partial \widetilde{u}_r}{\partial \theta} + \frac{\partial \widetilde{u}_\theta}{\partial r} + \frac{\widetilde{u}_\theta}{r}\right). \tag{6.40}$$

Equilibrium equations,

$$\frac{\partial \widetilde{\sigma}_{rr}}{\partial r} + \frac{1}{r}\frac{\partial \widetilde{\sigma}_{\theta r}}{\partial \theta} + \frac{\widetilde{\sigma}_{rr} - \widetilde{\sigma}_{\theta\theta}}{r} = 0, \tag{6.41}$$

$$\frac{\partial \widetilde{\sigma}_{r\theta}}{\partial r} + \frac{1}{r}\frac{\partial \widetilde{\sigma}_{\theta\theta}}{\partial \theta} + 2\frac{\widetilde{\sigma}_{r\theta}}{r} = 0. \tag{6.42}$$

Continuity equation,

$$s\widetilde{\zeta} - \frac{k_1}{\mu}\left(\frac{\partial^2}{\partial r^2} + \frac{1}{r}\frac{\partial}{\partial r} + \frac{1}{r^2}\frac{\partial^2}{\partial \theta^2}\right)\widetilde{p} = 0. \tag{6.43}$$

6.3.1.2 Solution to the Plane Strain Axisymmetric Problem

Substitution of the constitutive relations into the equilibrium equation in radial direction yields the following Navier-type equation:

$$\frac{\partial\left(\widetilde{\varepsilon}_{\theta\theta} + \widetilde{\varepsilon}_{\theta\theta}\right)}{\partial r} = -\frac{\alpha_1 M}{M_{11}^u}\frac{\partial \widetilde{\zeta}}{\partial r}. \tag{6.44}$$

Substitution of the Navier-type equation into the continuity equation yields the following diffusion equation for the variation of fluid content:

$$s\widetilde{\zeta} - c_1\left(\frac{\partial^2}{\partial r^2} + \frac{1}{r}\frac{\partial}{\partial r}\right)\widetilde{\zeta} = 0, \tag{6.45}$$

with $c_1 = \frac{k_1}{\mu}\frac{M_{11}M}{M_{11}^u}$, of which the analytical solution is as follows:

$$\tilde{\zeta} = \frac{M_{11}^u}{M} C_1 K_0(\xi), \tag{6.46}$$

with $\xi = r\sqrt{s/c_1}$ and K_n is the modified Bessel function of the second kind of order n. The solution for ζ above already takes into account that ζ must stay finite as r approaches infinity. Substituting this solution into the Navier-type equation and integrating with respect to r yields the expression for the radial displacement,

$$\tilde{u}_r = \alpha_1 C_1 r \frac{K_1(\xi)}{\xi} + C_2 r. \tag{6.47}$$

The Laplace-domain solutions for all stresses, strains, pore pressure, and flux can then be easily obtained. Solving for the boundary conditions, the parameters C_1 and C_2 can be found to be as follows:

$$C_1 = \frac{-\frac{p_0}{s} + \tilde{p}_i}{M_{11} K_0(\beta)}, \tag{6.48}$$

$$C_2 = -\frac{\alpha_1 R^2}{M_{11}}\left(-\frac{p_0}{s} + \tilde{p}_i\right)\frac{1}{K_0(\beta)}\frac{K_1(\beta)}{\beta} - \frac{R^2}{2G}\left(-\frac{P_0}{s} + \tilde{p}_w\right), \tag{6.49}$$

with $\beta = R\sqrt{s/c_1}$. The displacement at the wellbore wall can then be easily found to be as follows:

$$\tilde{u}_r\big|_{r=R} = -\left(-\frac{P_0}{s} + \tilde{p}_w\right)\frac{R}{2G}. \tag{6.50}$$

For the plane strain axisymmetric problem, although the displacement field as a whole is dependent on the poroelastic properties of the rock formation, the displacement

at the wellbore wall is the same as in elasticity; it only depends on the shear modulus of the formation.

6.3.1.3 Solution to the Plane Strain Deviatoric Problem

Because of the symmetry of the problem, the response of the formation is assumed to take the following form:

$$\widetilde{\sigma}_{rr} = \Sigma_{rr} \cos 2(\theta - \theta_0), \tag{6.51}$$

$$\widetilde{\sigma}_{r\theta} = \Sigma_{r\theta} \sin 2(\theta - \theta_0), \tag{6.52}$$

$$\widetilde{\sigma}_{\theta\theta} = \Sigma_{\theta\theta} \cos 2(\theta - \theta_0), \tag{6.53}$$

$$\widetilde{p} = P \cos 2(\theta - \theta_0), \tag{6.54}$$

$$\widetilde{u}_r = U_r \cos 2(\theta - \theta_0), \tag{6.55}$$

$$\widetilde{u}_\theta = U_\theta \sin 2(\theta - \theta_0), \tag{6.56}$$

$$\widetilde{\varepsilon}_{rr} = E_{rr} \cos 2(\theta - \theta_0), \tag{6.57}$$

$$\widetilde{\varepsilon}_{\theta\theta} = E_{\theta\theta} \cos 2(\theta - \theta_0), \tag{6.58}$$

$$\widetilde{\varepsilon}_{r\theta} = E_{r\theta} \sin 2(\theta - \theta_0), \tag{6.59}$$

$$\widetilde{\omega}_z = W_z \sin 2(\theta - \theta_0), \tag{6.60}$$

$$\widetilde{\zeta} = Z \cos 2(\theta - \theta_0), \tag{6.61}$$

$$\widetilde{q}_r = Q_r \cos 2(\theta - \theta_0), \tag{6.62}$$

$$\widetilde{q}_\theta = Q_\theta \sin 2(\theta - \theta_0). \tag{6.63}$$

Substitution of the constitutive relations into the equilibrium equations leads to the following relations:

$$M_{11}^{u}\frac{\partial(\widetilde{\varepsilon}_{rr}+\widetilde{\varepsilon}_{\theta\theta})}{\partial r}+\alpha_1 M\frac{\partial\widetilde{\zeta}}{\partial r}-2G\frac{1}{r}\frac{\partial\widetilde{\omega}}{\partial\theta}=0\,, \tag{6.64}$$

$$M_{11}^{u}\frac{1}{r}\frac{\partial(\widetilde{\varepsilon}_{rr}+\widetilde{\varepsilon}_{\theta\theta})}{\partial\theta}+\alpha_1 M\frac{1}{r}\frac{\partial\widetilde{\zeta}}{\partial\theta}+2G\frac{\partial\widetilde{\omega}}{\partial r}=0\,. \tag{6.65}$$

The introduction of a new function ϕ satisfying $\frac{M_{11}^{u}}{2G}(\widetilde{\varepsilon}_{rr}+\widetilde{\varepsilon}_{\theta\theta})+\frac{\alpha_1 M}{2G}\widetilde{\zeta}+\phi=0$ leads to,

$$\phi=\Phi\cos 2(\theta-\theta_0)\,, \tag{6.66}$$

$$\frac{\partial\Phi}{\partial r}=-2\frac{W_z}{r}, \tag{6.67}$$

$$-2\Phi=r\frac{\partial W_z}{\partial r}\,. \tag{6.68}$$

W_z therefore satisfies the following equation:

$$r^2\frac{\partial^2 W_z}{\partial r^2}+r\frac{\partial W_z}{\partial r}-4W_z=0\,. \tag{6.69}$$

Since W_z must stay bounded as r approaches infinity, it takes the following form:

$$W_z=\frac{M_{11}^{u}}{2G}\frac{C_3}{r^2}, \tag{6.70}$$

which leads to $\Phi=\frac{M_{11}^{u}}{2G}\frac{C_3}{r^2}$. Substitution of ω_z and ϕ into the equilibrium equation and the continuity equation yields the following Navier-type equation and diffusion equation:

$$\nabla^2(\widetilde{\varepsilon}_{rr}+\widetilde{\varepsilon}_{\theta\theta})=-\frac{\alpha_1 M}{M_{11}^{u}}\nabla^2\widetilde{\zeta}\,, \tag{6.71}$$

$$s\widetilde{\zeta}-c_1\nabla^2\widetilde{\zeta}=0\,, \tag{6.72}$$

with $c_1 = \frac{k_1}{\mu}\frac{M_{11}M}{M_{11}^u}$ and $\nabla^2 = \frac{\partial^2}{\partial r^2} + \frac{1}{r}\frac{\partial}{\partial r} + \frac{1}{r^2}\frac{\partial^2}{\partial \theta^2}$ is the Laplacian in cylindrical coordinates. The angle-independent component of the variation of fluid content therefore takes the following form:

$$Z = \frac{M_{11}^u}{M} C_4 K_2(\xi), \tag{6.73}$$

with $\xi = r\sqrt{s/c_1}$ and K_n is the modified Bessel function of the second kind of order n. The displacement field can then be found to be as follows:

$$\widetilde{u}_r = \left\{ \frac{M_{11}^u}{2G}\frac{C_3}{r} + \frac{\alpha_1}{\sqrt{s/c_1}} C_4 \left[K_1(\xi) + 2\frac{K_2(\xi)}{\xi} \right] + \frac{C_5}{r^3} \right\} \cos 2(\theta - \theta_0), \tag{6.74}$$

$$\widetilde{u}_\theta = \left[-\frac{C_3}{2r} + \frac{2\alpha_1}{\sqrt{s/c_1}} C_4 \frac{K_2(\xi)}{\xi} + \frac{C_5}{r^3} \right] \sin 2(\theta - \theta_0). \tag{6.75}$$

The unknown parameters C3, C4, and C5 can then be found by solving the boundary conditions,

$$C_3 = 4\frac{S_0}{s} R^2 \frac{M_{11}K_2(\beta)}{(M_{11}^u + M_{12}^u)M_{11}K_2(\beta) - 4G\alpha_1^2 M \dfrac{K_1(\beta)}{\beta}}, \tag{6.76}$$

$$C_4 = 4\frac{S_0}{s} \frac{\alpha_1 M}{(M_{11}^u + M_{12}^u)M_{11}K_2(\beta) - 4G\alpha_1^2 M \dfrac{K_1(\beta)}{\beta}}, \tag{6.77}$$

$$C_5 = -\frac{S_0}{s}\frac{R^2}{2G} \frac{(M_{11}^u + M_{12}^u)M_{11}K_2(\beta) + 4G\alpha_1^2 M \dfrac{K_1(\beta)}{\beta} + 16G\alpha_1^2 M \dfrac{K_2(\beta)}{\beta^2}}{(M_{11}^u + M_{12}^u)M_{11}K_2(\beta) - 4G\alpha_1^2 M \dfrac{K_1(\beta)}{\beta}}. \tag{6.78}$$

6.3.1.4 Solution to the Anti-Plane Shear Problem

Using the displacement functions proposed by Hashin and Rosen (1964), the solution immediately after wellbore excavation can be found to be as follows:

$$u_r = u_\theta = 0, u_z = -S_{rz}\frac{R^2}{M_{44}r}, \tag{6.79}$$

$$\sigma_{rz} = -S_{rz}\frac{R^2}{r^2}, \tag{6.80}$$

$$\sigma_{\theta z} = S_{\theta z}\frac{R^2}{r^2}. \tag{6.81}$$

No normal strain is created in this mode of anti-plane shear loading. Hence, no pore pressure is generated and the solution is time-independent and elastic in nature. It is also noted that the displacement field produced by this mode of loading does not affect the size of the wellbore.

6.3.1.5 Superposed Displacement Field

At the wellbore wall, $r = R$, the radial and tangential displacements due to wellbore drilling are as follows:

$$\begin{aligned}\tilde{u}_r\big|_{r=R} = &-\left(-\frac{P_0}{s}+\tilde{p}_w\right)\frac{R}{2G} \\ &+\frac{S_0}{s}\frac{R}{2G}\frac{\left(3M_{11}^u - M_{12}^u\right)M_{11}K_2(\beta)+4G\alpha_1^2 M\dfrac{K_1(\beta)}{\beta}}{\left(M_{11}^u + M_{12}^u\right)M_{11}K_2(\beta)-4G\alpha_1^2 M\dfrac{K_1(\beta)}{\beta}}\cos 2(\theta-\theta_0),\end{aligned} \tag{6.82}$$

$$\tilde{u}_\theta\big|_{r=R} = -\frac{S_0}{s}\frac{R}{2G}\frac{\left(3M_{11}^u - M_{12}^u\right)M_{11}K_2(\beta)+4G\alpha_1^2 M\dfrac{K_1(\beta)}{\beta}}{\left(M_{11}^u + M_{12}^u\right)M_{11}K_2(\beta)-4G\alpha_1^2 M\dfrac{K_1(\beta)}{\beta}}\sin 2(\theta-\theta_0), \tag{6.83}$$

The deformed shape of the wellbore is therefore elliptical with the following semimajor and semiminor axes, respectively:

$$\tilde{a} = \frac{R}{s} + \left(-\frac{P_0}{s} + \tilde{p}_w \right) \frac{R}{2G} + \frac{S_0}{s} \frac{R}{2G} \frac{\left(3M_{11}^u - M_{12}^u\right) M_{11} K_2(\beta) + 4G\alpha_1^2 M \dfrac{K_1(\beta)}{\beta}}{\left(M_{11}^u + M_{12}^u\right) M_{11} K_2(\beta) - 4G\alpha_1^2 M \dfrac{K_1(\beta)}{\beta}}, \tag{6.84}$$

$$\tilde{b} = \frac{R}{s} + \left(-\frac{P_0}{s} + \tilde{p}_w \right) \frac{R}{2G} - \frac{S_0}{s} \frac{R}{2G} \frac{\left(3M_{11}^u - M_{12}^u\right) M_{11} K_2(\beta) + 4G\alpha_1^2 M \dfrac{K_1(\beta)}{\beta}}{\left(M_{11}^u + M_{12}^u\right) M_{11} K_2(\beta) - 4G\alpha_1^2 M \dfrac{K_1(\beta)}{\beta}}. \tag{6.85}$$

The semiminor axis is in the direction $\theta = \theta_0$ since maximum stress relief occurs in that direction. For isotropic rocks, Eqs. (6.84) and (6.85) simplify as follows:

$$\begin{aligned} \tilde{a} = {} & \frac{R}{s} + \left(-\frac{P_0}{s} + \tilde{p}_w \right) \frac{R}{2G} \\ & + \frac{S_0}{s} \frac{R}{2G} \frac{\left(K + \frac{5}{3}G + \alpha^2 M \right)\left(K + \frac{4}{3}G \right) K_2(\beta) + 2G\alpha^2 M \dfrac{K_1(\beta)}{\beta}}{\left(K + \frac{1}{3}G + \alpha^2 M \right)\left(K + \frac{4}{3}G \right) K_2(\beta) - 2G\alpha^2 M \dfrac{K_1(\beta)}{\beta}}, \end{aligned} \tag{6.86}$$

$$\begin{aligned} \tilde{b} = {} & \frac{R}{s} + \left(-\frac{P_0}{s} + \tilde{p}_w \right) \frac{R}{2G} \\ & - \frac{S_0}{s} \frac{R}{2G} \frac{\left(K + \frac{5}{3}G + \alpha^2 M \right)\left(K + \frac{4}{3}G \right) K_2(\beta) + 2G\alpha^2 M \dfrac{K_1(\beta)}{\beta}}{\left(K + \frac{1}{3}G + \alpha^2 M \right)\left(K + \frac{4}{3}G \right) K_2(\beta) - 2G\alpha^2 M \dfrac{K_1(\beta)}{\beta}}, \end{aligned} \tag{6.87}$$

where K and G are the bulk modulus and the shear modulus, respectively.

6.3.2 Poroviscoelastic Solution

Application of the correspondence principle in Laplace transform domain immediately gives the poroviscoelastic deformation of the wellbore:

$$\widetilde{u}_r\big|_{r=R} = -\left(-\frac{P_0}{s}+\widetilde{p}_w\right)\frac{R}{2\overline{G}}$$

$$+\frac{S_0}{s}\frac{R}{2\overline{G}}\frac{\left(3\overline{M}_{11}^u-\overline{M}_{12}^u\right)\overline{M}_{11}K_2(\beta)+4\overline{G}\,\overline{\alpha}_1^2\overline{M}\,\dfrac{K_1(\beta)}{\beta}}{\left(\overline{M}_{11}^u+\overline{M}_{12}^u\right)\overline{M}_{11}K_2(\beta)-4\overline{G}\,\overline{\alpha}_1^2\overline{M}\,\dfrac{K_1(\beta)}{\beta}}\cos 2(\theta-\theta_0), \tag{6.88}$$

$$\widetilde{u}_\theta\big|_{r=R} = -\frac{S_0}{s}\frac{R}{2\overline{G}}\frac{\left(3\overline{M}_{11}^u-\overline{M}_{12}^u\right)\overline{M}_{11}K_2(\beta)+4\overline{G}\,\overline{\alpha}_1^2\overline{M}\,\dfrac{K_1(\beta)}{\beta}}{\left(\overline{M}_{11}^u+\overline{M}_{12}^u\right)\overline{M}_{11}K_2(\beta)-4\overline{G}\,\overline{\alpha}_1^2\overline{M}\,\dfrac{K_1(\beta)}{\beta}}\sin 2(\theta-\theta_0), \tag{6.89}$$

$$\widetilde{a} = \frac{R}{s}+\left(-\frac{P_0}{s}+\widetilde{p}_w\right)\frac{R}{2\overline{G}}+\frac{S_0}{s}\frac{R}{2\overline{G}}\frac{\left(3\overline{M}_{11}^u-\overline{M}_{12}^u\right)\overline{M}_{11}K_2(\beta)+4\overline{G}\,\overline{\alpha}_1^2\overline{M}\,\dfrac{K_1(\beta)}{\beta}}{\left(\overline{M}_{11}^u+\overline{M}_{12}^u\right)\overline{M}_{11}K_2(\beta)-4\overline{G}\,\overline{\alpha}_1^2\overline{M}\,\dfrac{K_1(\beta)}{\beta}}, \tag{6.90}$$

$$\widetilde{b} = \frac{R}{s}+\left(-\frac{P_0}{s}+\widetilde{p}_w\right)\frac{R}{2\overline{G}}-\frac{S_0}{s}\frac{R}{2\overline{G}}\frac{\left(3\overline{M}_{11}^u-\overline{M}_{12}^u\right)\overline{M}_{11}K_2(\beta)+4\overline{G}\,\overline{\alpha}_1^2\overline{M}\,\dfrac{K_1(\beta)}{\beta}}{\left(\overline{M}_{11}^u+\overline{M}_{12}^u\right)\overline{M}_{11}K_2(\beta)-4\overline{G}\,\overline{\alpha}_1^2\overline{M}\,\dfrac{K_1(\beta)}{\beta}}. \tag{6.91}$$

Let R_c denote the outer radius of the casing, the maximum time available to set the casing from the instance of wellbore excavation can be calculated using the following relation:

$$b = R_c\,. \tag{6.92}$$

For isotropic rocks, Eqs. (6.90) and (6.91) simplify as follows:

$$\widetilde{a} = \frac{R}{s}+\left(-\frac{P_0}{s}+\widetilde{p}_w\right)\frac{R}{2\overline{G}}$$
$$+\frac{S_0}{s}\frac{R}{2\overline{G}}\frac{\left(\overline{K}+\dfrac{5}{3}\overline{G}+\overline{\alpha}^2\overline{M}\right)\left(\overline{K}+\dfrac{4}{3}\overline{G}\right)K_2(\beta)+2\overline{G}\,\overline{\alpha}^2\overline{M}\,\dfrac{K_1(\beta)}{\beta}}{\left(\overline{K}+\dfrac{1}{3}\overline{G}+\overline{\alpha}^2\overline{M}\right)\left(\overline{K}+\dfrac{4}{3}\overline{G}\right)K_2(\beta)-2\overline{G}\,\overline{\alpha}^2\overline{M}\,\dfrac{K_1(\beta)}{\beta}}, \tag{6.93}$$

$$\tilde{b} = \frac{R}{s} + \left(-\frac{P_0}{s} + \tilde{p}_w \right) \frac{R}{2\overline{G}} - \frac{S_0}{s} \frac{R}{2\overline{G}} \frac{\left(\overline{K} + \frac{5}{3}\overline{G} + \overline{\alpha}^2 \overline{M} \right)\left(\overline{K} + \frac{4}{3}\overline{G} \right) K_2(\beta) + 2\overline{G}\,\overline{\alpha}^2 \overline{M} \frac{K_1(\beta)}{\beta}}{\left(\overline{K} + \frac{1}{3}\overline{G} + \overline{\alpha}^2 \overline{M} \right)\left(\overline{K} + \frac{4}{3}\overline{G} \right) K_2(\beta) - 2\overline{G}\,\overline{\alpha}^2 \overline{M} \frac{K_1(\beta)}{\beta}}, \tag{6.94}$$

where K and G are the bulk modulus and the shear modulus, respectively.

6.4 Numerical Example and Discussion

In this section, a numerical example of wellbore drilling through a claystone formation is presented. The bulk mechanical properties of the rock are taken from a field study by Zhifa et al. (2001). The Young's modulus of the claystone is found by Zhifa et al. to be best represented by the Zener model, as shown in **Fig. 6.3** while the Poisson's ratio is constant at 0.33.

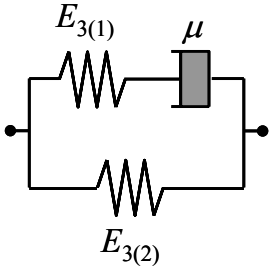

Fig. 6.3 – Zener model for the Young's modulus of claystone, $E_{3(1)}$ = 16.64 MPa, $E_{3(2)}$ = 68.32 MPa, μ = 2.43×10^{13} Pa-s (Zhifa et al., 2001).

Other rock properties are assumed to be as follows: porosity ϕ = 0.2, permeability k_1 = 1.0 mD, pore fluid viscosity μ = 1.0 cP, grain bulk modulus K_s = 40 GPa, pore fluid bulk modulus K_f = 2.3 GPa. To investigate the effects of the rock formation anisotropy, it will be assumed that the measured Young's modulus is in the direction perpendicular to bedding, E_3, while the Young's modulus parallel to bedding, E_1, is $n_E E_1$. Typical value of n_E is from 1.0 to 2.0. Three values of n_E of 1.0, 1.5, and 2.0 will therefore be

used in the following analyses. The Poisson's ratio, on the other hand, is assumed to be isotropic; however, this assumption can be relaxed without any difficulties.

Vertical wellbore drilling at a depth of 1000 m will be analyzed. The overburden stress gradient is assumed to be 2.30 g/cc. The maximum and minimum horizontal stresses are assumed to be the 0.9 and 0.8 times the overburden. For this in-situ state of stress, the axisymmetric and deviatoric stresses P_0 and S_0 equal 0.85 and 0.05 times the overburden, respectively. The pore pressure gradient is assumed to be 1 g/cc. The gravitational acceleration g is taken to be 9.81 m/s^2.

Some of the existing works in the literature model the time-dependent wellbore deformation using only viscoelasticity for simplicity (see for example Carcione et al. (2006)). To investigate the adequacy of such approach to modeling wellbore deformation in porous viscoelastic rock formations, a viscoelastic analysis has also been carried out for comparison using rock bulk properties identical to the poroviscoelastic analysis. The initial wellbore is assumed to be circular with a radius of 0.254 m for both analyses.

6.4.1.1 Balanced Drilling

The evolution of wellbore dimensions for the typical scenario of balanced drilling ($p_w = p_0$) will be investigated first. For balanced drilling, the formation of mudcake is unlikely. Therefore, p_i is assumed to be the same as p_w.

The evolution of the axisymmetric displacement at the wellbore wall due to the unloading of P_0 and the introduction of p_w is illustrated in **Fig. 6.4**. The poroviscoelastic and viscoelastic analyses yield identical results, as discussed in the derivation of the solution for the plane strain axisymmetric problem. As E_1 increases, the formation

becomes stiffer in the cross-sectional plane and therefore wellbore contraction decreases, as shown in **Fig. 6.4**.

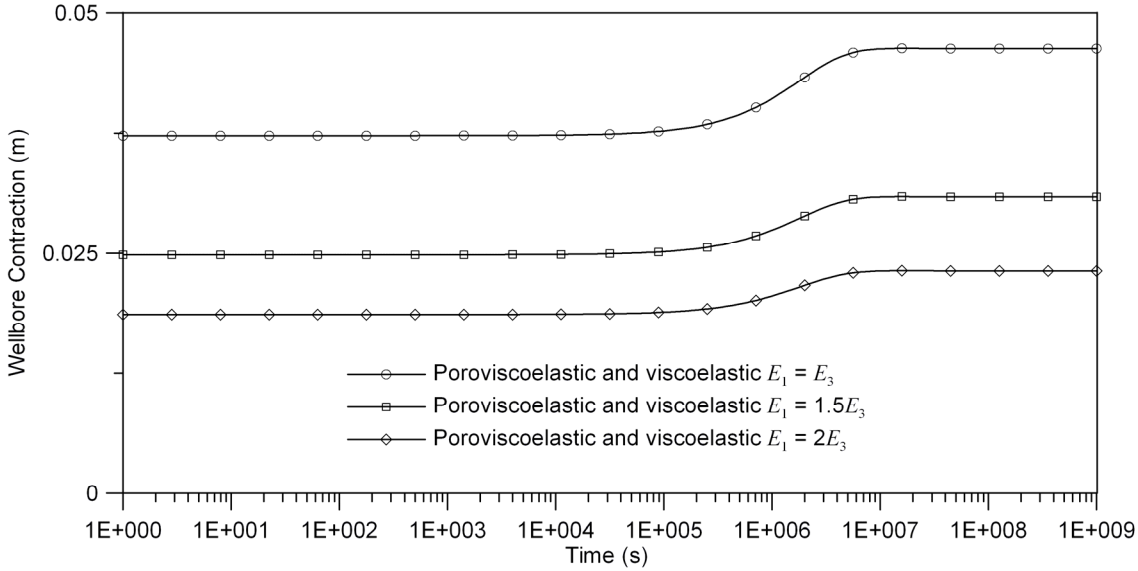

Fig. 6.4 – Evolution of the axisymmetric displacement due to the unloading of the axisymmetric in-situ stress $P_0 = 0.85\ S_V$ and the introduction of balanced drilling mudweight p_w = 1.0 g/cc.

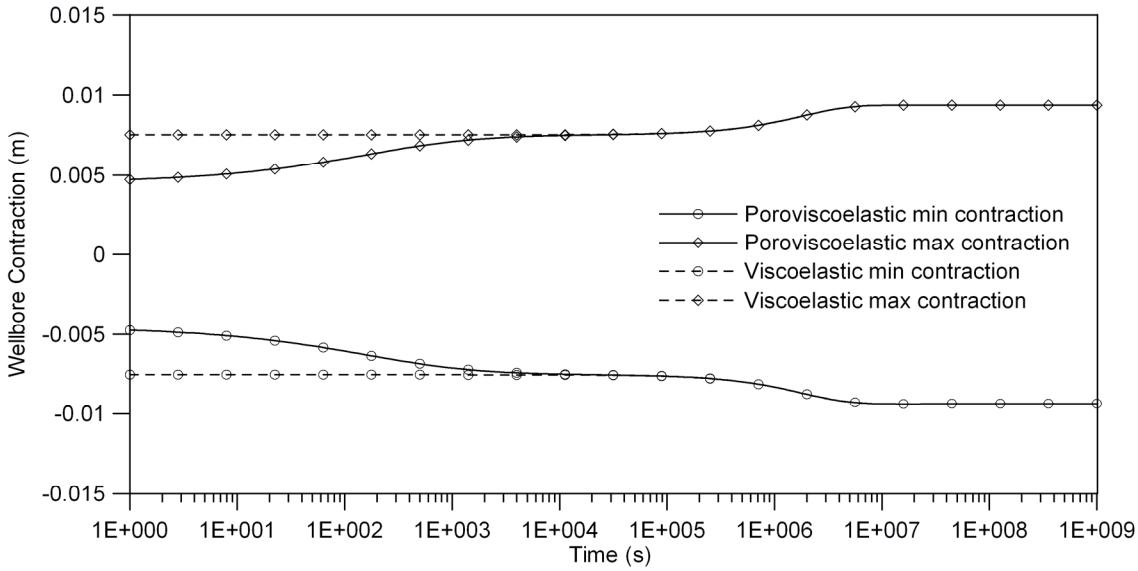

Fig. 6.5 – Evolution of the deviatoric displacements due to the unloading of the deviatoric stress $S_0 = 0.05\ S_V$, $E_1 = E_3$.

The evolution of the deviatoric displacements at the wellbore wall due to the unloading of the deviatoric stress S_0 is shown in **Fig. 6.5** to **Fig. 6.7**. At long times, when the pore pressure has reached equilibrium, the poroviscoelastic and viscoelastic

displacements are identical. However, at shorter times, the poroviscoelastic deformation is less than that predicted using viscoelasticity. Regarding the effects of formation anisotropy, the stiffer the Young's modulus in the cross-sectional plane, the smaller the wellbore contraction.

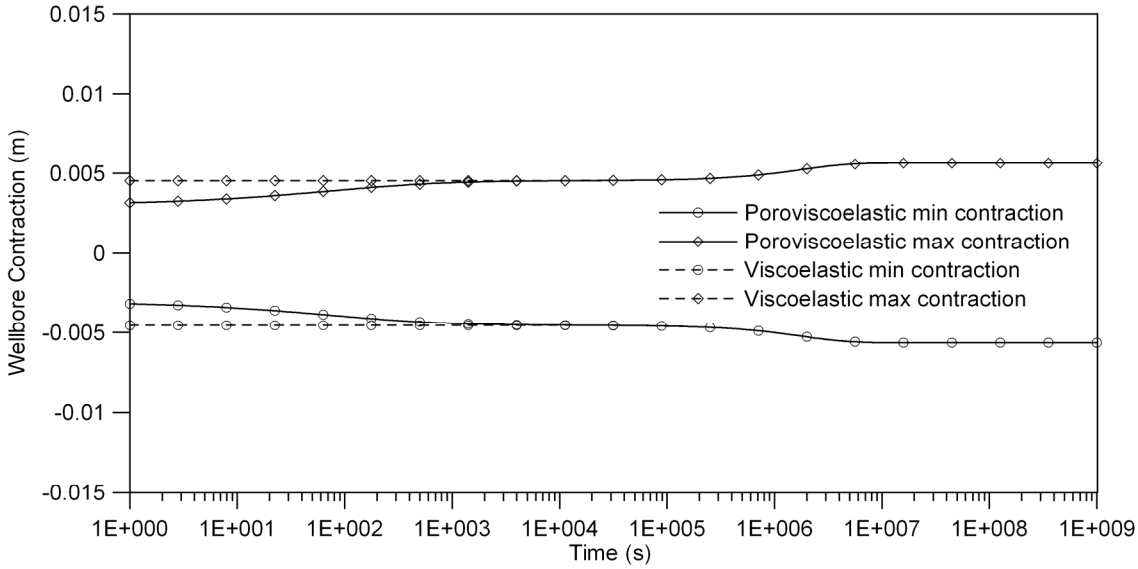

Fig. 6.6 – Evolution of the deviatoric displacements due to the unloading of the deviatoric stress $S_0 = 0.05\, S_V$, $E_1 = 1.5E_3$.

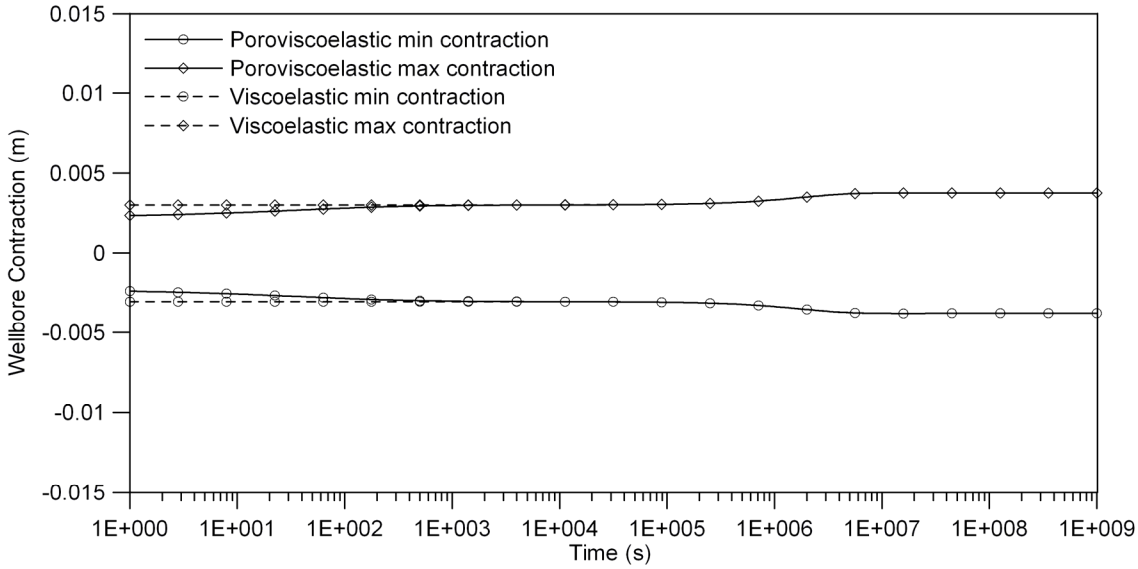

Fig. 6.7 – Evolution of the deviatoric displacements due to the unloading of the deviatoric stress $S_0 = 0.05\, S_V$, $E_1 = 2E_3$.

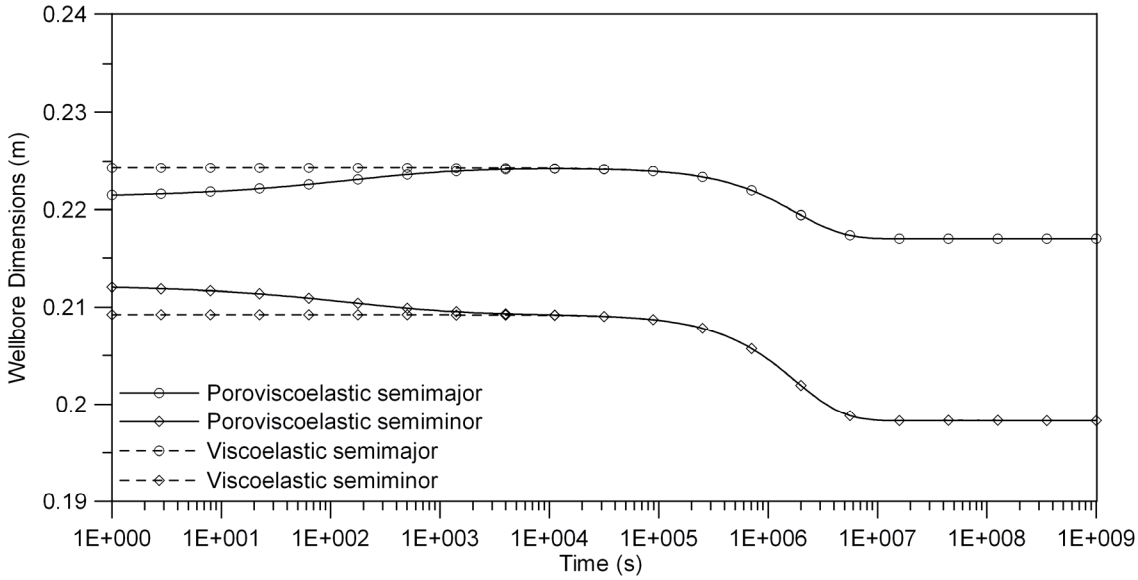

Fig. 6.8 – Evolution of wellbore dimensions for p_w = 1.0 g/cc, $E_1 = E_3$.

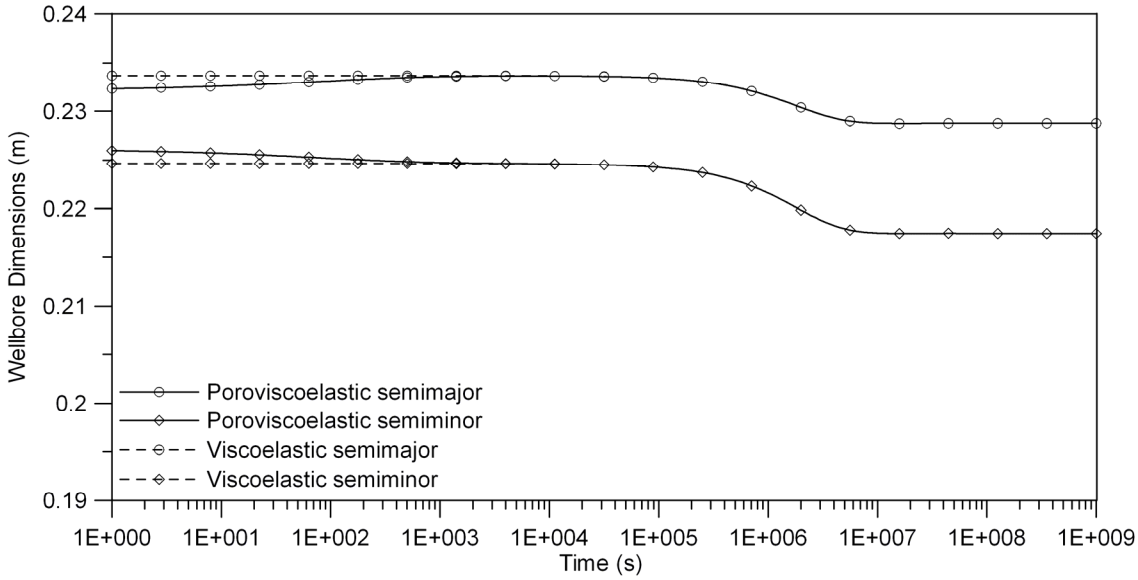

Fig. 6.9 – Evolution of wellbore dimensions for p_w = 1.0 g/cc, $E_1 = 1.5E_3$.

The actual evolution of the wellbore dimensions can be obtained through the superposition of the axisymmetric and deviatoric displacements, as shown in **Fig. 6.8** to **Fig. 6.10**. The time-variation of the semimajor of the elliptical wellbore is less than that of the semiminor for both the poroviscoelastic and the viscoelastic analyses because the axisymmetric and deviatoric displacements partly offset each other for the semimajor

(direction of minimum horizontal stress) while they complement each other for the semiminor (direction of maximum horizontal stress).

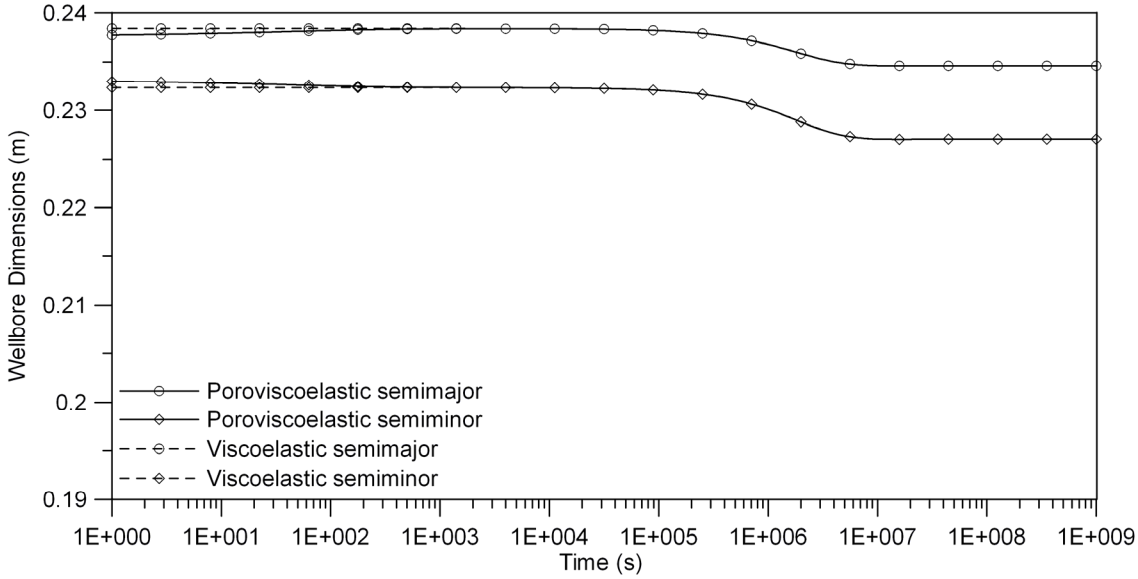

Fig. 6.10 – Evolution of wellbore dimensions for p_w = 1.0 g/cc, $E_1 = 2E_3$.

6.4.1.2 Overbalanced Drilling

A common practice to remedy the wellbore shrinkage problem in poroviscoelastic formation is to increase the drilling mudweight to apply additional pressure on the wellbore wall. In this section, the same well drilling scenario as in the previous section would be considered, except the mudweight is increased to 1.5 g/cc.

The evolution of the axisymmetric displacement at the wellbore wall due to the unloading of P_0 and the introduction of p_w is illustrated in **Fig. 6.11**. The poroviscoelastic and viscoelastic analyses again yield identical results, as predicted by the solution of the plane strain axisymmetric problem, but the magnitude of wellbore contraction is less than the case of balanced drilling thanks to the additional support of a higher mud pressure. The evolution of the deviatoric displacement is the same as in the

case of balanced drilling presented in the last section (**Fig. 6.5** to **Fig. 6.7**) since the deviatoric response is independent of the mud pressure.

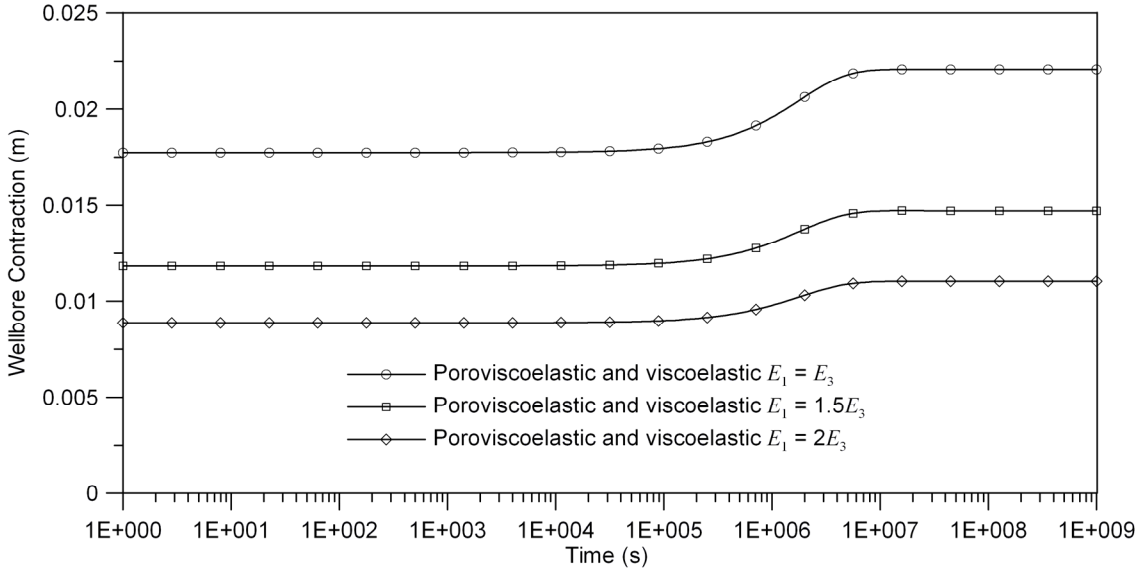

Fig. 6.11 – Evolution of the axisymmetric displacement due to the unloading of the axisymmetric stress $P_0 = 0.85\ S_V$ and the introduction of overbalanced drilling mudweight $p_w = 1.5$ g/cc.

Finally, the evolution of the wellbore dimensions is illustrated in **Fig. 6.12** to **Fig. 6.14**, with less wellbore shrinkage in the semiminor (maximum horizontal stress direction) compared to balanced drilling.

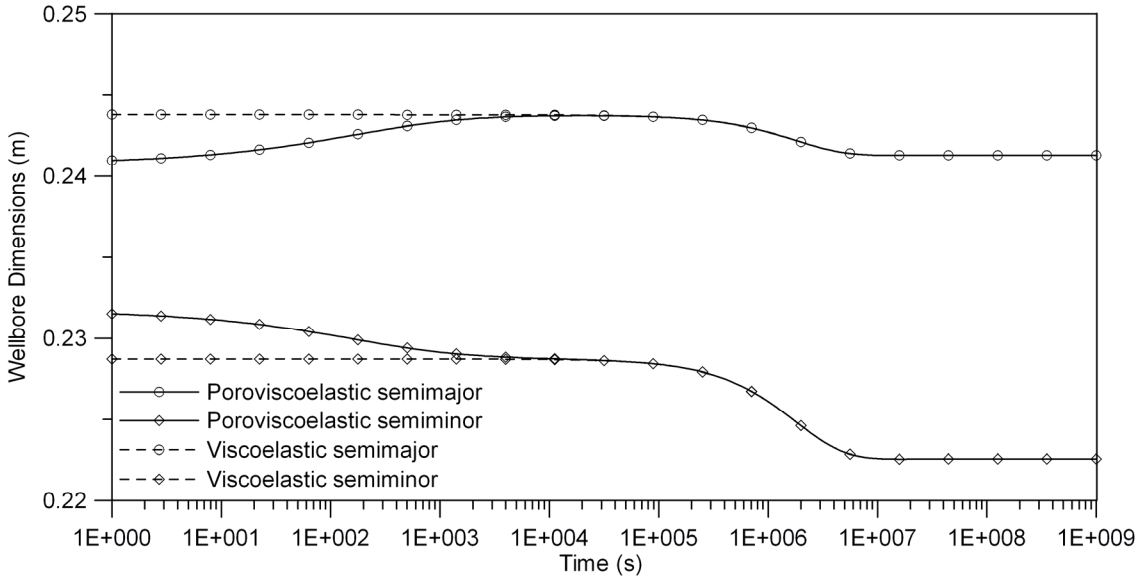

Fig. 6.12 – Evolution of wellbore dimensions for $p_w = 1.5$ g/cc, $E_1 = E_3$.

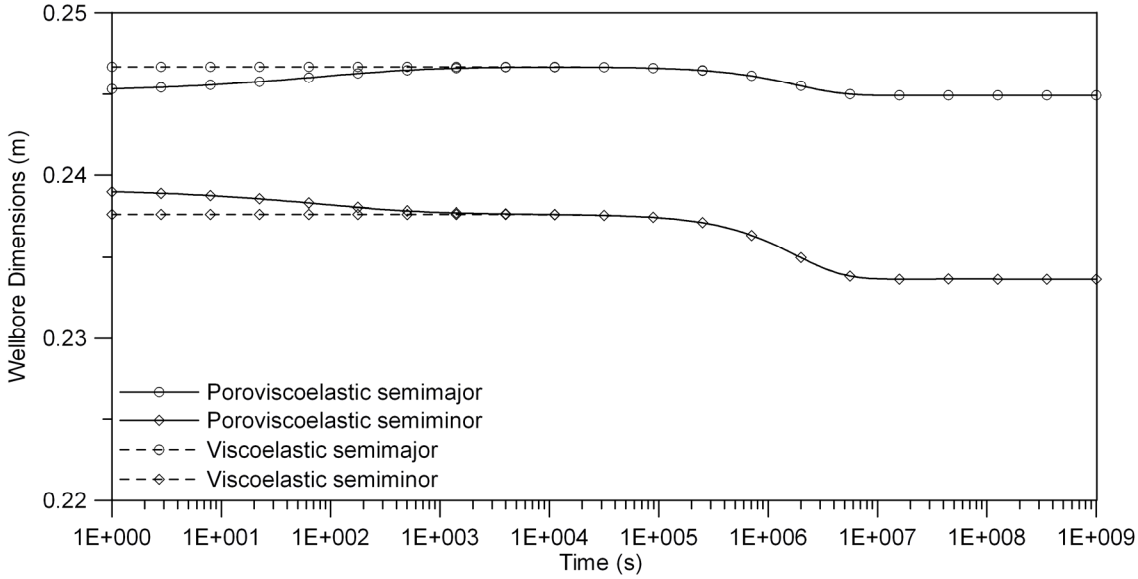

Fig. 6.13 – Evolution of wellbore dimensions for p_w = 1.5 g/cc, $E_1 = 1.5E_3$.

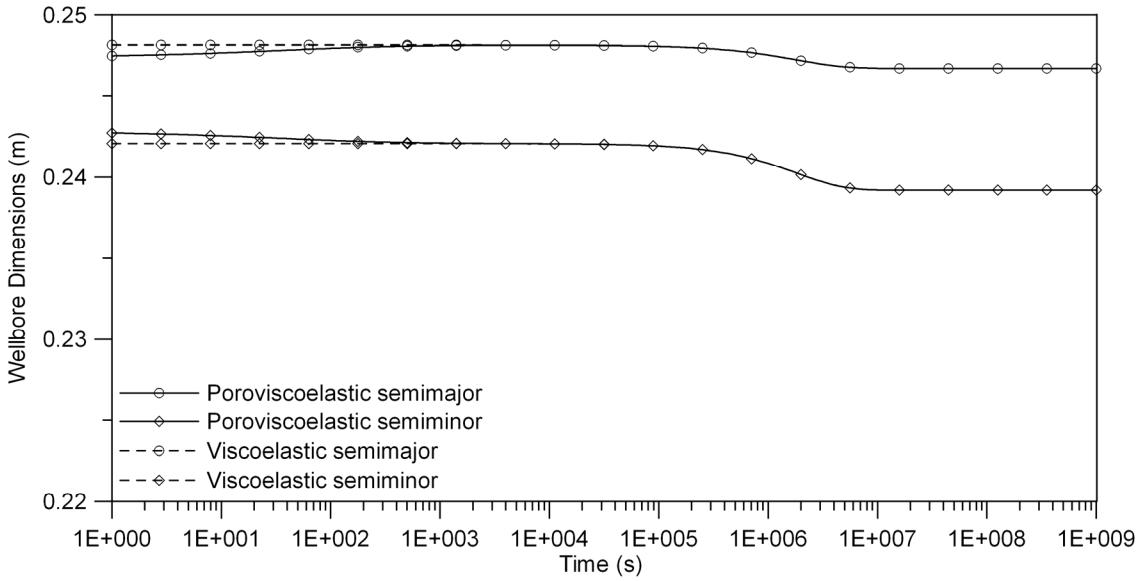

Fig. 6.14 – Evolution of wellbore dimensions for p_w = 1.5 g/cc, $E_1 = 2E_3$.

6.5 Summary

In this chapter, the analytical poroelastic solution of an inclined borehole in a transversely isotropic rock formation (Abousleiman and Cui, 1998) has been modified to explicitly calculate the deformation field induced by wellbore drilling. The modified solution has also been transferred to poroviscoelasticity using the correspondence

principle established in Chapter 2. The presented poroviscoelastic solution will be useful in design and analysis of wellbore drilling through rock formations with significant viscoelasticity in the rock matrix, such as salt rock and shales. Through the presented numerical examples of wellbore drilling through claystone using published field-measured rock viscoelastic properties, it is observed that the commonly used viscoelastic analysis for wellbores in poroviscoelastic formations gives adequate prediction of displacements at the wellbore wall at long times for but produces erroneous wellbore deformation predictions at shorter times if the in-situ stresses in the cross-section plane of the wellbore are non-hydrostatic. It has also been observed that formation anisotropy has a significant influence over the time-dependent wellbore displacement; specifically, higher stiffness in the cross-sectional plane of the wellbore results in smaller wellbore deformation.

Chapter 7: Conclusions

A rigorous proof of the correspondence principle between poroviscoelasticity and poroelasticity with general anisotropy has been presented in Chapter 2, both in time domain and in Laplace transform domain, for the general formulation as well as the material coefficients. Using this correspondence principle, analytical solutions in Laplace transform domain for poroviscoelasticity and poroelasticity can be readily transferred from one model to the other. Chapters 3 to 6 show detailed applications of this correspondence principle to various practical engineering problems, as described below.

Transversely isotropic cylinders under various loading and unloading conditions, with the axis of material symmetry coinciding with the axis of geometrical symmetry, have been analyzed in Chapter 3. This is one of the most useful and versatile class of solutions in both geomechanics and biomechanics, simulating a wide range of laboratory and field testing conditions (oedometer or K_0 test in geomechanics, confined compression test in biomechanics, unconfined compression test, unjacketed triaxial test, jacketed triaxial test, and strain recovery method). It has been shown mathematically and numerically that the sample response significantly depends on how the test is set up (lateral displacement is constrained or not). Specifically, the popular unconfined compression test and confined compression test in biomechanics are not equivalent as commonly believed. In particular, the confined compression test can be very misleading and should be accompanied by other testing techniques for mechanical characterization of anisotropic biological tissue. It has also been shown that for geomechanics, sample behavior should be closely monitored during the waiting time between confining

pressure application and axial loading, as these responses are particularly useful for differentiating the poroviscoelastic and/or anisotropic nature of the tested geo-material.

Chapter 4 presents an extension of the analytical solution and analyses of Chapter 3 to cylinders with material weak cylindrical-orthotropy under laboratory loading conditions, also with the axis of material symmetry coinciding with the axis of geometrical symmetry. This work can be of particular importance for cylindrically-reinforced low permeability clays with significant viscoelastic behavior. Potential applications of these materials might include nuclear waste storage, chemical waste storage, and viscoelastic settlement estimation. It has been shown that compared to transversely isotropic samples, orthotropic specimens could have appreciably different effective tangential stress and lateral dilation evolutions.

For geo-materials and biological tissues with Cartesian mechanical orthotropy, the symmetry of material properties implies that rectangular strips (Mandel's problem) are the best sample geometry to use for mechanical characterization. This setup has been studied in Chapter 5. Through the numerical examples, it has been shown that the poroelastic analysis commonly used in biomechanics will give erroneous predictions of the sample behavior at short and intermediate times even when the right degree of anisotropy is used. Similarly, any attempt to lower the anisotropy in poroviscoelastic modeling by averaging material properties in different directions will compromise the prediction of sample responses to external loading.

Finally, the important problem of wellbore drilling through transversely isotropic rocks has been considered in Chapter 6, with the emphasis on time-dependent displacement of the wellbore wall to investigate wellbore instability instances where the

time-dependent borehole deformation is so excessive that the viscoelastic nature of the rock matrix must be explicitly taken into account. Notable rock formations with such behavior are salt rock and shale. Through the presented numerical example of wellbore drilling through claystone using published field-measured rock viscoelastic properties, it has been shown that the simpler and commonly used viscoelastic analysis for wellbores in poroviscoelastic formations can give adequate prediction of displacements at the wellbore wall at long times for but produces erroneous wellbore deformation predictions at shorter times if the in-situ stresses in the cross-section plane of the wellbore are non-hydrostatic. The analytical solution and engineering analysis presented in this chapter can be readily applied to other circular excavations such as tunnels and drill shafts.

Bibliography

Abousleiman, Y., et al. 1993. A micromechanically consistent poroviscoelasticity theory for rock mechanics applications. *Int. J. Rock Mech. Min. Sci. & Geomech. Abstr.* 30(7):1177–1180.

Abousleiman, Y. and A. H–D. Cheng. 1996. Anelastic strain recovery of deep cores with presence of pore pressure. Engineering Mechanics 2, 935–938, Proceedings of the 11th Conference, Fort Lauderdale, FL, May 19–22, 1996.

Abousleiman, Y. and S. Ekbote. 2005. Solutions for the inclined borehole in a porothermoelastic transversely isotropic medium. *Journal of Applied Mechanics* 72(1):102–114.

Abousleiman, Y., et al. 1996a. Mandel's problem revisited. *Géotechnique* 46(2):187–195.

Abousleiman, Y., et al. 1996b. Poroviscoelastic analysis of borehole and cylinder problems. *Acta Mechanica* 119(1–4):199–219.

Abousleiman, Y., et al. 1999. Time-dependent coupled processes in wellbore design and stability: PBORE-3D. Paper SPE 56759 presented at the 1999 SPE ATCE, Houston, 3–6 October.

Abousleiman, Y., et al. 2000. Time-dependent wellbore in(stability) predictions: theory and case study. Paper IADC/SPE 62796 presented at the 2000 IADC/SPE Asia Pacific Drilling Technology, Kuala Lumpur, 11–13 September.

Abousleiman, Y. and L. Cui. 1998. Poroelastic solutions in transversely isotropic media for wellbore and cylinder. *Int. J. Solids Structures* 35:4905–4929.

Abousleiman, Y. and L. Cui. 2000. The theory of anisotropic poroelasticity with applications. In *Modeling in Geomechanics*, Eds: Zaman, M., Gioda, G., and J. Booker, Chichester: John Wiley & Sons, 559–593.

Abousleiman, Y. and V. Nguyen. 2005. Poromechanics response of inclined wellbore geometry in fractured porous media. *Journal of Engineering Mechanics* 131(11):1170–1183.

Al-Wardy, W. and O.P. Urdaneta. 2010. Geomechanical modeling for wellbore stability during drilling Nahr Umr shales in a field in petroleum development Oman. Paper SPE 138214 presented at the Abu Dhabi International Petroleum Exhibition & Conference, Abu Dhabi, UAE, 1–4 November.

Armstrong, C.G., Lai, W.M., and V.C. Mow. 1984. An analysis of the unconfined compression of articular cartilage. *Journal of Biomechanical Engineering* 106(2):165–173.

Armstrong, C.G. and V.C. Mow. 1982. Variations in the intrinsic mechanical properties of human articular cartilage with age, degeneration, and water content. *Journal of Bone and Joint Surgery*, American Volume 64, 88–94.

Anderson, D.R., Woo, S. L-Y., Kwan, M.K., and D.H. Gershuni. 1991. Viscoelastic shear properties of the equine medial meniscus. *Journal of Orthopaedic Research* 9(4): 550–558.

Baroud, G., Nemes, J., Ferguson, S.J., and T. Steffen. 2003. Material changes in osteoporotic human cancellous bone following infiltration with acrylic bone cement for a vertebral cement augmentation. *Computer Methods in Biomechanics and Biomedical Engineering* 6(2):133–139.

Biot, M. A. 1941. General theory of three-dimensional consolidation. *J. Appl. Phys.* 12(5):155–164.

Biot, M. A. 1955. Theory of elasticity and consolidation for a porous anisotropic solid. *J. Appl. Phys.* 26(2):182–185.

Biot, M. A. 1956. Theory of deformation of a porous viscoelastic anisotropic solid. *J. Appl. Phys.* 27(5):459–467.

Biot, M. A. 1973. Nonlinear and semilinear rheology of porous solids. *J. Geophys. Res.* 78(23):4924–4937.

Blanton, T.L. 1983. The relation between recovery deformation and in-situ stress magnitudes. Paper SPE/DOE 11624 presented at the 1983 SPE/DOE Symposium on Low Permeability, Denver, CO, 14–16 March.

Blanton, T.L. and L.W. Teufel. 1983. A field fest of the strain recovery method of stress determination in Devonian shale. Paper SPE 12304 presented at the Eastern Regional Meeting, Champion, Pennsylvania, 9–11 November.

Blanton, T.L. and L.W. Teufel. 1986. A critical evaluation of recovery deformation measurements as a means of in-situ stress determination. Paper SPE 15217 presented at the Unconventional Gas Technology Symposium, Louisville, Kentucky, 18–21 May.

Bloch, M., Siqueira, C.A.M., Ferreira, F.H., and J.C.J. Conceicao. 1997. Techniques for determining in-situ stress direction and magnitudes. Paper SPE 39075 presented at the Fifth Latin American and Caribbean Petroleum Engineering Conference and Exhibition, Rio de Janeiro, 30 August–3 September.

Boyde, A. and S.J. Jones. 1983. Scanning electron microscopy of cartilage. *Cartilage, Volume 1-Structure, Function, and Biochemistry*, Ed: Hall B.K., Academic Press, NY.

Bradley, W.B. 1979. Failure of inclined boreholes. Journal of Energy Resources Technology 101(4):232–239.

Bursać, P.M., Obitz, T.W., Eisenberg, S.R., and D. Stamenović. 1999. Confined and unconfined stress relaxation of cartilage: Appropriateness of a transversely isotropic analysis. *Journal of Biomechanics* 32(10):1125–1130.

Buschmann, M.D., Soulhat, J., Shirazi-Adl, A., Jurvelin, J.S., and E.B. Hunziker. 1998. Confined compression of articular cartilage: linearity in ramp and sinusoidal tests and the importance of interdigitation and incomplete confinement. *Journal of Biomechanics* 31(2):171–178.

Carcione, J.M. and F. Cavallini. 1995. Attenuation and quality factor surfaces in anisotropic-viscoelastic media. *Mechanics of Materials* 19(4):311-327.

Carcione, J.M., Helle, H.B., and A.F. Gangi. 2006. Theory of borehole stability when drilling through salt formations. *Geophysics* 71(3):F31–F47, doi: 10.1190/1.2195447.

Carter, J.P. and J.R. Booker. 1982. Elastic consolidation around a deep circular tunnel. *Int. J. Solids Structures* 18(12):1059–1074.

Carter, J.P. and J.R. Booker. 1983. Creep and consolidation around circular openings in finite media. *Int. J. Solids Structures* 19(8):663–675.

Carter, J.P. and J.R. Booker. 1984. Elastic consolidation around a lined circular tunnel. *Int. J. Solids Structures* 20(6):589–608.

Chahine, N.O., Wang, C. C-B., Hung, C.T., and G.A. Ateshian. 2004. Anisotropic strain-dependent material properties of bovine articular cartilage in the transitional range from tension to compression. *Journal of Biomechanics* 37(8):1251–1261.

Chen, G. and R.T. Ewy. 2005. Thermoporoelastic effect on wellbore stability. *SPE Journal* 10(2):121–129.

Cheng, A. H-D. 1997. Material coefficients of anisotropic poroelasticity. *Int. J. Rock Mech. Min. Sci.* 34(2):199–205.

Cheng. A. H.-D. and E. Detournay. 1988. A direct boundary element method for plane strain poroelasticity. *Int. J. Numer. Anal. Methods Geomech.* 12(5):551–572.

Cheng, A. H-D., Sidauruk, P., and Y. Abousleiman. 1994. Approximate inversion of the Laplace transform. *The Mathematica Journal* 4(2):76–82.

Cheng, S. and L.E. Bilston. 2007. Unconfined compression of white matter. *Journal of Biomechanics* 40(1):117–124.

Christensen, R. M. 1982. *Theory of viscoelasticity, an introduction*. 2nd Ed. New York: Academic Press.

Christian, J. T. and J. W. Boehmer. 1970. Plane strain consolidation by finite elements. *J. Soil Mech. Fdn. Div. Am. Soc. Civ. Engrs* 96(4):1435–1457.

Cohen, B., Lai, W.M., and V.C. Mow. 1998. A transversely isotropic biphasic model for unconfined compression of growth plate and chondroepiphysis. *Journal of Biomechanical Engineering* 120(4):491–496.

Comerlati, A., Ferronato, M., Gambolati, G., Putti, M., and P. Teatini. 2005. A coupled model of anthropogenic Venice uplift. In *PoroMechanics III*, Eds: Abousleiman, Y., Cheng, A.H-D., and Ulm, F-J., proceedings of the 2005 Biot Conference, Norman, Oklahoma, May 24–27, 2005.

Coussy, O. 1991. *Mecanique des milieux poreux*. Paris: Editions Technip.

Coussy, O. 1995. *Mechanics of porous continua*. New York: John Wiley & Sons.

Cowin, S.C. 1999. Bone poroelasticity. *Journal of Biomechanics* 32:217–238.

Cowin, S.C. and M.M. Mehrabadi. 2007. Compressible and incompressible constituents in anisotropic poroelasticity: the problem of unconfined compression of a disk. *Journal of the Mechanics and Physics of Solids* 55(1):161–193.

Cryer, C.W. 1963. A comparison of the three-dimensional consolidation theories of Biot and Terzaghi. *Quart. J. Mech. Appl. Math.* 16:401–412.

Cui, L. and Y. Abousleiman. 2001. Time-dependent poromechanical responses of saturated cylinders. *Journal of Engineering Mechanics* 127(4):391–398.

Cui, L., Abousleiman, Y., Cheng, A. H.-D., and V. Kaliakin. 1995. Finite element analyses of anisotropic poroelasticity: a generalized Mandel's problem and an inclined borehole problem. *Int. J. Numer. Analy. Methods Geomech.* 20(6):381–401.

Cui, L., Cheng, A. H-D., and Y. Abousleiman. 1997. Poroelastic solution for an inclined borehole. *Journal of Applied Mechanics* 64(1):32–38.

Cui, L., Ekbote, S., Abousleiman, Y., et al. 1998. Borehole stability analyses in fluid saturated formations with impermeable walls. *Int. J. Rock Mech. Min. Sci.* 35(4/5):582–583.

Cui, L., et al. 1999. Time-dependent failure analysis of inclined boreholes in fluid-saturated formations. *Journal of Energy Resources Technology* 121(1):31–39.

Deligianni, D.D., Maris, A., and Y.F. Missirlis. 1994. Stress relaxation behaviour of trabecular bone specimens. *Journal of Biomechanics* 27(12):1469–1476.

Detournay, E. and A. H-D. Cheng. 1988. Poroelastic response of a borehole in a non-hydrostatic stress field. *Int. J. Rock Mech. Min. Sci. & Geomech. Abstr.* 25(3):171–182.

Díaz, M.C., Duffy, J.J., Snape, C.E., and K.M. Steel. 2007. Use of high-temperature, high-torque rheometry to study the viscoelastic properties of coal during carbonization. *J. Rheol.* 51(5):895–913.

Dickey, J. W., Ladd, C. C. and J. J. Rixner. 1968. A plane strain device for testing clays. *Research in earth physics, Phase report 10, Civil Engineering Research Report R68-3*. Boston: Massachusetts Institute of Technology.

DiSilvestro, M.R. and J-K.F. Suh. 2001. A cross-validation of the biphasic poroviscoelastic model of articular cartilage in unconfined compression, indentation, and confined compression. *Journal of Biomechanics* 34:519–525.

Diwan, P., Pandey, B.P., and D.K. Gupta. 2011. A fresh look at wellbore stability analysis to sustainable development of natural resources: issues and opportunities. *International Journal of Science Technology & Management* 2(1):55–63.

Ehlers, W. and B. Markert. 2001. A linear viscoelastic biphasic model for soft tissues based on the theory of porous media. *Journal of Biomechanical Engineering* 123:418–424.

Eisenberg, S.R. and A.J. Grodzinsky. 1987. The kinetics of chemically induced nonequilibrium swelling of articular cartilage and corneal stroma. *Journal of Biomechanical Engineering* 109:79–89.

Ekbote, S.M. 2002. Anisotropic poromechanics of the wellbore coupled with thermal and chemical gradients. *Dissertation*, University of Oklahoma.

Ekbote, S. and Y. Abousleiman. 2005. Porochemothermoelastic solution for an inclined borehole in a transversely isotropic formation. *Journal of Engineering Mechanics* 131(5):522–533.

Ekbote, S. and Y. Abousleiman. 2006. Porochemoelastic solution for an inclined borehole in a transversely isotropic formation. *Journal of Engineering Mechanics* 132(7):754–763.

Ekbote, S., Abousleiman, Y., Cui, L., and M. Zaman. 2004. Analyses of inclined boreholes in poroelastic media. *International Journal of Geomechanics* 4(3):178–190.

Ekbote, S., Abousleiman, Y., and M.M. Zaman. 2000. Porothermoelastic solution for an inclined borehole in transversely isotropic porous media. *Fourth North American Rock Mech. Symp.*, Seattle, USA, Sep 5–10, 2000.

El Rabaa, A. W. and D. L. Meadows. 1986. Laboratory and field application of the strain relaxation method. SPE paper 15072, presented at the 56th California Regional Meeting, Oakland, CA, April 2–4, 1986.

El Rabaa, A. W. 1989. Determination of the stress field and fracture direction in the Danian chalk. In: Maury, V., Fourmaintraux, D. (Eds.), Rock at Great Depths. Balkema, Rotterdam, pp. 1017–1024.

Ezzat, M. A. and A. S. El-Karamany. 2002. The uniqueness and reciprocity theorems for generalized thermoviscoelasticity for anisotropic media. *Journal of Thermal Stresses* 25(6):507–522.

Flügge, W. 1967. *Viscoelasticity*. Waltham: Blaisdell.

Friedman, M.H. 1971. General theory of tissue swelling with application to the corneal stroma. *Journal of Theoretical Biology* 30:93–109.

Fung, Y.C. 1981. *Biomechanics – Mechanical properties of living tissues*. Springer-Verlag, NY, p. 47.

García, J.J. and D.H. Cortés. 2006. A nonlinear biphasic viscohyperelastic model for articular cartilage. *Journal of Biomechanics* 39:2991–2998.

García, J.J. and D.H. Cortés. 2007. A biphasic viscohyperelastic fibril-reinforced model for articular cartilage: Formulation and comparison with experimental data. *Journal of Biomechanics* 40(8):1737–1744.

Geuze, E.C.W.A. and T. Tjong-Kie. 1954. The mechanical behavior of clays. In Proceedings of the Second International Congress on Rhelogy, Oxford, July 26–31 1953, V.G.W. Harrison (ed), Butterworths Scientific Publications, London 1954.

Gibson, R.E., Knight, K., and P.W. Taylor. 1963. A critical experiment to examine theories of three-dimensional consolidation. In: Problems of settlements and compressibility of soils, proceedings of the European Conference on Soil Mechanics and Foundation Engineering, Vol. 1, pp. 69–76, Wiesbaden.

Grasley, Z.C. 2007. Poroviscoelastic damping of a uniaxially loaded cementitious cylinder. Presented at the 18th Engineering Mechanics Division Conference, Blacksburg, Virginia, June 3–6 2007.

Griggs, D.T. 1939. Creep of rocks. *J. Geol.* 47(3):225–251.

Griggs, D.T. 1940. Experimental flow of rocks under conditions favoring recrystallization. *Bull. Geol. Soc. Am.* 51:1001–1034.

Hashin, Z. and B.W. Rosen. 1964. The elastic moduli of fiber-reinforced materials. *Journal of Applied Mechanics* 31:223–232.

Hayes, W.C. and A.J. Bodine. 1978. Flow-independent viscoelastic properties of articular cartilage matrix. *Journal of Biomechanics* 11:407–419.

Heard, H.C. 1963. Effect of large changes in strain rate in the experimental deformation of Yule marble. *The Journal of Geology* 71(2):162–195.

Hoang, S. and Y. Abousleiman. 2005. Poroviscoelastic anisotropic solution for Mandel's problem. *PoroMechanics III*, Eds: Abousleiman, Y., Cheng, A.H-D., and Ulm, F-J., Taylor & Francis Group, London, 69–75.

Hoang, S. and Abousleiman, Y. 2009a. Poroviscoelastic two-dimensional anisotropic solution with application to articular cartilage testing. *Journal of Engineering Mechanics* 135(5):367–374.

Hoang, S. and Abousleiman, Y. 2009b. Critical poroviscoelastic anisotropic evaluation of anelastic strain recovery test. Paper SPE 124330 presented at the 2009 SPE ATCE, New Orleans, Louisiana, 4–7 October.

Hoang, S.K. and Abousleiman, Y.N. 2010. Poroviscoelasticity of transversely isotropic cylinders under laboratory loading conditions. *Mechanics Research Communications* 37(3):298–306.

Huang, C.Y., Stankiewicz, A., Ateshian, G.A., and V.C. Mow. 2005. Anisotropy, inhomogeneity, and tension-compression nonlinear of human glenohumeral cartilage in finite deformation. *Journal of Biomechanics* 38(4):799–809.

Huang, C.Y., Mow, V.C., and G.A. Ateshian. 2001. The role of flow-independent viscoelasticity in the biphasic tensile and compressive responses of articular cartilage. *Journal of Biomechanical Engineering* 123(5):410–417.

Hsu, T-W. and S-C. Lu. 2006. Behavior of one-dimensional consolidation under time-dependent loading. *Journal of Engineering Mechanics* 132(4):457–462.

Iyo, T., Maki, Y., Sasaki, N., and M. Nakata. 2004. Anisotropic viscoelastic properties of cortical bone. *Journal of Biomechanics* 37(9):1433–1437.

Jaeger, J.C. and N.G.W. Cook. 1979. *Fundamentals of rock mechanics*, 3rd Ed. London: Chapman and Hall.

Jin, H. and J.L. Lewis. 2004. Determination of Poisson's ratio of articular cartilage by indentation using different-sized indenters. *Journal of Biomechanical Engineering* 126(2):138–145.

Jones, C.A. and Z.C. Grasley. 2009. Correlation of hollow and solid cylinder dynamic pressurization tests for measuring permeability. *Cement and Concrete Research* 39:345–352.

Jourine, S., Valkó, P.P., and A.K. Kronenberg. 2004. Modelling poroelastic hollow cylinder experiments with realistic boundary conditions. *Int. J. Numer. Anal. Meth. Geomech.* 28:1189–1205, doi: 10.1002/nag.383.

Kameo, Y., Adachi, T., and M. Hojo. 2008. Transient response of fluid pressure in a poroelastic material under uniaxial cyclic loading. *Journal of the Mechanics and Physics of Solids* 56(5):1794-1805.

Kanj, M., Y. Abousleiman, and R. Ghanem. 2003. Poromechanics of anisotropic hollow cylinders. *J. Eng. Mech.* 129:1277–1287.

Kanj, M. and Y. Abousleiman. 2005. Porothermoelastic analyses of anisotropic hollow cylinders with applications. *Int. J. Numer. Anal. Meth. Geomech*. 29:103–126.

Kenyon, D.E. 1979. Consolidation in transversely isotropic solids. *J. Appl. Mech.* 46(1):65–70.

Khalil, F. and G. Abdel-Messeih. 1954. Water content of tissues of some desert reptiles and mammals. *Journal of Experimental Zoology* 125 (3):407–414.

Kim, Y.R., Seo, Y., King, M., and M. Momen. 2004. Dynamic modulus testing of asphalt concrete in indirect tension mode. *Transportation Research Record: Journal of the Transportation Research Board* 1891:163–173.

Kirsch, G. 1898. Die theorie der elastizitat und die bedurfnisse der festigkeitslehre. *Zeit Verein Deutsch Ing* 42:797–807.

Le Comte, P. 1965. Creep in rock salt. *J. Geol.* 73:469–484.

Lecampion, B., Constantinescu, A., and L. Malinsky. 2006. Identification of poroelastic constants of "tight" rocks from laboratory tests. *International Journal of Geomechanics* 6 (3):201–208.

Lefeuve-Mesgouez, G. and A. Mesgouez. 2008. Ground vibration due to a high-speed moving harmonic rectangular load on a poroviscoelastic half-space. *International Journal of Solids and Structures* 45:3353–3374.

Leipzig, N.D. and K.A. Athanasiou. 2005. Unconfined creep compression of chondrocytes. *Journal of Biomechanics* 38(1):77–85.

Li, L.P., Buschmann, M.D., and A., Shirazi-Adl. 2000. A fibril reinforced nonhomogeneous poroelastic model for articular cartilage: inhomogeneous response in unconfined compression. *Journal of Biomechanics* 33:1533–1541.

Li, X. 1999. Stress and displacement fields around a deep circular tunnel with partial sealing. *Computers and Geotechnics* 24(2):125–140.

Li, X. 2003. Consolidation around a borehole embedded in media with double porosity under release of geostatic stresses. *Mechanics Research Communications* 30(1):95–100.

Li, X. and R. Flores-Berrones. 2002. Time-dependent behavior of partially sealed circular tunnel. *Computers and Geotechnics* 29(6):433–449.

Mandel, J. 1953. Consolidation des sols (étude mathématique). *Géotechnique* 3(7):287–299.

Mak, A.F. 1986. The apparent viscoelastic behavior of articular cartilage-the contributions from the intrinsic matrix viscoelasticity and interstitial fluid flows. *Journal of Biomechanical Engineering* 108(2):123–130.

Mansour, J. M. and V. C. Mow. 1977. On the natural lubrication of synovial joints: normal and degenerate. *ASME Journal of Lubrication Technology* 99(2):163–173.

McCutchen, C. W. 1962. The frictional properties of animal joints. *Wear* 5(1):1–17.

McTigue, D.F. 1990. Flow to a heated borehole in porous, thermoelastic rock: analysis. *Water Resources Research* 26(8):1763–1774.

Mesgouez, A. and G. Lefeuve-Mesgouez. 2009a. Study of transient poroviscoelastic soil motions by semi-analytical and numerical approaches. *Soil Dynamics and Earthquake Engineering* 29:245–248.

Mesgouez, A. and G. Lefeuve-Mesgouez. 2009b. Transient solution for multilayered poroviscoelastic media obtained by an exact stiffness matrix formulation. *International Journal for Numerical and Analytical Methods in Geomechanics* 33:1911–1931.

Mikami, Y., Kurashige, M., and K. Imai. 2002. Mechanical response of a water-saturated core sample under opposite diametrical loadings. *Acta Mechanica* 158:15–32.

Miller-Young, J.E., Duncan, N.A., and G. Baroud. 2002. Material properties of the human calcaneal fat pad in compression: experiment and theory. *Journal of Biomechanics* 35:1523–1531.

Morland, L.W. 1991. Non-linear viscoelastic response of ice. *Applied Ocean Research* 13(5):254–261.

Mow, V.C., Kuei, S.C., Lai, W.M., and C.G. Armstrong. 1980. Biphasic creep and stress relaxation of articular cartilage in compression: theory and experiments. *Journal of Biomechanical Engineering* 102(1):73–84.

Nakken, S.J., Christensen, T.L., Marsden, R., and R.M. Holt. 1989. Mechanical behavior of clays at high stress levels for wellbore stability applications. In: Maury, V., Fourmaintraux, D. (Eds.), Rock at Great Depths. Balkema, Rotterdam, pp. 141–148.

Noailly, J., Oosterwyck, H.V., Wilson, W., Quinn, T.M., and K. Ito. 2008. A poroviscoelastic description of fibrin gels. *Journal of Biomechanics* 41(15):3265–3269.

Nguyen, V.X. and Y.N. Abousleiman. 2009. Poromechanics response of inclined wellbore geometry in chemically active fractured porous media. *Journal of Engineering Mechanics* 135(11):1281–1294.

Nguyen, V.X. and Y.N. Abousleiman. 2010. Incorporating electrokinetic effects in the porochemoelastic inclined wellbore formulation and solution. *Annals of the Brazilian Academy of Sciences* 82(1):195–222.

Nguyen, V., Abousleiman, Y., and S. Hoang. 2007. Analyses of wellbore instability in drilling through chemically active fractured rock formations. Paper SPE 105383 presented at the 15th SPE Middle East Oil & Gas Show and Conference, Kingdom of Bahrain, 11–14 March.

Nguyen, V.X., Abousleiman, Y.N., and S.K. Hoang. 2009. Analyses of wellbore instability in drilling through chemically active fractured-rock formations. *SPE Journal* 14(2):283–301.

Nguyen, V.X., et al. 2004. Poromechanics modeling of wellbore stability in naturally fractured formations. Paper SPE 90227 presented at the 2004 SPE ATCE, Houston, 26–29 September.

Nomura, S., Kato, K., Komaki, I., Fujioka, Y., Saito, K., and I. Yamaoka. 1999. Viscoelastic properties of coal in the thermoplastic phase. *Fuel* 78(13):1583–1589.

Nur, A. and J. D. Byerlee. 1971. An exact effective stress law for elastic deformation of rock with fluids. *Journal of Geophysical Research* 76(26):6414–6419.

Oomens, C.W., van Campen, D.H., and H.J. Grootenboer. 1987. A mixture approach to the mechanics of skin. *Journal of Biomechanics* 20(9):877–885.

Owen, L.B., Toronto, T.W., and R.E. Peterson. 1988. Reliability of anelastic strain recovery estimates for stress orientation in the Travis Peak formation, Harrison County, Texas. Paper SPE 18165 presented at the 63rd Annual Technical Conference and Exhibition, Houston, Texas, 2–5 October.

Paraschiv-Munteanu, I. and N.D. Cristescu. 2001. Stress relaxation during creep of rocks around deep boreholes. *International Journal of Engineering Science* 39(7):737–754.

Parsons, J.R. and J. Black. 1977. The viscoelastic shear behavior of normal rabbit articular cartilage. *Journal of Biomechanics* 10:21–29.

Patel, D.J., Janicki, J.S., Vaishnav, R.N., and J.T. Young. 1973. Dynamic anisotropic viscoelastic properties of the aorta in living dogs. *Circulation Research* 32:93–107.

Peña, A., Bolton, M.D., Whitehouse, H., and J. Pickard. 1999. Effects of brain ventricular shape on periventricular biomechanics: A finite element analysis. *Neurosurgery* 45(1):107–118.

Pomeroy, C.D. 1956. Creep in coal at room temperature. *Nature* 178(4527):279–280.

Rajapakse, R.K.N.D. 1993. Stress analysis of borehole in poroelastic medium. *Journal of Engineering Mechanics* 119(6):1205–1227.

Sawaguchi, H. and M. Kurashige. 2005. Constant strain-rate compression test of a fluid-saturated poroelastic sample with positive or negative Poisson's ratio. *Acta Mechanica* 179(3–4):145–156.

Schanz, M. and A. H–D. Cheng. 2001. Dynamic analysis of a one-dimensional poroviscoelastic column. *J. Appl. Mech.* 68:192–198.

Schmitt, D.R., Tait, R.J., and H. Spann. 1993. Solution for pore pressure and stress in a porous hollow cylinder: Application to a laboratory experiment. *Int. J. Rock Mech. Min. Sci. & Geomech. Abstr.* 30(7):1057–1060.

Sheldon, H. 1983. Transmission electron microscopy of cartilage. *Cartilage, Volume 1-Structure, Function, and Biochemistry*, Ed: Hall B.K., Academic Press, NY.

Sherwood, J.D. 1993. Biot poroelasticity of a chemically active shale. *Proceedings of the Royal Society of London, Series A* 445:679–692.

Sherwood, J.D. and L. Bailey. 1994. Swelling of shale around a cylindrical wellbore. *Proceedings of the Royal Society of London, Series A* 444:161–184.

Shiffman, R.L. 1971. A thermoelastic theory of consolidation. *Environmental and Geophysical Heat Transfer*, *ASME*, 78–84.

Shu, X. and B. Huang. 2008. Dynamic modulus prediction of HMA mixtures based on the viscoelastic micromechanical model. *Journal of Materials in Civil Engineering* 20(8):530–538.

Simon, B.R. and M.A. Gaballa. 1988. Finite strain, poroelastic finite element models for large arterial cross sections. In R.L. Spilker and B.R. Simon, eds., Computational Methods in Bioengineering, BED-Vol. 9 (ASME, New York, 1988), 325–334.

Simon, B.R., Wu, J.S.S., Carlton, M.W., Evans, J.H., and L.E. Kararian. 1985. Structural models for human spinal motion segments based on a poroelastic view of the intervertebral disk. *Journal of Biomechanical Engineering* 107:327–335.

Soulhat, J., Buschmann, M.D., and A. Shirazi-Adl. 1999. A fibril-network-reinforced biphasic model of cartilage in unconfined compression. *Journal of Biomechanical Engineering* 121(3):340–347.

Spilker, R.L., Donzelli, P.S., and V.C. Mow. 1992. A transversely isotropic biphasic finite element model of the meniscus. *Journal of Biomechanics* 25 (9):1027–1045.

Suh, J-K. and M.R. DiSilvestro. 1999. Biphasic poroviscoelastic behavior of hydrated biological soft tissue. *Journal of Applied Mechanics* 66:528–535.

Tabaddor, F. and R.W. Little. 1971. Interacting continuous medium composed of an elastic solid and incompressible Newtonian fluid. *Int. J. Solids Struct.* 7(7):825–841.

Taylor, P. A., and E. C. Aifantis. 1982. On the theory of diffusion in linear viscoelastic media. *Acta Mechanica* 44:259–298.

Terzaghi, K. 1923. Die berechnung der durchlässigkeitsziffer des tones aus dem verlauf der hydrodynamischen. *Spannungserscheinungen. Siltz. Adak. Wissen. Wien Math.-naturw. Kl.* 132(2a):125.

Terzaghi, K. 1943. *Theoretical soil mechanics*. New York: John Wiley & Sons.

Teufel, L.W. 1983. Determination of in-situ stress from anelastic strain recovery measurements of oriented core. Paper SPE/DOE 11649 presented at the 1983 SPE/DOE Symposium on Low Permeability, Denver, Colorado, 14–16 March.

Teufel, L.W. 1985. In-situ stress state in the mounds test well as determined by the anelastic strain recovery method. Paper SPE/DOE 13896 presented at the SPE/DOE 1985 Low Permeability Gas Reservoirs, Denver, Colorado, 19–22 May.

Vgenopoulou, I. and D.E. Beskos. 1992. Dynamic behavior of saturated poroviscoelastic media. *Acta Mechanica* 95(1–4):185–195.

Voight, B. 1968. Determination of the virgin state of stress in the vicinity of a borehole from measurements of a partial anelastic strain tensor in drill core. *Felsmechanik und Ingenieurgeologie* 6:201–215.

Walker, P.S., Dowson, D., Longfield, M.D., and V. Wright. 1968. Boosted lubrication in synovial joints by fluid entrapment and enrichment. *Annals of Rheumatic Disease* 27(6):512–520.

Wang, Y. and E. Papamichos. 1994. Conductive heat flow and thermally induced fluid flow around a well bore in a poroelastic medium. *Water Resources Research* 30(17):3375–3384.

Warpinski, N.R. and L.W. Teufel. 1989. A viscoelastic constitutive model for determining in-situ stress magnitudes from anelastic strain recovery of core. *SPE Production Engineering* 4(3):272–280.

Wilson, R. K. and E. C. Aifantis. 1982. On the theory of consolidation with double porosity. *Int. J. Eng. Sci.* 20(9):1009–1035.

Wilson, W., van Donkelaar, C.C., van Rietbergen, B., and R. Huiskes. 2005. A filbril-reinforced poroviscoelastic swelling model for articular cartilage. *Journal of Biomechanics* 38(6):1195–1204.

Wilson, W., van Donkelaar, C.C., van Rietbergen, B., Ito, K., and R. Huiskes. 2004. Stresses in the local collagen network of articular cartilage: A poroviscoelastic fibril-reinforced finite element study. *Journal of Biomechanics* 37:357–366.

Wong, H., Morvan, M., Deleruyelle, F., and C.J. Leo. 2008. Analytical study of mine closure behavior in a poro-visco-elastic medium. *Int. J. Numer. Anal. Meth. Geomech.* 32:1737–1761.

Woo, S. L-Y., Akeson, W.H., and G.F. Jemmott. 1976. Measurements of nonhomogeneous, directional mechanical properties of articular cartilage in tension. *Journal of Biomechanics* 9(12):785–791.

Woo, S. L-Y., Simon, B.R., Kuei, S.C., and W.H. Akeson. 1980. Quasi-linear viscoelastic properties of normal articular cartilage. *Journal of Biomechanical Engineering* 102(2): 85–90.

Zhang, J., et al. 2003. Dual-porosity poroelastic analyses of wellbore stability. *International Journal of Rock Mechanics and Mining Sciences* 40(4):473–483.

Zhifa, Y., Wang, Z. Luqing, Z., Ruiguang, Z., and X. Nianxing. 2001. Back-analysis of viscoelastic displacements in a soft rock road tunnel. *International Journal of Rock Mechanics and Mining Sciences* 38(3):331–341.

Zwanenburg, C. and F.B.J. Barends. 2007. The influence of anisotropic stiffness on the consolidation of peat. *Soils and Foundations* 47(3):507–516.